UNIVERSITEIT VAN PRETORIA
UNIVERSITY OF PRETORIA
YUNIBESITHI YA PRETORIA

A COMPARATIVE STUDY OF REYNOLDS-AVERAGED NAVIER-STOKES AND SEMI-EMPIRICAL THERMAL SOLUTIONS OF A GAS TURBINE NOZZLE GUIDE VANE

by

Marius Botha

Submitted in fulfilment of part of the requirements for the degree

MASTER OF ENGINEERING

in the Faculty of Engineering, Built Environment and Information Technology,

University of Pretoria,

Pretoria

February 2009

A COMPARATIVE STUDY OF REYNOLDS-AVERAGED NAVIER-STOKES AND SEMI-EMPIRICAL THERMAL SOLUTIONS OF A GAS TURBINE NOZZLE GUIDE VANE

Marius Botha

Supervisor:	Dr. D. de Kock
Co-Supervisor	Prof. J.P. Meyer
Department:	Mechanical and Aeronautical Engineering
Degree:	Master of Engineering

ABSTRACT

In a typical modern gas turbine engine, the nozzle guide vanes (NGVs) endure the highest operating temperatures. There exists a great drive in the turbine industry to increase the turbine inlet temperatures leading to higher thermal efficiency. This has led to a drive to increase turbine vane- and blade-cooling. Numerical modelling has to a large degree replaced empirical codes and models as the main research tool regarding simulation of blade-cooling. Outdated empirical solvers have made way for commercial CFD solvers such as FLUENT, a Reynolds-averaged Navier-Stokes (RANS) solver. One such empirical solver, TACT1, has until recently still proved to yield acceptable results. A comparative study has been done using the T56 NGV blade to establish the differences, advantages and disadvantages of these 2 codes. The engine and subsequent NGV blade were analysed using NREC, STAN5, LOSS3D and TACT1. RANS simulations were found to be computationally expensive. TACT1 yielded acceptable results compared with computational cost. For modern-day designers, RANS would be the preferred tool.

Keywords: CFD, RANS, FLUENT, Empirical, NREC, STAN5, LOSS3D, TACT1, NGV, Heat Transfer

ACKNOWLEDGEMENTS

I would like to extend a word of thanks to the following people for their help and support pertaining to this dissertation:

My supervisor, Dr. D. J. de Kock for his insight regarding CFD modelling and the effort and time spent on the outlay and revision of this document.

Thomas Roos at the CSIR whose help, support and patience were an invaluable contribution to the successful outcome of this dissertation; in particular his short words of philosophical wisdom in time of need, "If you don't have insight you have nothing".

Glen Snedden of the CSIR, for his help and cynical yet comical outlook on life in establishing what can and cannot realistically be done.

Last but not least, I would like to thank my wife Evelyn Botha for her unequivocal support and understanding with regard to the time spent and sacrifices made for this dissertation.

TABLE OF CONTENTS

LIST OF TABLES

LIST OF FIGURES

LIST OF ABBREVIATIONS

ACIS   Alan, Charles, Ian's System

ASCI   Asynchronous Serial Communications Interface

CAD   computer-aided design

CBDE   cooled blade demonstrator engine

CFD   computational fluid dynamics

DES   detached eddy simulations

DSTO   Defence Science and Technology Organisation

MTTF   mean time to failure

NASA   National Aeronautics and Space Administration

NGV   nozzle guide vane

NURBS   non-uniform rational B-splines

OEM   original engine manufacturer

Q3D   quasi-three-dimensional

RAM   random access memory

RANS   Reynolds-averaged Navier-Stokes

RPM   revolutions per minute

RSM   reynolds stress model

SAAF   South African Air Force

SST   shear stress transport

TIT   turbine inlet temperature

VKI   Von Karman Institute

1D   one-dimentional

2D   two-dimensional

3D   three-dimensional

NOMENCLATURE

CHAPTER 2

Greek Symbols

α	Standard k-ω model damping factor	
α^*	Low Reynolds number correction k-ω model damping factor	
β	Standard k-ω k-ω model constant	
β^*	Low Reynolds number correction k-ω model constant	
ρ	Density	[kg.m^{-2}]
μ	Viscosity	[kg.m^{-1}.s^{-1}]
σ	Prandtl number	
ε	Turbulent eddy dissipation	
Γ	Effective diffusivity..	[kg.m^{-1}.s^{-1}]
ϕ	Constant	
η	Effectiveness	
τ	Shear stress	[N.m^{-2}]
u', v'	Fluctuating velocity...	[m.s^{-1}]
$\bar{u}, \bar{v}$	Mean velocity...	[m.s^{-1}]
ω	Specific dissipation rate	[s^{-1}]

English Symbols

bf	Generalised x direction body force, momentum equation	
D	Cross-diffusion	
d	Diameter[m]	
G	Generation term..	[kg.m^{-1}.s^{-3}]
g	Local gravitational constant to determine Free-convection body force	[m.s^{-2}]
I*	Static enthalpy of fluid	[m^2.s^{-2}]
k	Turbulence kinetic energy.......................................	[m^2.s^{-2}]
L	Characteristic macroscopic length scale	[m]
l	Diameter of smallest turbulent eddies...................	[m]

m	Constant	
Nu	Nusselt number	
P	Pressure .... [kPa]	
Pr	Prandtl number	
R	Radius... [m]	
Re	Reynolds number	
S	Source term .... $[kg.m^{-1}.s^{-3}]$	
T	Temperature .... [K]	
t	Time[s]	
u,v,w	Cartesian velocity .... $[m.s^{-1}]$	
x,y	Cartesian displacement reference...................................... [m]	
U,V	Cartesian absolute velocity.. $[m.s^{-1}]$	
W	Mass flow rate per unit area .... $[kg.\ s^{-1}.m^{-2}]$	
X	Impingement jet, span-wise, centre-to-centre spacing .... [m]	
$Y+$	Dimensionless wall distance	
Y	Dissipation	
Z	Impingement channel width .... [m]	

Subscripts

0	Reference
1,2	Constants
c	Coolant channel
D	Channel hydraulic diameter
eff	Effective
j	Jet impingement or film-cooling
k	Turbulence kinetic energy
t	Turbulent
ω	Specific dissipation rate
τ	Friction
∞	Infinity

CHAPTER 4

Greek Symbols

η   Efficiency

English Symbols

T   Temperature .... [K]

Subscripts

blade   With reference to turbine nozzle guide vane
coolant inlet With reference to coolant inlet location
cooling   With reference to cooling
gas   With reference to combustor outlet location

APPENDIX C

Greek Symbols

γ   Dimensionless ratio of specific heats
η   Efficiency
ρ   Percentage pressure drop

English Symbols

a   Speed of sound .... [m.s^{-1}]
P   Pressure .... [Pa]
PR   Pressure ratio
T   Temperature .... [K]
V   Velocity .... [m.s^{-1}]
w   Mass flow rate .... [kg.s^{-1}]

Subscripts

0	Reference
1	Engine inlet
2	Compressor inlet
3	Compressor outlet
4	Diffuser outlet
5	Combustor outlet
6	Turbine outlet
Δ	Change In
a	Air flow
Bleed	With reference to air bled off
c	With reference to compressor
Cb	Combustor
Duct	With reference to engine inlet duct
P	Pressure
Plane	With reference to aeroplane
t	Turbine

Appendix D

Greek Symbols

ρ	Percentage pressure drop
τ	Percentage temperature gain
Δ	Change in

English Symbols

a	Speed of sound .... [m.s^{-1}]
C	Specific heat .... [J.kg^{-1}.K^{-1}]
M	Mach number
P	Pressure .... [Pa]

PR	Pressure ratio
R	Gas constant .... $[\text{J.kg}^{-1}.\text{K}^{-1}]$
RPR	Ram pressure ratio
RTR	Ram temperature ratio
S	Entropy
V	Velocity .... $[\text{m.s}^{-1}]$
w	Mass flow rate .... $[\text{kg.s}^{-1}]$

Subscripts

0	Reference
1	Engine inlet
2	Compressor inlet
3	Compressor outlet
4	Diffuser outlet
5	Combustor outlet
6	Turbine outlet
7	Ambient at turbine outlet
Δ	Change in
a	Air flow
am	Ambient
Bleed	With reference to air bled off
c	With reference to compressor
Cb	Combustor
Diff	With reference to diffuser
Duct	With reference to engine inlet duct
f	Fuel flow
P	Pressure
Plane	With reference to air plane
S	Sound
t	Turbine
T	Temperature
V	Volume

CHAPTER 1

INTRODUCTION

SUMMARY OF CONTENTS

BACKGROUND

OBJECTIVES OF STUDY

SCOPE

LAYOUT

1.1   Background

In a typical modern gas turbine engine, the nozzle guide vanes (NGVs) endure the highest operating temperatures. These blades are stationary blades located at the inlet to the turbine and their purpose is to guide the flow of hot gases from the combustor exit to the first row of turbine blades. The operating temperatures of the (NGVs) are significantly higher than the melting point of the material. This is a significant problem, as the failure of these blades causes the failure of the entire turbine. Complex technologies are employed to enhance the oxidation and hot corrosion resistance of these blades. Such technologies include thermal barrier coatings and internal cooling techniques and configurations, which are used to increase the rate of heat transfer between the coolant flow and the hot combustor gases.

It can be shown that the thermal efficiency is a function of the compressor pressure ratio, the ratio between compressor inlet temperature and the combustor exit temperature, component efficiencies as well as the properties of the gas [1]. There is a great drive in the turbine industry to increase the turbine inlet temperature (TIT). This increased temperature leads to higher thermal efficiency since the temperature ratio between compressor exit and compressor inlet is directly coupled with the pressure ratio between compressor exit and compressor inlet, as well as the compressor efficiency.

It is this increase in TIT which has caused designers to push cooling technology to its limits. The cooling of stator and rotor vanes is a complex process and this research field has grown considerably over the past 30 years, with numerous papers being published every year. Cooling methods are numerous, and various combinations and variations are often used. The main types of cooling include jet impingement cooling, general convective cooling (one of the oldest and most basic methods used to cool blades and vanes), turbulated rib-cooling and film-cooling (a fairly recent addition and a field in which a great deal of research and development is taking place) [1] [2].

The development of the T56 turbine dates back to the early 1950s with production commencing in 1954. The cooling configurations and technologies employed in the stator vanes are old and outdated when compared with modern stator-cooling

configurations. However, the T56 engine is still operated in over 70 countries worldwide. With over 18 000 engines produced and more than 200 million flying hours accumulated, the T56 has proved to be a robust engine with anticipated operation to continue well beyond 2020 [3] [4].

1.2 Objectives of the study

A problem currently experienced by the South African Air Force (SAAF) with the operation of the T56 engines on the Hercules C-130 is the maintenance interval scheduling. Maintenance interval scheduling of the nozzle guide vane blades is poor due to the fact that not enough information is known about the extent to which thermal fatigue damage these blades. The lifetime of these blades cannot accurately be predicted, as there is no accurate lifetime model for them. Figure 1.1, 1.2 and 1.3 are photo's taken of used T56 NGV blades. The hairline cracks and material deformation due to excessive thermal gradients can be observed with the naked eye.
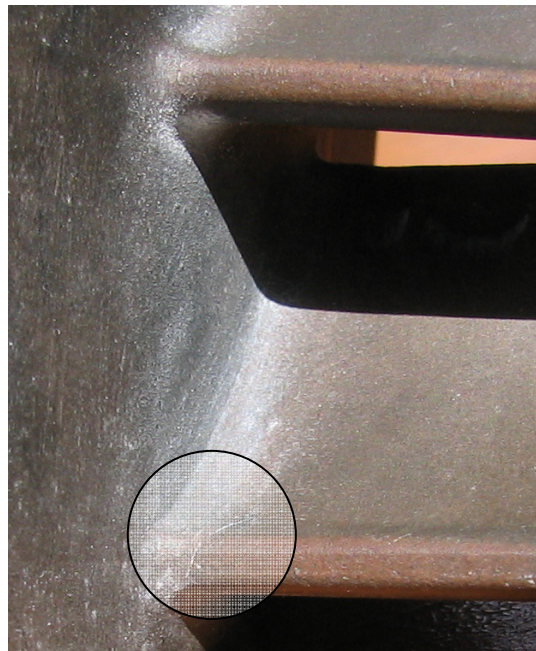
Fig. 1.1 Hairline crack on bottom blade where blade meets casing
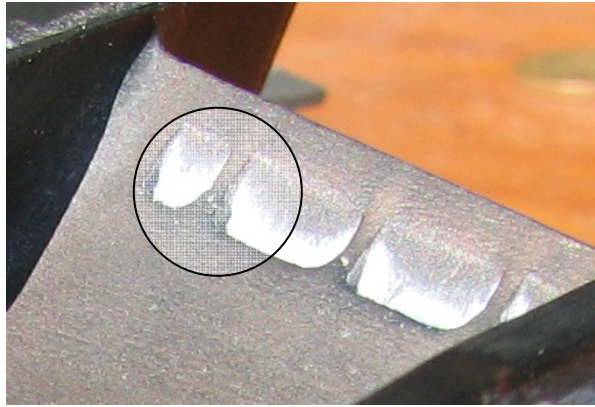
Fig. 1.2 Melted trailing edge at exit ports
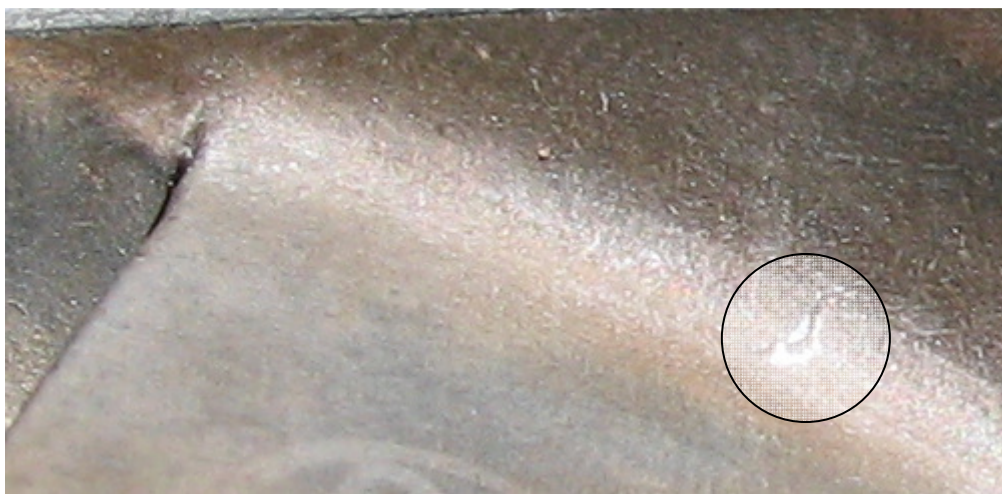
Fig. 1.3 Hairline crack where blade meets casing

It is imperative that this engine is understood, studied and numerically modelled to ensure safe and optimal operation according to its design specifications. Redesign of components and systems such as fuel spray patterns, blade thermal barrier coatings and blade profile optimisation has been an ongoing process since 1954 and still continues today. Although the T56 will not be optimised with respect to blade profiles, maintenance schedules are continually revised with respect to the time between inspections as this is a costly process, which is not always necessary. Mean time to failure (MTTF) calculations are difficult and often empirical data collected over time is the only semi-accurate method to draw up maintenance schedules.

It is the purpose of this research dissertation to focus on Jet impingement cooling and general convective cooling of turbine NGV blades. The cooling configuration considered is that which is found in the T56 series 3 turbine engine [5] [6]. Air was

bled from the compressor and fed to areas of high temperature such as the stator vanes, turbine blades and combustor housing. Particular attention is drawn to the fact that these blades have internal radically spaced chord-wise ribs.

A comparison was drawn between TACT1, a 1D empirical flow solver, and FLUENT, a RANS solver. The magnitude of cross-flow in the radial direction was determined along with vortex patterns and breakaway formed in the T56 NGV. It is important to know what 3D flow patterns are present in the coolant fluid and what effect they have on local heat transfer. Areas of high gradients of heat transfer were identified along with possible problem areas where the material was subjected to high combustor gas temperatures.

1.3   Scope

A comparison between the TACT1 solver and a RANS solver has, to the knowledge of the author, not yet been done. There is no way of knowing the accuracy with respect to other commercially available flow and heat transfer solvers. Such a comparison will yield insight into the accuracy of the TACT1 solver with respect to the omitted radial flow effects. Comparative temperature distributions, heat transfer coefficients and cooling effectiveness will yield much insight into whether it is really necessary to use complex computationally expensive RANS solvers on turbomachinery problems.

The drawback of TACT1 lies in the fact that exit ports cannot be modelled. Instead, the flow has to exit at a trailing edge slot where the pressure and suction surfaces meet. The presence of ribs running along the chord-wise direction as found on the T56 NGV can also not be modelled. Temperature profiles predicted will thus be distorted due to a false or incorrect surface area specified for convection. The drawbacks of RANS solvers on the other hand lie in the computational cost and resources necessary to obtain a solution. The question that lingers is whether TACT1 results are acceptable. To answer this question, there is no need to model reality but to seek an approximate, reasonable answer.

One of the purposes of this work is the investigation of this phenomenon and the effects it has on heat transfer within the blade and temperature distributions. Both the Navier-Stokes solver and empirical correlations for heat transfer and flow approaches have their strengths and weaknesses, which were explored through the modelling of the T56 NGV.

1.4   Layout

This research dissertation contains an in-depth literature survey of the history of the T56 engine. The discussion of NGV cooling leads to the theory behind turbulence modelling and the NREC, STAN5 and TACT1 codes. This serves as a general background to the numerical modelling chapter.

The chapter on numerical modelling does not examine results in detail but contains preliminary work on geometry and boundary condition formulation. A grid-independency study is also done as preliminary work to the result analysis section.

Results were obtained from the RANS solver FLUENT as well as from the empirical solvers of TACT1. The results were compared and preliminary conclusions were drawn. These conclusions are further discussed and recommendations made for further studies pertaining to this field.

CHAPTER 2

LITERATURE SURVEY

SUMMARY OF CONTENTS

INTRODUCTION

T56 ENGINE HISTORY AND LAYOUT

NGV COOLING

TURBULENCE MODELLING

NREC (TDML, TD3D) / STAN5 / TACT1

CONCLUSION

2.1   Introduction

It is common knowledge that in order to optimise the turbine engine and increase efficiencies one has to reach higher combustor temperatures. This is based on fundamental thermodynamic and heat transfer principles, which have been discussed by numerous literature sources [1] [3] [7], publications and almost every thesis or dissertation dealing with turbine engines, [8] [9] [10] to name but a few.

Turbine engines have not only become the main form of propulsion for aircraft but have also embedded themselves into the marine and power generation industry. The advancements that have been made over the past 40 years [11] are astounding and developers are still pushing to produce engines that are more efficient. One of the key driving forces for research and development taking place in the turbine industry today is military institutions. They need turbine-driven aircraft that are lighter in order for them to carry more fuel, armament, equipment and personnel.

The optimising and improving of the turbine engine are driven mostly by the need to increase the turbine inlet temperatures. The higher the turbine inlet temperature, the more efficient the engine becomes. This causes the specific fuel consumption of the engine to decrease [1]. The theory behind this is quite simple. To increase the turbine inlet temperature, one needs to burn more fuel. However, to maintain an acceptable combustor efficiency of at least 99%, the inlet pressure to the combustor also needs to be increased in order for near complete combustion to take place. Any fuel particles not burnt will erode the turbine blades and lead to eventual failure. To facilitate this pressure increase, the pressure ratio of the compressor has to be increased. The limiting factor in most cases seems to be the materials from which compressor and turbine blades are made. One can always burn more fuel and thus increase the turbine inlet temperature, but the limiting factor will always be at the point where the structural integrity of these blades is compromised due to the increased heat load.

The solution to the problem lies in cooling technology, in particular the internal cooling of turbine and stator blades. The engine coolant is obtained by bleeding air from the compressor at delivery point. Bleed values are expressed as a fraction of the entry gas mass flow. Cohen et al [1] state the following values: Annulus walls: 1.6%,

nozzle blades: 2.5%, rotor blades: 1.9%, rotor disk: 0.5%. Air bled from the compressor is used in various cooling configurations and techniques including internal and external cooling. The external blade surface is often cooled via film cooling. This is a process whereby the coolant is injected into the mainstream of hot gases coming from the combustor at discrete locations on the blade.

In older cooling configurations, film-cooling is only used at the trailing edge where the hot gases are ejected into the mainstream from slots. Today, complex showerhead film-cooling configurations are employed where air is ejected out of small holes at discrete locations from the leading edge all the way to the trailing edge. This shields the blade from the hot gases in the immediate vicinity of injection as well as downstream from these holes. A great deal of research is being done on film-cooling of blades and various turbulence models have been experimented with over the past 10 years [12] [13] [14].

Internal cooling often takes the form of jet impingement where coolant is fed through the blade in the radial direction, through a passage referred to as a plenum, from where it is fed through circular, rectangular or oval slots and impinged against the inside of the blade. Earlier blades started off using a single impingement slot across the radial direction of the plenum. Often, the air travels towards the rear of the blade with the aid of ribs from where it exits the blade and joins with the hot gases. The behaviour of coolant gas ejected from the blade into the hot gas path has yielded much research contribution, in particular by Martini et al. [15] [16] [17]. Film-cooling is the active form of cooling in these trailing regions where the coolant flow will exit the blade at the trailing edge and form a protective layer of cooler air over the thinnest part of the blade at the trailing edge.

The purpose of the internal ribs, stretching from the leading to trailing edge, is to increase the heat transfer surface area between the internal coolant air and internal blade surfaces. A secondary purpose of these ribs is to facilitate an increase in turbulence levels as this will yield an increase in heat transfer. These turbulators are, however, more often than not at an angle or normal to the direction of the coolant flow. They are normally located in passages called serpentine passages which guide flow through the blade towards the rear with numerous 180 degree turns in them. The

walls are lined with small ribs inclined at various angles. These rib-roughened walls are mainly to facilitate an increase in turbulence levels and the onset of separation rather than increasing the surface area for convective heat transfer. This literature survey focuses on and discusses in more detail the various cooling techniques and configurations used by the turbine industry for the cooling of NGVs. The mathematics of turbulence modelling is discussed as implemented in commercial CFD codes, as well as their applicability to model the internal cooling of the NGV.

2.2   T56 engine history and layout
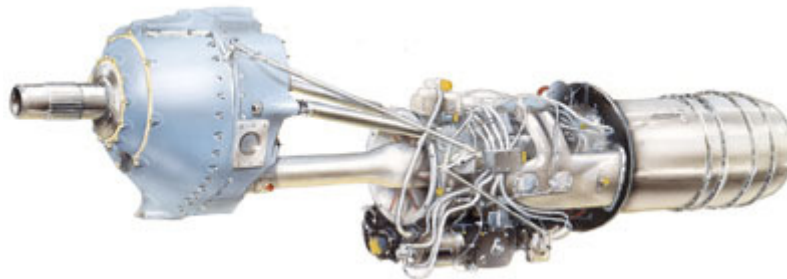
Fig. 2.1 T56-A-15 turboprop engine

The first aircraft to be furnished with the T56-A-15 engine was the C-130H in June 1974. The C-130H engine was a major improvement on the C-130A, with four Allison T56-A-11 or T56-A-9 turboprop engines, which dated back to 1956 and the C-130B, introduced in May 1959, using the T56-A-7 turboprop engines [4].

The Allison T56-A-15 engine consists of a 14-stage axial compressor driven by a four-stage turbine unit. The compressor is connected to a diffuser, which slows down the air sufficiently to facilitate proper combustion. The compressor of the T56-A-15 has a pressure ratio of 9.25:1. Later upgrades in the form of the T56-A-427 yielded an even greater pressure ratio of 12:1. The diffuser is coupled to a six-can annular-type combustor. The four-stage turbine consists of four stator/rotor units. The reduction gearbox has two stages of gear reduction [5].

2.3   NGV-cooling

2.3.1   Turbine and NGV blade-cooling technology development and history

The first patent for a combustion turbine was filed in England and granted to John Barber in 1791. Modern versions of this turbine were patented by Franz Stolze and Charles Curtis in the late nineteenth century [11]. However, these designs were not feasible from the perspective that the power needed to drive the compressor was more than the power output gained from the turbine.

To overcome this problem, the turbine inlet temperatures had to be increased, which was not feasible at the time due to melting point limitations of the blade material. The jet engine race was later fuelled by World War II with Germany's Junkers and Great Britain's Rolls-Royce successfully starting production towards the end of the war. Although most turbine developments during the 1950s and 1960s were made in aircraft industry, power generation soon followed suit with General Electric being able to transfer knowledge to the power generation industry [11].

The 1960s marked a paradigm shift with the introduction of cooling technology within turbine blades and vanes. Increasing the blades' material properties in turbine engines became just as important as cooling the blades and these two fields became complementary to each other. During the next four decades, advancements in cooling technology saw a yielded turbine inlet temperature increase of up to 500K [11] as can be seen in Figure 2.2. Figure 2.3 [11] depicts the cooling configuration advancements made over time. Figure 2.3 is an outline of the type of cooling technology developed by Westinghouse's Heavy Duty Power Generation and Industrial Combustion Turbines. Today, advance is still being made due to intensive turbine research at academic institutions as well at large turbine manufacturing companies and military institutions.
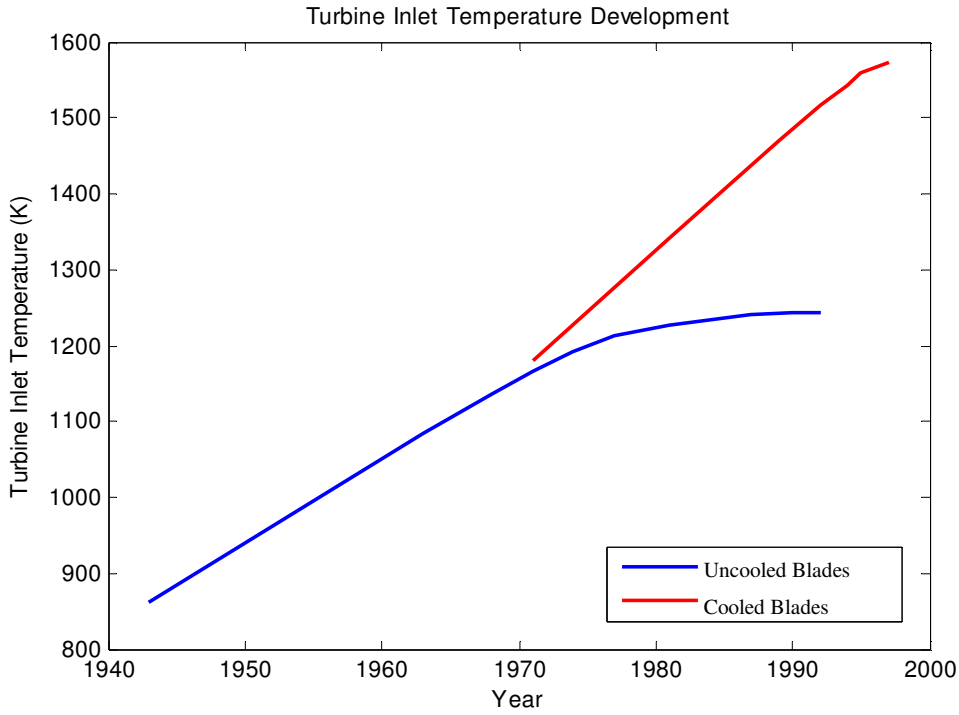
Fig. 2.2 Turbine inlet temperature (Copyright Westinghouse plc [11])
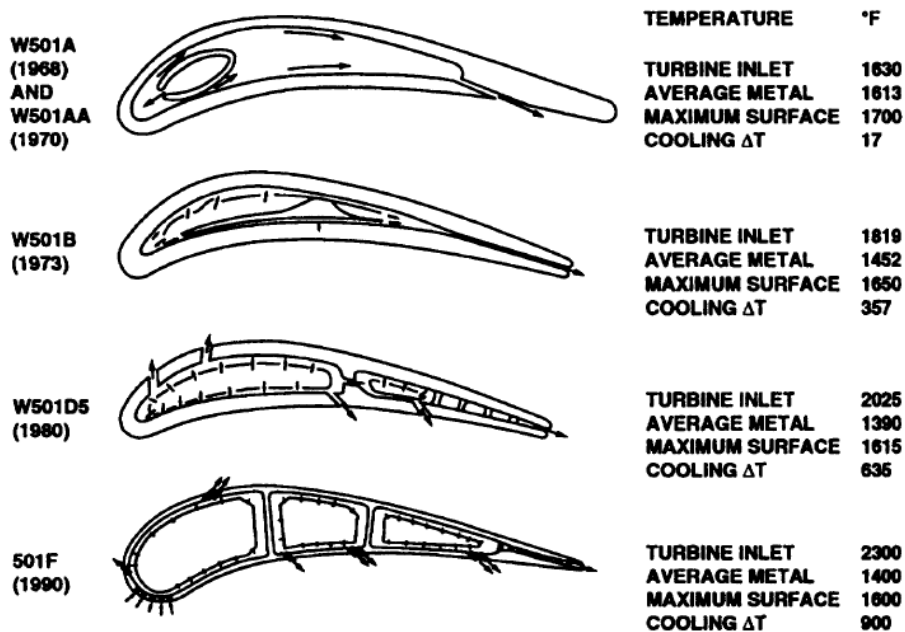
Fig. 2.3 W501 cooling configurations (Copyright Westinghouse plc [11])

Figure 2.4 is a depiction of typical TIT values relating to the coolant configurations, as illustrated in Figure 2.3 [11]. The T56 has a TIT of 1350K and the cooling configuration corresponds to the Westinghouse W501 AA model of 1970 as seen in Figure 2.3.
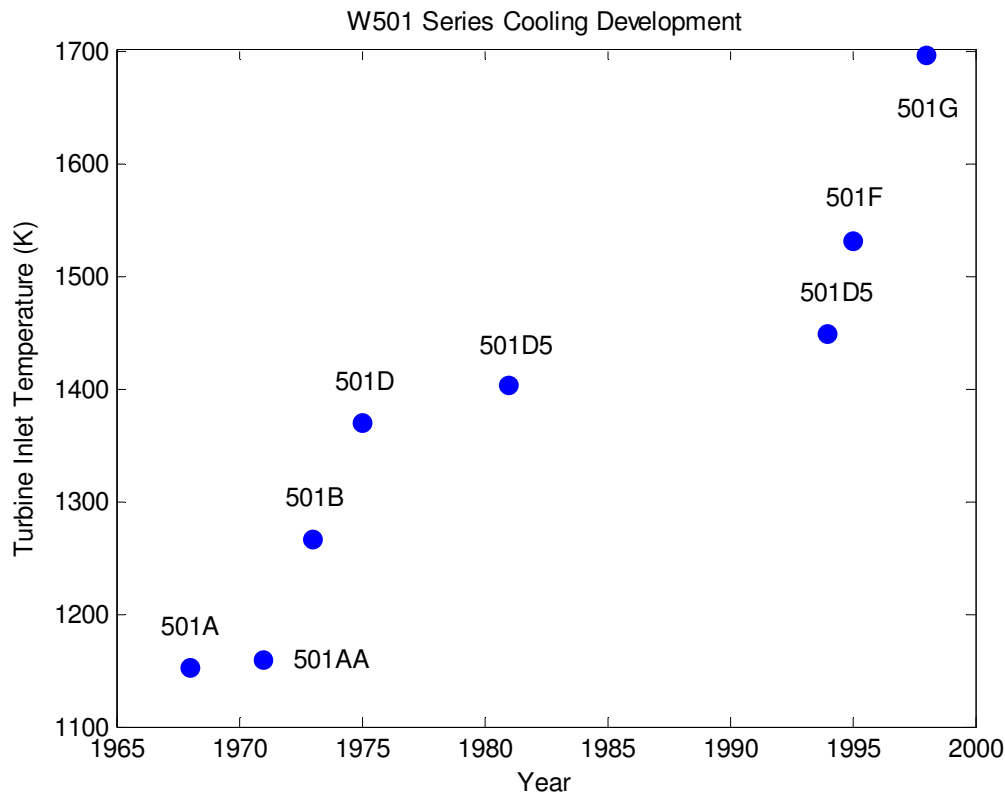
Fig. 2.4 W501 cooling technology timeline (Copyright Westinghouse plc [11])

2.3.2 T56 nozzle guide vane-cooling configuration

The T56 NGV utilises the first type of cooling configuration as illustrated in Figure 2.3. Je-Chin, H., Dutta, S., Srinath, V. E [18] gives in depth explanations for various cooling configurations employed as well as that found in the T56 NGV. Due to the age of the T56 engine, the cooling technology employed in the stator and rotor blades is rather primitive and outdated, dating back to the early 1950s. The stator blade or nozzle guide vane (NGV) has intricate passages within the blade, which guides the coolant air through the blade towards the trailing edge. Air enters the blade through an internal impingement tube called a plenum *(See Figure 2.6)* and travels towards the core of the vane. It then impinges onto the inside of the leading edge through

impingement holes evenly spaced along the radial direction of the blade. There are six impingement slots facing towards the leading edge and one slot facing toward the trailing edge.

Fig. 2.5 T56 NGV 60-blade assembly
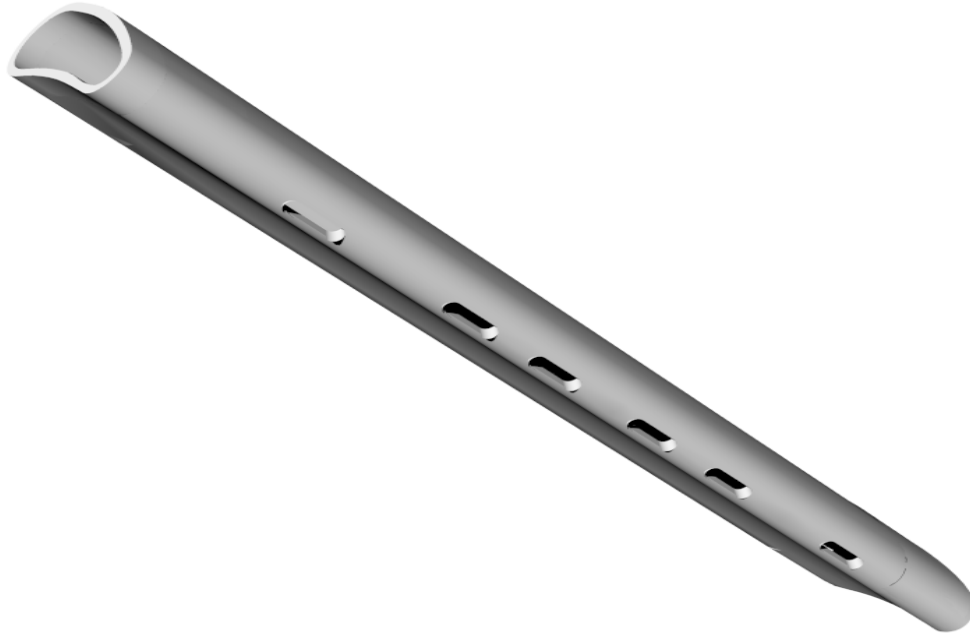
Fig. 2.6 T56 NGV plenum insert

The inside of the blade is divided into four flow passages with three ribs separating these flow regimes from each other. The flow is guided from the leading edge towards the trailing edge with the aid of additional ribs. These ribs are attached to the inside pressure and suction surfaces allowing coolant to still travel in the radial direction across them as shown in Figure 2.7 and Figure 2.8. The purpose of these ribs is to increase the surface area for better heat transfer and to guide the flow towards the trailing edge. These ribs have a constant width throughout the blade but not constant height and are profiled to get thinner towards the trailing edge of the blade. The coolant air exits the vane at the trailing edge through four ports. Each port is located within the four flow regimes described earlier and joins with the combustor gases.
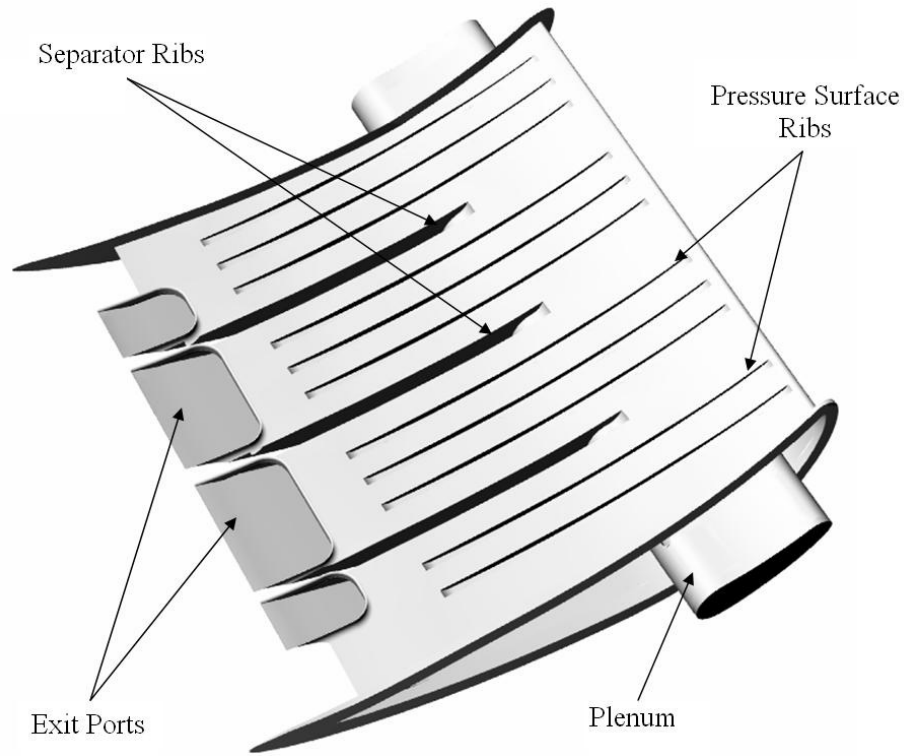
Fig. 2.7 Open section of T56 NGV pressure surface - plenum with ribs and exit ports
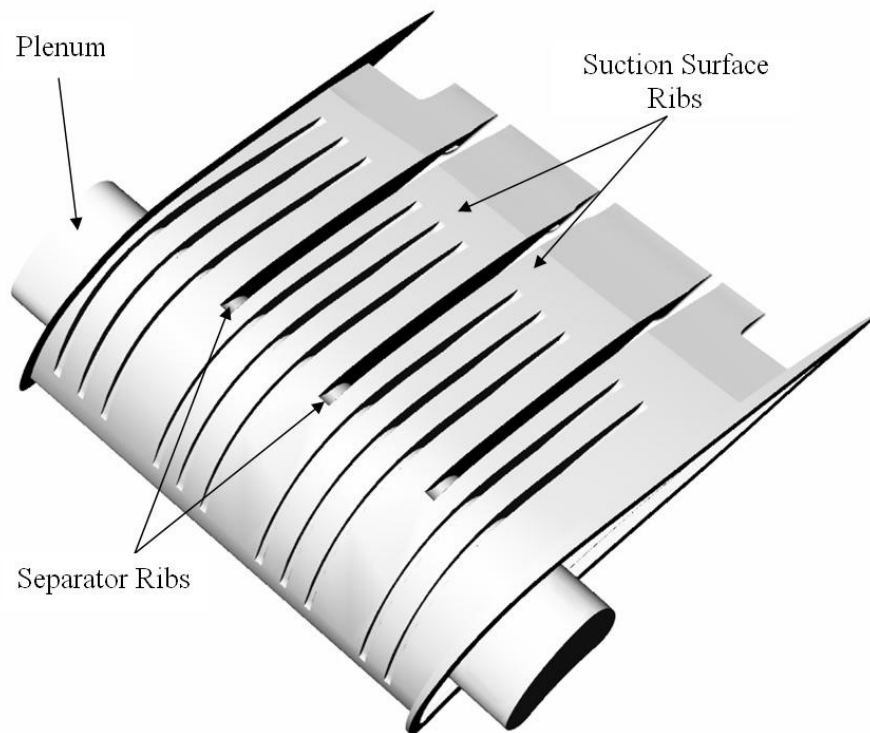
Fig. 2.8 Open section of T56 NGV suction surface - plenum with ribs and exit ports

Figure 2.9 and Figure 2.10 depict the pressure and suction surfaces on the outside of the blade. The hub and casing are also included.
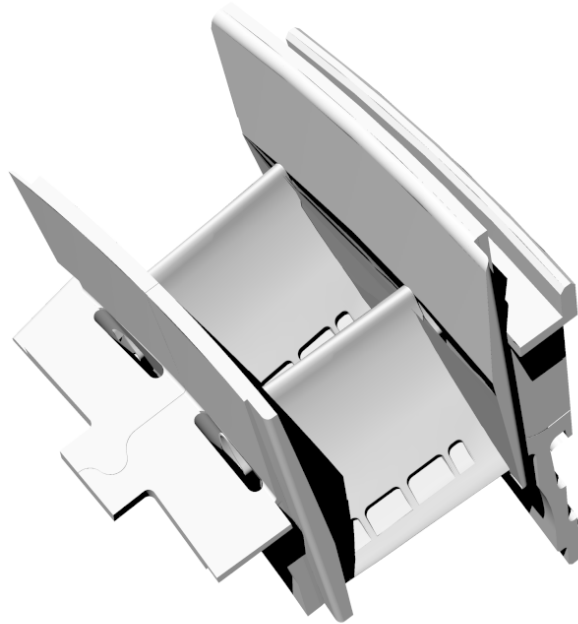
Fig. 2.9 Pressure surface of the T56 NGV

Fig. 2.10 Suction surface of the T56 NGV

2.3.3   Turbine blade/NGV-cooling modelling

In the late 1960s, research into cooling technology really took off [11]. NASA has been involved with cooling technology research ever since, with some of its first publication reports dealing with impingement cooling released in the early 1980s [19] [20] [21]. At the beginning of the 1980s jet impingement cooling had already become the norm for conventionally cooling turbine stator and rotor blades. A great deal of research was thus done during the 1980s to optimise this cooling method through experimental investigation [22] and numerical simulation. Jet impingement is still a favourable cooling method and research is very much still ongoing [23]. However, in recent years impingement cooling has given way to external cooling techniques such as film cooling [18] and work done is very much both experimental and numerical in nature regarding flow as well as heat transfer [24] [25].

Jet impingement cooling had already established a foothold in industrial sectors such as the cooling of electronic equipment, drying of paper and textiles, annealing of metals and glass-tempering operations [20]. This type of jet impingement cooling is still used in industry today. For some applications, a single jet may be sufficient for cooling, but for narrow, long regions such as the inside of turbine blades and vanes a row of slots is used. When considering the modelling of blade cooling a great deal of factors needs to be taken into account. Ejection of coolant gas at the trailing edge of the blade induces pressure losses [26].   All these factors influences the cooling effectiveness.

In the case of the T56 NGV, there is a single row of slots facing towards the leading edge and a single slot is located at the casing-side of the blade facing towards the trailing edge.   The trailing hole is called a dump hole and it is not made for impingement but rather to increase the mass flow of coolant air at the casing.

Florschuetz et al. [20] point out that in the case where coolant air impinging on the leading edge is allowed to flow to the trailing edge where it exits the blade, a cross-flow phenomenon occurs on impingement rows downstream of the leading edge. On the T56 blade, this does not occur, due to the fact that there is only one row of slots facing towards the leading edge and only one slot facing towards the trailing edge.

Due to the fact that these holes are situated on the plenum at an angle of 180 degrees from each other, cross-flow is drastically minimised as the air from the leading edge merely joins the air of the trailing hole with minimal cross-flow influence. The parameterised study conducted by Florschuetz et al. [20] varied the number, spacing and size of the jet orifices. However, due to inadequacy of the correlations used at the time, experimental results obtained from a real turbine varied greatly from the correlated ones.

A second type of cross-flow phenomenon is found in some nozzle guide vanes. Cross-flow can also occur in the radial direction where various jets of turbulent air interfere and merge as they travel towards the trailing edge of the blade.

Florschuetz et al. [19] continued with their work on jet array impingement with-cross flow [20] and successfully established a correlation for streamwise-resolved flow and heat transfer distributions. A simple model pertaining to a one-dimensional incompressible momentum-flux case was drawn up that predicted streamwise distributions of jet and channel cross-flow velocities. Due to limitations in computer power, numerical validation had not yet been established and readily used as an accurate and general means to validate empirical correlations drawn up. However, during the 1980s and 1990s numerical prediction became more accurate and also more established as a design tool in the turbine industry [9] [19] [20] [21] [27] [28] [29].

Quasi-three-dimensional (Q3D) computer programs, for the calculation of fully 3D flow in turbo-machinery blade rows, were the main tools for turbo-machinery aerodynamicists for most of the 1960s and 1970s [27]. One of the shortcomings of Q3D methods is the approximation necessary for solving, and the fact that the blade-to-blade flow is confined to stream surfaces which are surfaces of revolution. The final solution is obtained through iteration between Q3D solutions and blade-to-blade stream surfaces and hub-to-shroud stream surfaces [27].

Crawford and Kayes [30] developed a 2D boundary-layer code called STAN5. The updated version, TEXSTRAN, is capable of handling turbulent flows employing a user-defined turbulence model. Streamwise pressure gradients in the form of velocity

distributions are implemented. The modified version of STAN5 [31] is capable of predicting laminar/turbulent transition, free-stream turbulence augmentation, surface curvature models, surface roughness models and leading-edge heat transfer models. Fully 3D methods for computing the flow are robust in such a way that little human intervention is required due the fact that no iteration between methods is required.

In 1983, Denton [27] developed a time-marching code called LOSS3D. This code became quite popular with many gas and steam turbine manufacturers [27]. This code included various complications such as loss into the basic inviscid calculations as well as boundary-layer blockage and two blade rows in relative rotation. LOSS3D is often used as a pre-processor for STAN5, solving for pressure distributions, which are read into STAN5 from where heat transfer distributions and heat transfer coefficients are obtained.

A computer program was developed by NASA to compute the transient thermal components of a cooled turbine blade or vane equipped with a coolant insert [32]. This code has often been changed and modified to be used as a tool for solving for flow and heat transfer inside a blade for various cooling configurations.

2.4   Turbulence modelling
2.4.1   General overview

The majority of flows naturally found are of a turbulent nature. Turbulence onset is generally measured by the magnitude of the Reynolds number (2.1). As a rough approximation for a Reynolds number above 1 000 the flow is most likely turbulent while for a number below 100, it is probably not turbulent [33].

$$\text{Re} = \frac{\rho \text{LU}}{\mu} \qquad \text{...(2.1)}$$

If L is the characteristic macroscopic length scale and l is the diameter of the smallest turbulent eddies, defined as the scale on which the viscous effects are dominant, then the ratio of these scales can be shown to be of the order of the relation below in Equation 2.2.

$$\frac{L}{l} \approx Re^{\frac{3}{4}} \qquad \dots(2.2)$$

This relation follows from the assumption that in a steady state the smallest eddies must dissipate turbulent energy by converting it to heat. For modest Reynolds numbers of the order of 10 000, the range of L/l spans over three orders of magnitude. The number of control volumes needed for resolving all these eddies would be greater than this ratio, which falls out of the range of current computing power. This limitation is what drives the construction and development of the appropriate turbulence models representing the appropriate turbulent flow.

Today, Reynolds-averaged Navier-Stokes (RANS) solvers are commonly used as a tool to compute the effect of internal blade-cooling. Although turbine manufacturing companies are still using semi-3D in-house-developed codes such as TACT1 and STAN5, it is becoming the norm to use RANS solvers [34] [35] for both research and further development.

Turbomachinery manufacturing companies such as Rolls Royce, Westinghouse and General Electric still make use of in-house-developed codes for solving heat transfer and flow. However, since the 1990s there seems to have been a drive towards using off-the-shelf codes such as FLUENT, CFX or STARR-CD. These codes are more user-friendly but they are computationally more expensive and complex. They offer a great number of user-defined options with respect to different problem setups, operating conditions, turbulence models and post-processing capabilities. These commercial codes vary slightly from one another with respect to the mathematics and discretisation schemes they incorporate [34], but are virtually similar.

Incorporated turbulence models are often based on the modelling of the eddy viscosity (2.3). Eddy viscosity is not a fluid property and varies only with respect to the geometry and the flow conditions. For a simple 2D turbulent boundary-layer flow, the turbulent shear is the only additional unknown term. The gradient diffusion term is made analogous to modular shear following the traditional modelling assumption of J. Boussinesq, 1877 [33].

Turbulent Shear

$$\tau_t = -\rho \overline{u'v'} = \mu_t \frac{\partial \overline{u}}{\partial y} \qquad \ldots(2.3)$$

where $\mu_t =$ eddy viscosity

So-called zero equation models simply use a method to model the eddy viscosity [33]. Later models include the Baldwin-Lomax model (1978) [33], which is an algebraic eddy viscosity model. Modifications to the Baldwin-Lomax turbulence model [12] yielded positive results in the early years of CFD and were successfully incorporated into many CFD codes due to ease of implementation and fast computational time [33].

So-called two-equation models had many benefits over the Baldwin-Lomax model. Turbulent kinetic energy (k) is coupled with turbulent eddy dissipation (ε), turbulence length scale (L) or the vorticity fluctuations (ω) [33]. Later models developed include Reynolds stress models and large eddy simulations. These models are not commonly used when modelling turbine machinery due to their high computational cost. The k-ε model is the industry standard model for predicting turbulent flow due to its robustness, economy, accuracy and its application to a wide range of flow phenomena. However, the standard k-ε model in some cases under predicts the onset of separation and the quantification thereof. This often yields optimistic results with respect to machine performance due to the reduced separation prediction.

The standard k-ε model was improved upon and the realisable k-ε model was developed [36]. The realisable model predicts the physics of turbulent flows more accurately with regard to mathematical constraints imposed on the normal stresses in the fluid. It is also favoured due to its ability to predict non-equilibrium boundary-layer flow more accurately than the standard version. The realisable k-ε model is preferred when it comes to modelling jet-impinging flows. This being the case, it has been found that the realisable k-ε model over-predicts the heat transfer coefficients at stagnation point and under-predicts them at the wall jet zone [37]. However, the realisable k-ε model correlates far better with experimental data than the standard k-ε model.

The k-ω model has been studied by various academics since its addition to the turbulence models in 1992 by Menter [36]. It has been incorporated into various commercially available flow solvers. A memorandum released by NASA in 1997 [13] established that the k-ω shear stress transport (SST) model was the most accurate model for aerodynamic applications. The types of flow phenomena investigated were that of a mixing layer, a round jet, a plane jet, a plane wake and a compressible mixing layer. It would be fair to make the assumption that the k-ω turbulence model performs best for external flow over blade surfaces.

The one-equation Spalart Almares [36] model is also a favoured turbulence model when calculating flow over an external airfoil, due to its simplicity, yielding lower computational cost. The k-ε model requires complex non-linear damping functions and thus lacks the robustness of the k-ω model, where the low Reynolds number computations receive near-wall treatment [14]. Low Reynolds number grids require a *Y+* value of at least smaller than five; however, a value of smaller than two is more favoured when dealing with heat transfer in conjunction with flow. This cannot always be guaranteed and for this reason the k-ω model was developed to allow for a smooth shift from a low reynolds number form to a wall function formulation [14].

Computation of high Reynolds number wall bounded flow, as in the case of many blade coolant passage flows, is very challenging due to its requirements for thin turbulent boundary layers. This holds in particular when heat transfer is being solved in near wall regions where large gradients of the flow field variables, such as velocity and pressure, occur. The representation of the wall boundary has a large impact on the accuracy of the computation. This also becomes a critical factor when looking at the robustness and accuracy of the solver [38].

A study was conducted at the University of Florence defining the main issues and guidelines for an accurate heat transfer CFD simulation of internal ribbed ducts [39]. A low Reynolds k-ε model, high Reynolds k-ε model, high Reynolds k-ε with the use of wall functions and a k-ω model as proposed by Wilcox were used for numerical modelling. For a refined grid the low Reynolds number k-ε model showed significant deviation from experimental results [39].

Garg [40] studied the flow of coolant through the plenum and hole pipes for three staggered rows of showerhead holes on the VKI rotor, and main flow over the blade. This study used the k-ω model of Menter [36] and results were more favourable than those of a previous study where the plenum itself was not modelled, but inlet boundary conditions prescribed at hole exits. The k-ω model also correlated better with experimental results than the Baldwin-Lomax model, Coakley's q-ω model, Chien's k-ε model and Wilcox's k-ω model.

Ameri et al. [41] conducted a study where a Low Reynolds number version of the k-ω model as prescribed by Wilcox and the two equation k-ω SST model as adapted by Menter were used for the calculation of turbulent heat transfer in a 180-degree turn simulating an internal coolant passage. They concluded that substantial grid refinement using the k-ω model of Wilcox did not change the flow characteristics substantially. A substantial difference was observed between the Wilcox k-ω model and the k-ω SST model. A Reynolds stress model (RSM) was also implemented for comparative purposes and results indicated that this model predicted heat transfer more accurately than the two k-ω models. However, the k-ω SST model did perform better than the Wilcox k-ω model. It was concluded that the k-ω SST model is a good substitute for the RSM when computational resources are limited [41].

The validity of the k-ω model has been questioned and in certain cases the k-ε model is still favoured for solving internal blade flow. The realisable k-ε model was successfully implemented in solving for flow and heat transfer on a cooled trailing edge in a modern turbine blade [15]. This model was favoured due to its performance on shear flows including jets, mixing layers and separated flows. Martini et al. [16] later revealed that RANS turbulence models lead to poor predictions in terms of film-cooling effectiveness on the cut-back surface of blades. They did not, however, establish any relation with respect to the performance of a RANS solver in predicting heat transfer coefficients in that region. It was finally concluded that detached eddy simulations (DES) provide reliable results on the discharge coefficients of the exit cooling slots. Furthermore, the k-ω SST steady solver performed quite well with respect to prediction of the discharge coefficients. It was thus found that time-consuming DES simulations were not mandatory for all cases dealing with coolant flow ejection [16].

From the above literature cases, it seems that there are various turbulence models to choose from and they each seem to have their strengths, weaknesses and specified applications where each performs best. Computational time will always weigh heavily when selecting the turbulence model as well as application. It seems that the k-ω SST model offers a compromise between computational time, robustness and accuracy for this study. The k-ω model will now be discussed in more detail.

2.4.2   k-ω model

The standard k-ω model in FLUENT is based on the Wilcox k-ω model [36]. The Shear Stress Transport (SST) k-ω model developed by Menter blends the k-ω model in the near-wall region with the k-ε model in the far field. To account for the transport of the principle turbulent shear stress, turbulent viscosity is modified.

The k-ω modelling of the near wall is robust and accurate, while the k-ε far-field modelling has free-stream independence. A blending function in the near-wall region is used to combine these models. The blending function has a value of one in the near-wall region, which activates the standard k-ω model, while it has a value of zero away from the wall, which activates the transformed k-ε model [36].

$$\frac{\partial}{\partial t}(\rho k) + \frac{\partial}{\partial x_i}(\rho k u_i) = \frac{\partial}{\partial x_j}\left(\Gamma_k \frac{\partial k}{\partial x_j}\right) + \tilde{G}_k - Y_k + S_k \qquad \dots(2.4)$$

$$\frac{\partial}{\partial t}(\rho \omega) + \frac{\partial}{\partial x_i}(\rho \omega u_i) = \frac{\partial}{\partial x_j}\left(\Gamma_\omega \frac{\partial \omega}{\partial x_j}\right) + G_\omega - Y_\omega + D_\omega + S_\omega \qquad \dots(2.5)$$

The main terms of the above two equations, (2.4) and (2.5), will be briefly described below.

$\Gamma_k \, and \, \Gamma_\omega$ (2.6), (2.7) are the effective diffusivities of k and ω respectively.

$$\Gamma_k = \mu + \frac{\mu_t}{\sigma_k} \quad \dots(2.6)$$

$$\Gamma_\omega = \mu + \frac{\mu_t}{\sigma_\omega} \quad \ldots(2.7)$$

σ_ω and σ_k represent the turbulent Prandtl numbers for the turbulent kinetic energy (k) and the specific dissipation rate (ω). μ_t as found in (2.6), (2.7) is the turbulent viscosity and is computed by incorporating both k and ω (2.8).

$$\mu_t = \alpha^* \frac{\rho k}{\omega} \quad \ldots(2.8)$$

A damping factor is incorporated in the form of α (2.9). It damps the turbulent viscosity, which in turn causes a low Reynolds number correction. In the high Reynolds number form of the k-ω model, $\alpha = \alpha_\infty = 1$.

$$\alpha^* = \alpha_\infty^* \left(\frac{\alpha_0^* + \frac{R_{et}}{R_k}}{1 + \frac{R_{et}}{R_k}} \right) \quad \ldots(2.9)$$

$\tilde{G}_k$ (2.10) Represents the production of turbulence kinetic energy for the k-ω SST turbulence model.

$$\tilde{G}_k = \min\left(G_k, 10\rho\beta^* k\omega\right) \quad \ldots(2.10)$$

G_k (2.11) is defined from the exact equation for the transport of turbulence kinetic energy.

$$G_k = -\rho \overline{u_i' u_j'} \frac{\partial u_j}{\partial x_i} \quad \ldots(2.11)$$

The production of ω as represented by $\tilde{G}_k$ (2.10) and G_ω (2.12) is the same as for the standard k-ω model with α being the same as in (2.9).

$$G_\omega = \frac{\alpha}{v_t} G_k \quad \ldots(2.12)$$

$Y_k \ and \ Y_\omega$ (2.13), (2.14) represent the dissipation of k and ω due to turbulence.

$$Y_k = \rho\beta^* k\omega \quad \ldots(2.13)$$

$$Y_k = \rho\beta\omega^2 \quad \ldots(2.14)$$

D_ω (2.15) represents the cross diffusion term, which leads to the model's blending capability.

$$D_\omega = 2(1 - F_1)\rho\sigma_{\omega,2} \frac{1}{\omega} \frac{\partial k}{\partial x_j} \frac{\partial \omega}{\partial x_j} \quad \ldots(2.15)$$

User-defined source terms are introduced in the form of $S_k \ and \ S_\omega$ [36].

For further detail pertaining to the mathematical development of turbulence models, one can turn to texts such as White [33] where derivations of the Navier-Stokes equations are performed from first principles. What is important to note from the equations above is the introduction of the diffusion term (as in equation 2.15 which characterises the k-ω SST model due its unique blending capabilities).

Two variations of the k-ω SST model are implemented in FLUENT [36], thus for a low Reynolds number and for a high Reynolds number. In the low Reynolds number implementation, both the k and ω equations are resolved all the way down to the wall. It is imperative that the grid is suitable for the low Reynolds number modelling with respect to the *Y+* values. *Y+* can be thought of as a local Reynolds number at the wall region. It is a ratio of the flow velocity U, thickness of the wall adjacent cell *y*, fluid density ρ and fluid viscosity μ (2.16).

$$Y^+ = \frac{yU\rho}{\mu} \qquad \dots(2.16)$$

In this case, near-wall mesh guidelines for the enhanced wall treatment are followed. With the intention of resolving the laminar sub-layer, $Y+$ should be smaller than five given that the viscous sub-layer is well within this region. For heat conduction, however $Y+$ should preferably be of the order of two or lower. This can be seen from Figure 2.11 [36]. Figure 2.11 points out that empirical data collected seems to divide the flow regime into three layers. The innermost layer is called the viscous sub-layer. It is here where flow behaves in a laminar fashion and momentum and heat/mass transfer are dominated by the molecular viscosity of the fluid. The outer layer is called the fully turbulent layer where turbulence dominates the flow. The interim layer draws importance from both turbulence and molecular viscosity.
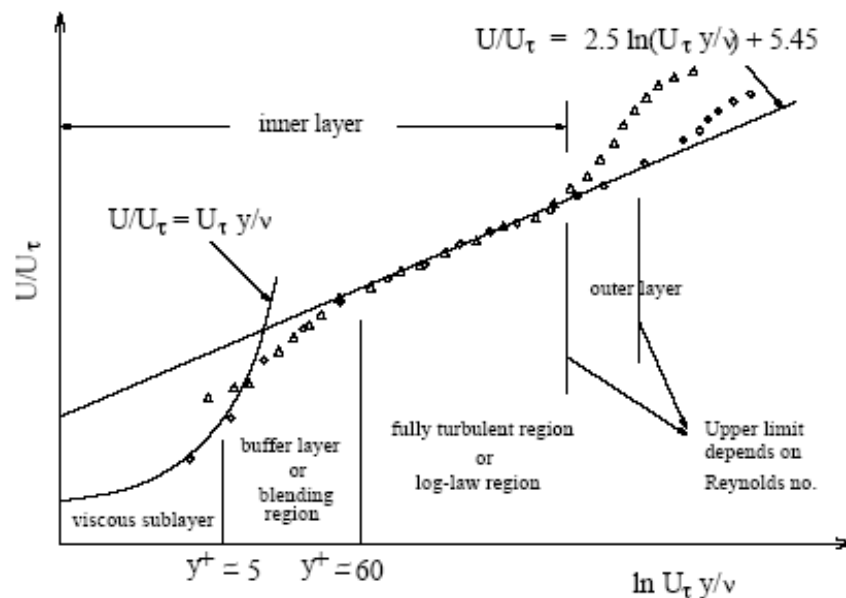
Fig. 2.11 Sub divisions of the near wall region [36]

In the high Reynolds number implementation, the enhanced wall treatment is employed and the near-wall modelling strategy is chosen automatically based on the local $Y+$ values. Therefore, if the grid is fine enough, then the transport equation (2.4) will be resolved all the way to the wall.
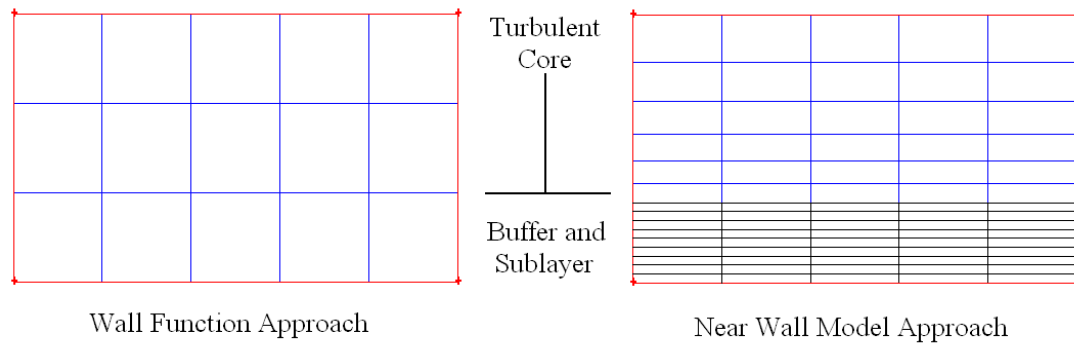
Fig. 2.12 Near-wall treatment in Fluent

The enhanced wall treatment thus acts as a quasi-low Reynolds number approach since only one equation out of the two is resolved to the wall. If the grid is not fine enough, then the blended enhanced wall functions are used, similar to the ones in the k-ε models where the viscosity-affected inner region (viscous sub-layer and buffer layer) is not resolved. Semi-empirical formulas are used to bridge the viscosity-affected region between the wall and fully turbulent region [36]. The computational grids used for these two approaches are depicted in Figure 2.12.

2.5 NREC (TDML, TD3D) / STAN5 / TACT1

Q3D flow calculation methods are robust and flexible to the extent that they can be applied to most turbomachinery applications. Before these methods were developed, axial turbine design consisted mostly of mean line design, which incorporated the solution of the work output equation and mass flow continuity equation for pre-selected values of stage reaction or stage exit swirl and annulus dimensions. These designs were mostly based on experience and empirical results.

Quasi-3D turbine design and analysis methods typically use one-dimensional aerothermodynamics, such as mean line theory and apply them to two-dimensional aerothermodynamics, such as hub-to-casing analysis.

Due to the fact that blade-to-blade flow is confined to stream surfaces, being surfaces of revolution, a component of approximation is added to the solution through correlations such as blade row loss coefficient correlations and performance

correlations. These loss coefficient correlations typically account for the following: level of Reynolds number, which will affect the boundary layer characteristics; amount of blade and disk coolant flows, which merge with the combustor gases; interaction of blade rows, which introduces time-dependant effects on boundary layers downstream as well as upstream of any particular blade row; radial non-uniformity of row inlet flow additions, which has typical effects on secondary flow and the subsequent losses, which go hand in hand.

Errors can creep into the solution and without any way of quantifying these errors the user has no way of telling whether the solution obtained is of sufficient accuracy. Q3D methods use an iterative scheme between Q3D solutions on blade-to-blade and hub-to-shroud stream surfaces [28]. This iterative step often requires the user to interface with the computer program with respect to the selection of relaxation factors and monitoring the effect they have on the convergence of the solution.

Fully 3D methods are thus very attractive in the sense that no iteration is required between methods and user intervention is minimal. Denton [28], although limited to invicid flow only, developed a time-marching code for solving for a fully 3D blade row. The code is capable of handling various geometric complications as well as the inclusion of viscous losses into the inviscid calculation.

NREC is a Q3D computer program that consists of two programs: TDML and TD3D. TDML is used to evaluate alternative mean line turbine designs during a preliminary design analysis [42]. Design requirements are identified and mean line velocity triangle data and stage and blade row performance data are calculated. The more rigorous analysis-governing equations are substituted for the use of loss correlations for ducting and blade rows, correlations for row deviation and expressions for efficiencies based on perfect gas relationships [43]. Total pressure loss coefficients are calculated for the ducting stator and rotor rows. Performance calculations are based on these loss correlations.

The following principle inputs are used. Flow path geometry is defined by hub and casing radius respectively. Stage work output is defined as the power output for each stage as stage exit temperature, gas properties, rotational speed and inlet flow

conditions in the form of the local Mach number and pressure. Stator exit flow angles and tangential velocities control each individual stage. The program calculates complete specifications for Mach numbers, temperatures, flow angles and pressure. Refer to Appendix A and Figure 2.13 for detailed analysis procedures followed.

Mass flow, continuity and total pressure loss equations are solved. The Euler work equation is solved at the rotor exit location. The solution procedure involves two iterative steps. An inner iteration is performed where the absolute velocity is determined at each blade row exit station. This is done by the method of false positioning. All flow conditions are evaluated during this iterative step. The second iterative step involves the outer iteration on the individual stage total efficiencies. Where efficiencies are known no second iteration step is required [42]. Refer to Appendix A for detail on the process for obtaining flow results using TDML and TD3D.

TD3D is the second step in the NREC solution procedure. TD3D analyses the geometry and design point performance of axial turbines. Flow conditions are solved at each design station as well as gas forces on each blade row. The inputs for TD3D are obtained from the results obtained using TDML. Although this solution procedure yields relatively accurate results, there are a few limitations that have to be taken into account. The flow field is treated as 2D, being in the axial and radial directions. Flow is thus considered to be axis-symmetric. Ideal gas relationships are also assumed at each design station.
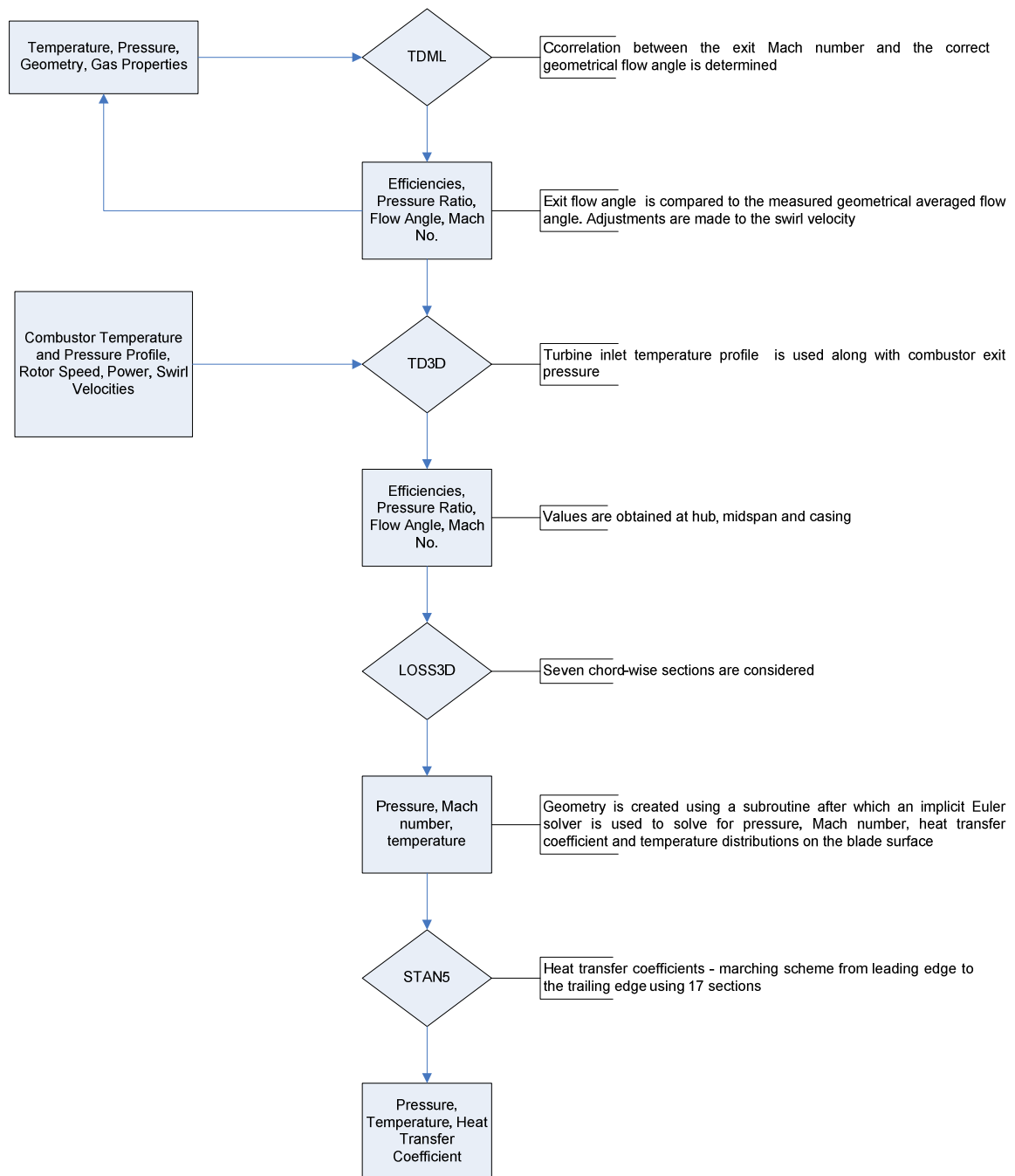
Fig. 2.13 Flow chart of the (TDML, TD3D) / STAN5 / TACT1 solution procedure

The total pressure loss equation, radial equilibrium equation, velocity component equation, the Euler work equation as well as the mass flow continuity equation and the stage power output equation are solved using TD3D. The unknowns are represented in a set of four differential equations derived from the radial equilibrium,

total pressure loss, velocity components and Euler work equations. These are solved at the streamline locations proceeding from the central streamline.

Integrated streamline values of velocity, pressure and temperature are obtained from Runge Kutta integration. The final location of streamline positions is determined in an iterative step since the initial flow distribution is unknown. This iterative step involves an iteration using the values of total pressure loss coefficient and stage power output.

The T56 NGV blades have been modelled by Snedden [31] using a 2D/semi-3D approach where the geometry is created using coordinate points of the blade at discrete slices. Pressure profiles are obtained on the suction- and pressure-side using an implicit Euler marching scheme called LOSS3D. STAN5 is then used to calculate the external temperature profiles and heat transfer coefficients from where TACT1 is used to solve for internal cooling. This method for solving is fast and effective and it is a fair assumption to make that the T56 NGV and turbine blades were most probably designed using this software as they date back to the design and initial optimisation of the T56 engine.

The internal coolant solver, LOSS3D, is an Euler-based solver. One of the drawbacks of this solver is the fact that it solves for 2D slices throughout the blade using a streamwise curvature method. Cross-flow effects in the chord-wise direction can be solved for, however, cross flow within the radial direction of the blade is ignored and deemed negligible. TACT1 uses the results from STAN5 to solve for the internal coolant flow using 1D empirical correlations for fluid flow and 3D heat transfer correlations. Flow is purely 2D but conduction is also solved in the radial direction and thus has a third dimension of computation.

STAN5 is derived from the original program developed by Patankar/Spalding in 1967 [44]. Patankar and Spalding deal with the mathematical equations of the boundary layer as well as a finite difference solution procedure and the capabilities of this procedure. Illustrations of research into physical hypothesis are also dealt with, yielding more insight. These hypothetical situations include some wall flux relationships as well as implications of the mixing length hypothesis.

STAN5 solves for 2D parabolic differential equations only. These equations are the convective boundary-layer transport equations of mass, momentum and stagnation enthalpy. They incorporate the usual boundary-layer approximations and are given in equations 2.17, 2.18 and 2.19. Figures 2.14 and 2.15 illustrate the coordinate system applicable to these equations.

 "I" represents the stagnation enthalpy, while "U" represents velocity. The infinity subscript is designated to represent the flow away from the wall.

Continuity

$$\frac{\partial}{\partial x}(r\rho U) + \frac{\partial}{\partial y}(r\rho V) = 0 \qquad \text{...(2.17)}$$

Momentum

$$\rho U \frac{\partial U}{\partial x} + \rho V \frac{\partial U}{\partial y} = -g_c \frac{dP}{dx} + \frac{1}{r}\frac{\partial}{\partial y}\left[r\mu_{eff}\frac{\partial U}{\partial y} \right] + g_c\left(\frac{\rho g}{g_c} + bf \right) \qquad \text{...(2.18)}$$

Stagnation Enthalpy

$$\rho U \frac{\partial I^*}{\partial x} + \rho V \frac{\partial I^*}{\partial y} = \frac{1}{r}\frac{\partial}{\partial y}\left\{ r\left[\frac{\mu_{eff}}{Pr_{eff}}\frac{\partial I^*}{\partial y} + \frac{\mu_{eff}}{g_c^{\ J}}\left(1 - \frac{1}{Pr_{eff}} \right)\frac{\partial}{\partial y}\left(\frac{U^2}{2} \right) \right] \right\} + S \qquad \text{...(2.19)}$$
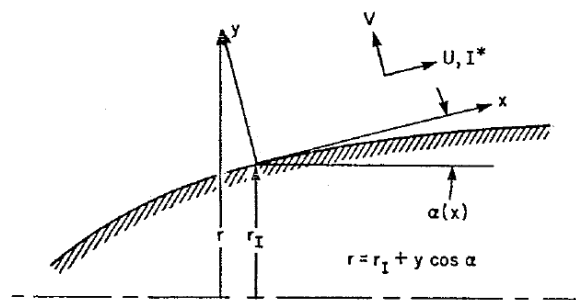
Fig. 2.14 Boundary layer coordinate system pertaining to equations 2.17, 2.18 and 2.19
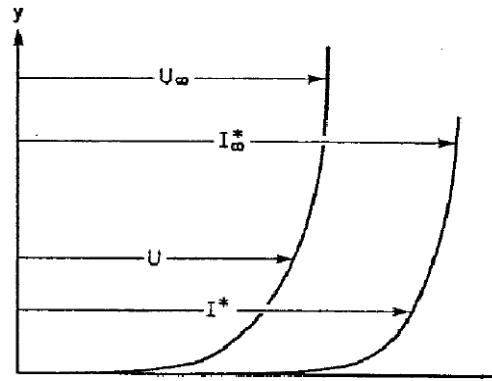
Fig. 2.15 Velocity and stagnation enthalpy profiles pertaining to equations 2.18 and 2.19

The eddy diffusivity concept as discussed in section 2.4.1 is used to model the turbulent stresses in the fluid. Recirculation cannot be dealt with in STAN5. This is a great shortcoming of STAN5, whereas RANS is able to handle recirculation and predict turbulent breakaway and reattachment.

STAN5 solves for laminar and turbulent boundary layers as well as transitions based on a momentum thickness Reynolds number criterion. Wall functions are employed in the near-wall region to allow for a coarse grid. A fully implicit differencing scheme is used for the main variables being velocity, enthalpy and mass concentration. The conservation equations are always satisfied. This together with the implicit scheme allows large forward steps to be taken with no compromise to stability. Fluid properties and turbulence properties are handled explicitly [30].

The strength of STAN5 lies in the fact that no iteration is ever required. This is restricted to relatively small forward steps with a value twice the size of a boundary-layer thickness. Finite difference calculations are made to ease the incorporation of variable boundary conditions and the export of data such as heat flux at frequent intervals along the surface.

TACT1 is a FORTRAN-based computer program used to analyse the transient thermal loads exerted on a cooled turbine blade or vane equipped with a coolant insert [32]. Transient and steady-state temperatures, pressures and flows are solved for in a

vane equipped with a plenum insert using impingement cooling. TACT1 is equipped to solve any of the following modes of heat transfer: impingement cooling including cross-flow, forced convection channel flow and forced convection over pin fins. Refer to Appendix B for illustrations of the control volumes and stations used when solving these flow phenomena or cooling methods. Heat transfer coefficients on the coolant-side are obtained using one of these models.

Limited film cooling capabilities are also taken into account and worked into the code. Coolant flow is assumed to travel in the chord-wise direction and exit the vane through a drilled or split trailing edge and through film-cooling holes. No provision has been made for radial flow of spent impingement air. Film-cooling usage in the program is limited by the numerical model requirement for continuous cross-flow [32].

TACT1 uses inputs of the geometry and coolant properties such as flow rate, temperature and pressure. Spatial Cartesian coordinates are used as inputs for the blade geometry. These coordinates are specified at various increments along a cross-section of the external blade pressure and suction surfaces. The location of these data points is referred to as stations, *(see Figure B3 in Appendix B for a sliced sketch)*. A maximum of 79 stations is allocated around each of the blade sections. The coordinates are recorded for various cross-sectional slices at various radial increments and in such a way that the entire surface is mapped *(see Figure B2 in Appendix B for a sketch showing these slices)*. The program allows for a maximum of 15 slices to be used.

Accuracy does not always increase drastically as the stations increase. However, due to the fact that the code usually takes roughly 500 iterations to converge at roughly one second per iteration, the maximum number of stations is used. In the '80s, however, computational power was minimal and using maximum computational resolution was not always an option.

The blade wall, or thickness, consists of four stations. These are located on internal, midway, external and at the thermal barrier coating regions. The code makes

provision for two different materials to be used in the blade thickness to account for proper modelling of the thermal barrier coating.

Outputs from TACT1 include coolant pressure, flow rates and coolant-side heat transfer coefficients. To obtain these values, a numerical solution has to be obtained for the temperatures throughout the blade at all the stations. At each of these nodal points, a transient energy equation is written forming a set of equations to be solved. The linearised 1D energy balances consist of the following equations: heat conduction at the wall outer surface node, heat conduction at the junction of the cladding and the metal node, and the wall inner surface node. The mid metal node uses a linear, 3D, heat conduction equation. The coolant fluid flow is solved in a very similar fashion. A transient momentum equation for one dimensional flow between adjacent fluid nodes is used to solve for the pressure distributions at every node. This yields the static pressure at these nodes. Energy and momentum equations for one dimensional compressible flow including friction and heat transfer are used to solve for the elemental channel length between two coolant nodes of the coolant flow channel.

Gaugler [32] proposes the following correlations, as first described by Kercher and Tabakoff, are to be used to calculate for heat transfer at impingement and channel flow conditions. Reynolds number conditions stipulate what constants should be used in Equation 2.20.

Impingement – Kercher and Tabakoff

$$\left(Nu\right)_j = \phi_1\phi_2\left(\mathrm{Re}\right)_j^m\left(\mathrm{Pr}\right)^{0.33}\left(\frac{Z}{d_j}\right)^{0.091} \quad \dots(2.20)$$

$$for\ 300 \le \left(\mathrm{Re}\right)_j \le 3000$$

$$m = -0.00145\left(\frac{X}{d_j}\right)^2 + 0.04284\left(\frac{X}{d_j}\right) + 0.51655 \qquad \dots(2.21)$$

$$\phi_1 = \exp\left[0.0126\left(\frac{X}{d_j}\right)^2 - 0.5106\left(\frac{X}{d_j}\right) - 0.2057\right] \qquad \dots(2.22)$$

$$\phi_2 = \frac{1.0}{1.0 + 0.4215\left(\dfrac{W_c}{W_j}\dfrac{Z}{d_j}\right)^{0.58}} \quad \dots(2.23)$$

$$for\ 3000 \le (\text{Re})_j \le 30\,000$$

$$m = -0.00252\left(\frac{X}{d_j}\right)^2 + 0.06849\left(\frac{X}{d_j}\right) + 0.50699 \qquad \dots(2.24)$$

$$\phi_1 = \exp\left[0.0260\left(\frac{X}{d_j}\right)^2 - 0.8259\left(\frac{X}{d_j}\right) - 0.3985\right] \qquad \dots(2.25)$$

$$\phi_2 = \frac{1.0}{1.0 + 0.4696\left(\dfrac{W_c}{W_j}\dfrac{Z}{d_j}\right)^{0.965}} \qquad \dots(2.26)$$

$z = $ Impingement Channel Width

$d_j = $ Channel Hydraulic Diameter (Jet Diameter)

$X = $ Impingemnt Span Center to Center Spacing

$W_c = $ Mass Flow Per Unit Area of Coolant Channel

$W_j = $ Impingement Jet Flow Rate

Turbulent Forced Convection Channel Flow [28]

$$(Nu)_D = 0.023(\text{Re})_d^{0.8}(\text{Pr})^{0.333} \qquad \dots(2.27)$$

2.6   Conclusion

This literature survey not only discussed the background and history behind the T56 turbine engine, but also delved into turbulence modelling using CFD as well as alternative, economical methods to analyse and design turbine vanes and blades using streamwise flow theory.

It is found that the Shear Stress Transport (SST) k-ω turbulence model, developed by Menter, is most suited for internal blade flow and cooling analysis.

Q3D flow calculation methods used for solving external blade flow are discussed and found to be robust and economical as an alternative to CFD analysis.

CHAPTER 3

NUMERICAL MODELLING

SUMMARY OF CONTENTS

3.1   Solution strategy
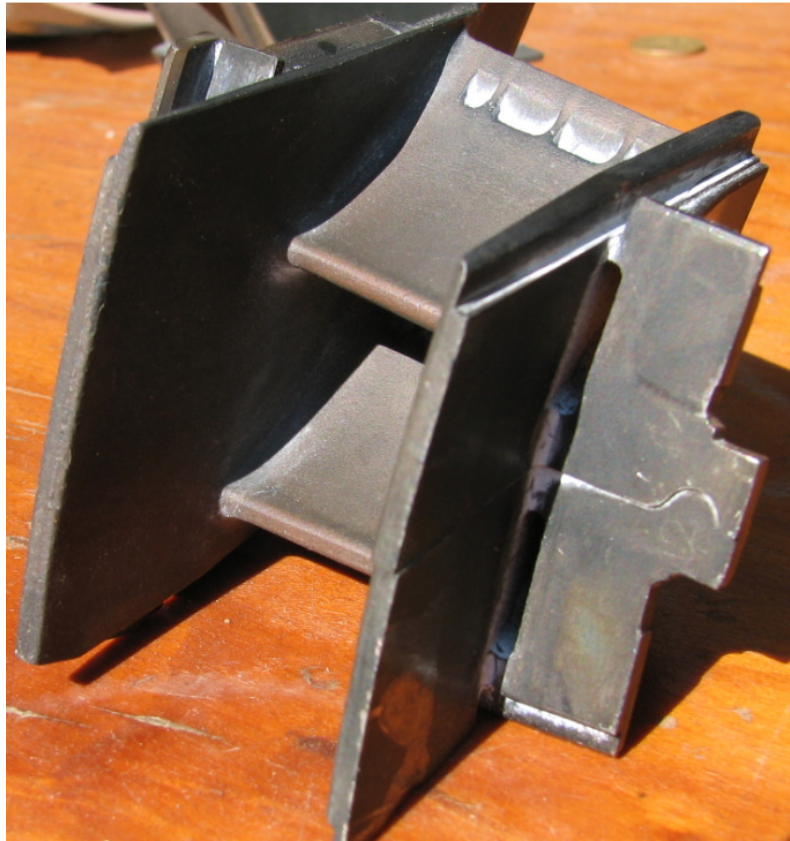
Fig. 3.1 Used T56 NGV

Generating the relevant CAD geometry of the fluid and solid domains of the T56 NGV poses its own problems. Obtaining geometry for CFD codes becomes a reverse engineering process where the T56 NGV was taken apart, disassembled and scanned using 3D laser-scanning technology. These scanned files were very rough, containing many ACIS errors and a great deal of clean up operations have to be done before any meshing can be done. Geometric errors could be due to faulty calibration of the laser scanner yielding different geometries from the real one being scanned.

The solution strategy to the problem as formulated in Chapter 1 entails the acquisition and reverse engineering of the T56 NGV blade geometry. Geometry is cleaned up using the commercial CAD NURBS program Rhinoceros 3.0 from where it is exported to Gambit where meshing operations are done. This process takes a great deal of time due to the fact that a bottom up geometry building approach is followed where vertices, splines and surfaces are constructed up to volume level.

Figure 3.2 shows an outline of the solution procedure that was followed. First, the entire engine was analysed to obtain relevant turbine inlet temperature profiles using published data [5] and basic thermodynamic gas turbine engine theory [1]. Some key information obtained from this analysis includes a profile at turbine inlet temperature, the mass flow of the combustor gas as well as the mass flow and temperature of the internal plenum coolant. These values were used for a LOSS3D analysis where the geometry, mass flow of combustor gas and turbine inlet temperature profile were used to calculate the pressure distribution on the pressure and suction surface of the NGV. A STAN5 analysis was done using the output variables of LOSS3D to obtain heat transfer coefficients and temperature profiles on the pressure and suction surfaces. Data from STAN5 was used for the final step in this process using TACT1 to solve for internal cooling. TACT1 yielded results of internal metal temperatures, heat transfer coefficients and pressures.

All the relevant boundary conditions used for inputs were obtained for the RANS solver FLUENT for further modelling. The computational domain was meshed and the relevant boundary conditions as calculated by STAN5 and the turbine engine analysis were applied. A FLUENT grid-independency study was done to establish the sensitivity of the grid to $Y+$ values, to gain a better understanding of how the flow regime behaves, and to identify areas of interest and importance. A detailed Flow analysis of a quarter section of the entire blade flow domain is done using a low and high Reynolds number approach to determine the effect of using a wall function approach.

The entire NGV blade was resolved using a low Reynolds number approach in the form of the k-ω SST FLUENT solver. This forced the use of a wall function approach. It is known that wall functions only approximate the behaviour of the boundary layer and they are not as accurate as using the low Reynolds number approach. A study was conducted to establish the sensitivity of conduction and convection within the T56 NGV.

A heat transfer study was done on three case studies using the commercial CFD software FLUENT. Firstly, the entire blade was solved for using a wall function approach. The total number of elements used was of the order of 500 000. The T56

NGV was divided into four distinct flow regimes with separator ribs. The second flow regime of these four sections was used as the flow domain for the second case study where wall functions were used to approximate the boundary layer. This model was small with roughly 150 000 elements. This study was done to ascertain the behaviour and effects that the four flow regimes exert on each other. Thermal gradients and flow do exist in the radial direction from hub to casing. A sectional part of the blade will not be exposed to these gradients and effects. This case study thus exposed any such effects that do exist.

The third case study was that of the same sectional model as in case 2, but using a low Reynolds number approach for resolving the boundary layer. Due to $Y+$ restrictions, this model was very fine with an element count of 7.8 million. It would be ideal to model the entire blade using the low Reynolds number approach but that would be computationally too expensive and impractical. Behavioural patterns were identified between these models with respect to conduction and convection in the radial direction of the blade. The results were compared with TACT1 to establish correlation between the RANS solver and empirical solver. However, it was not expected that the correlation will be good between these two solvers. Temperature profiles and cooling effectiveness obtained were compared with those calculated by the TACT1 solver.
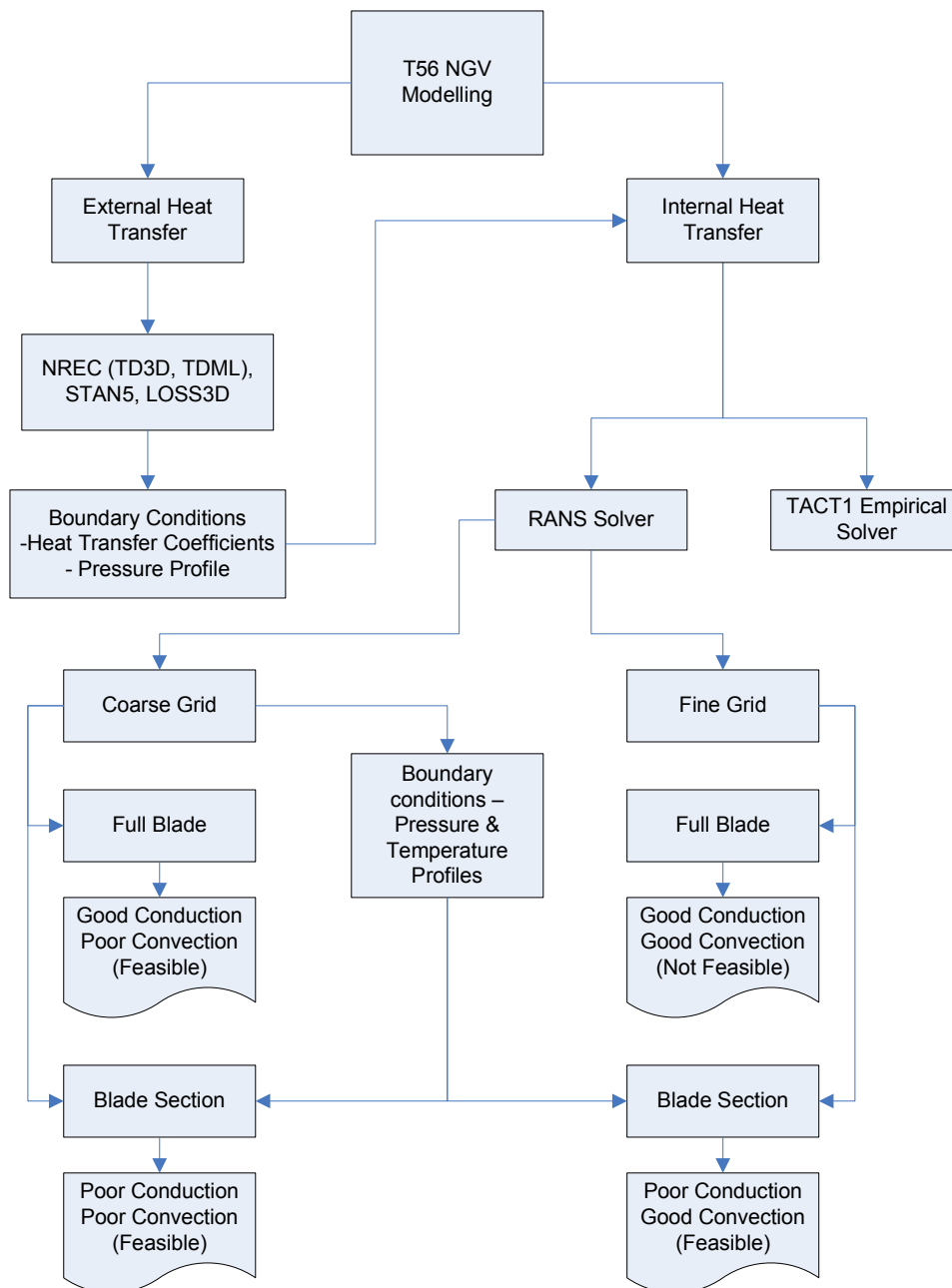
Fig. 3.2 Solution strategy flow diagram

3.2   Geometry acquisition and manipulation

Acquisition of geometry proved difficult due to OEM restrictions. The T56 first-stage NGV is a very complex blade where no symmetry exists. The blade has a different profile at the hub and the casing with an extruded surface with a twist and a draft angle. This makes it difficult to reproduce the geometry in CAD format. The blade thus has to be extruded along a curve with a draft angle and a twist. This implies that

the blade tapers from the casing to the hub and the cross-section at the hub is smaller than at the casing. Creation of this type of geometry through extrusion becomes difficult or impossible as in the case where Gambit is used as the geometry pre-processor and grid-building tool. Gambit has the ability to extrude surfaces into volumes along a curve using either a draft angle or a twist, but not both together. An accurate set of vertex data could be used to interpolate and extrapolate an external flow surface, however, hand-measured vertex data points will have an unacceptable error band which could cause non-smooth surfaces.

The CSIR has facilities where physical objects can be scanned with the use of high accuracy laser technology for the purpose of acquiring a CAD geometry duplication of the object. This is a process of reverse engineering and is the only feasible way of acquiring the geometry of the T56 first-stage NGV. The geometry acquired was of poor quality pertaining to duplicate surfaces, vertices and non-aligned faces. The geometry also had a great deal of problems pertaining to ACIS errors. An illustration of these errors is shown in Figures 3.3 and 3. 4. Most of these errors were embedded in the vertex data and the vertex had to be deleted and created using its Cartesian coordinates.
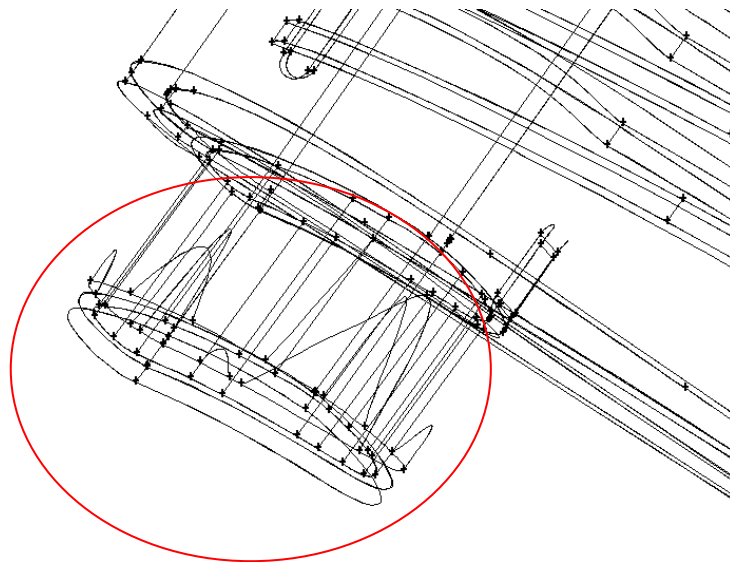
Fig. 3.3 ACIS Geometry curvature errors on the plenum
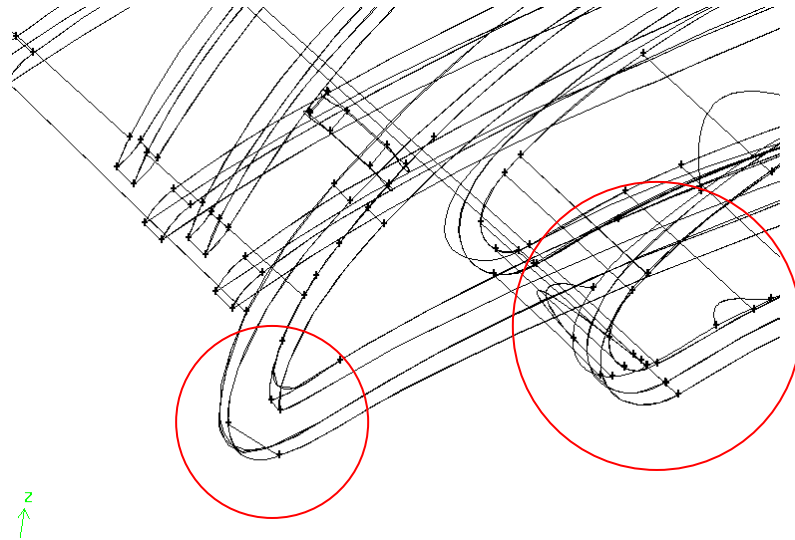
Fig. 3.4 ACIS geometry curvature errors on the plenum and the leading edge of the blade

For the clean-up operations that had to be done on the geometry, the computer suite Rhinoceros v3.0 (Rhino) was used. Rhino is a very user-friendly design suite that has its foundations in NURBS (non-uniform rational B-spline) modelling. NURBS is a mathematical model commonly used in computer graphics for generating and representing curves and surfaces. GAMBIT was used to reconstruct the remainder of the T56 NGV and for meshing.
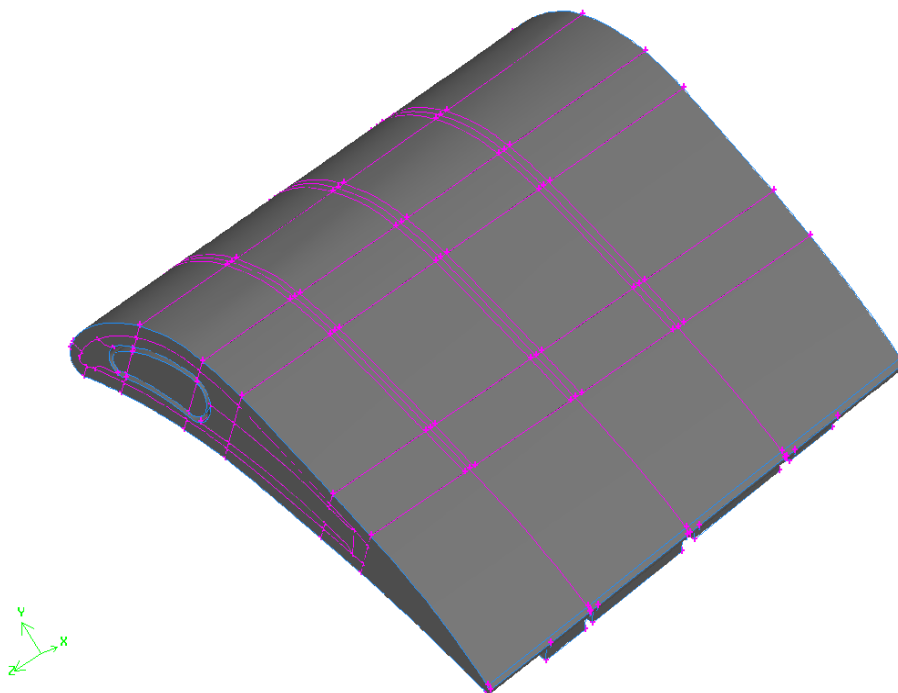
Fig. 3.5 T56 NGV fluid and solid blade geometry – suction surface
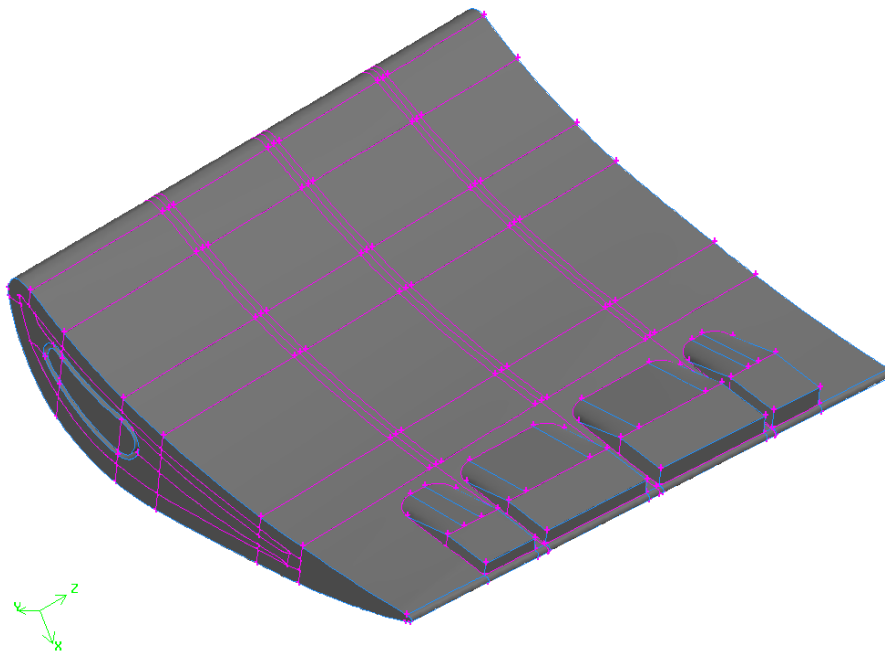
Fig. 3.6 T56 NGV fluid and solid blade geometry – pressure surface

Exit Flow Faces
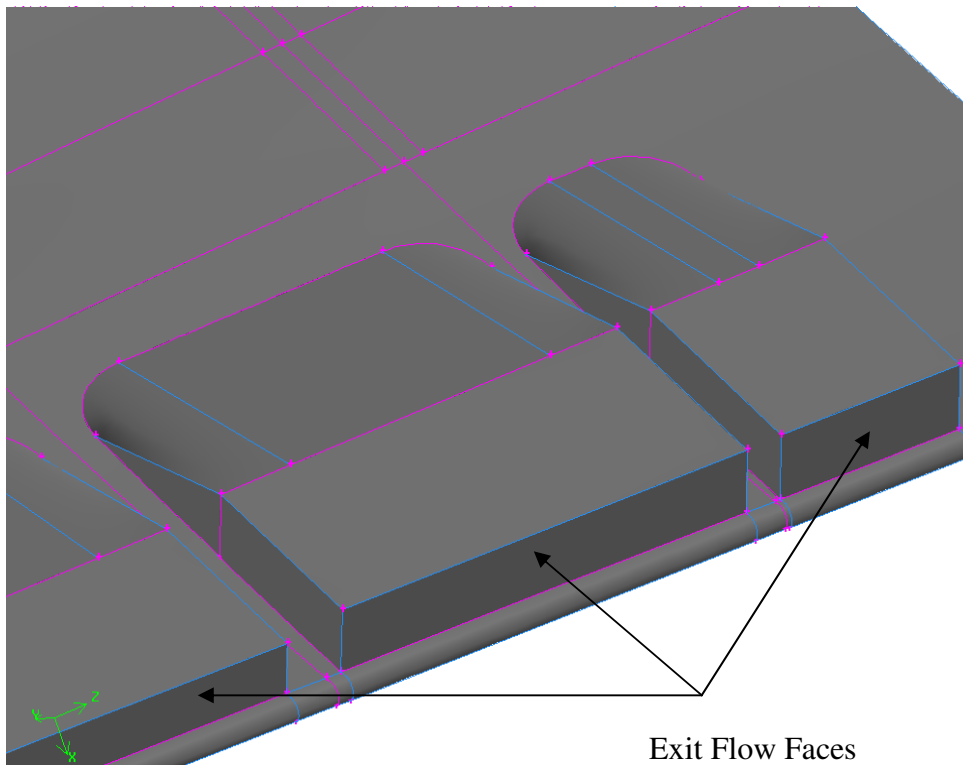
Fig. 3.7 T56 NGV exit port extensions
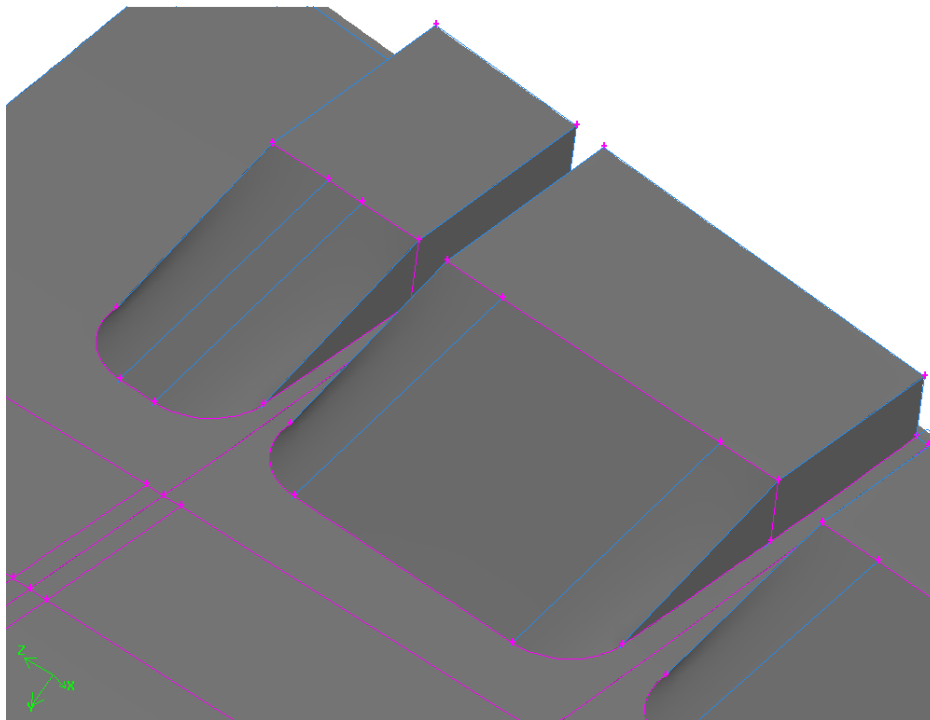
Fig. 3.8 T56 NGV exit port extensions

Figures 3.5 to 3.8 show the healed geometry as it was used for the final CFD analysis. Particular attention is drawn to Figures 3.7 and 3.8 where a close-up of the exit ports is revealed. In order to counteract reverse flow effects at the exit ports, they were extended as is shown. The coolant flow would join the combustor gas flow path and would in actual fact not flow out of these ports as illustrated. The exit ports were adjusted to simulate this behaviour and non-slip boundary conditions were used on the internal surfaces.

3.3   Initial and boundary condition formulation

3.3.1   Engine analysis

Boundary condition formulation is the most important stage in the process of numerical solving using a commercial CFD code. Without proper and accurate boundary conditions such as inlet mass flow rates, temperatures, heat transfer coefficients and pressures, the process of numerical solving becomes flawed. It thus becomes important to spend a considerable amount of time in determining and deriving correct boundary conditions suited to the problem at hand.

Boundary conditions for this study were hard to come by and some assumptions within acceptable limits had to be made at times. Assumptions made were driven from a perspective of insight into the problem rather than guesswork. These assumptions were due to the fact that a great deal of information was obtained from marketing data published in the T56/501D Series III engine training manual [6]. This data was converted from analogue to digital format using a computer program called DGXY [45]. However, as is revealed further in this chapter, this proved inaccurate and was used as a guideline.

3.3.2   Analogue to digital data conversion

The following information was obtained from the T56/501 D Series III Training Manual 15RC12 section 2-26 [6]. Data is tabulated in Table 3.1. The data was digitised and exported to the mathematics program Matlab [46] in order to plot data and obtain accurate values for any axial location in the engine. Figures 3.9 to 3.11 are plots of the total temperature, total pressure and total velocity at various locations in the engine. These locations include the compressor, diffuser, combustor, turbine and exhaust. The horizontal red lines separate these various engine components from each other. These figures give good insight into the engine.

Table 3.1 Data extracted from T56/501 D Series 3 Training Manual [6]

Location	Temp (K)	Pressure (kPa)	Velocity (m/s)
Compressor Inlet	291.79	104.91	176.40
Compressor Exit	602.87	958.50	146.96
Diffuser Exit	604.61	953.28	30.66
Turbine Inlet	1360.40	932.51	178.16
Turbine Exit	858.94	100.71	301.17
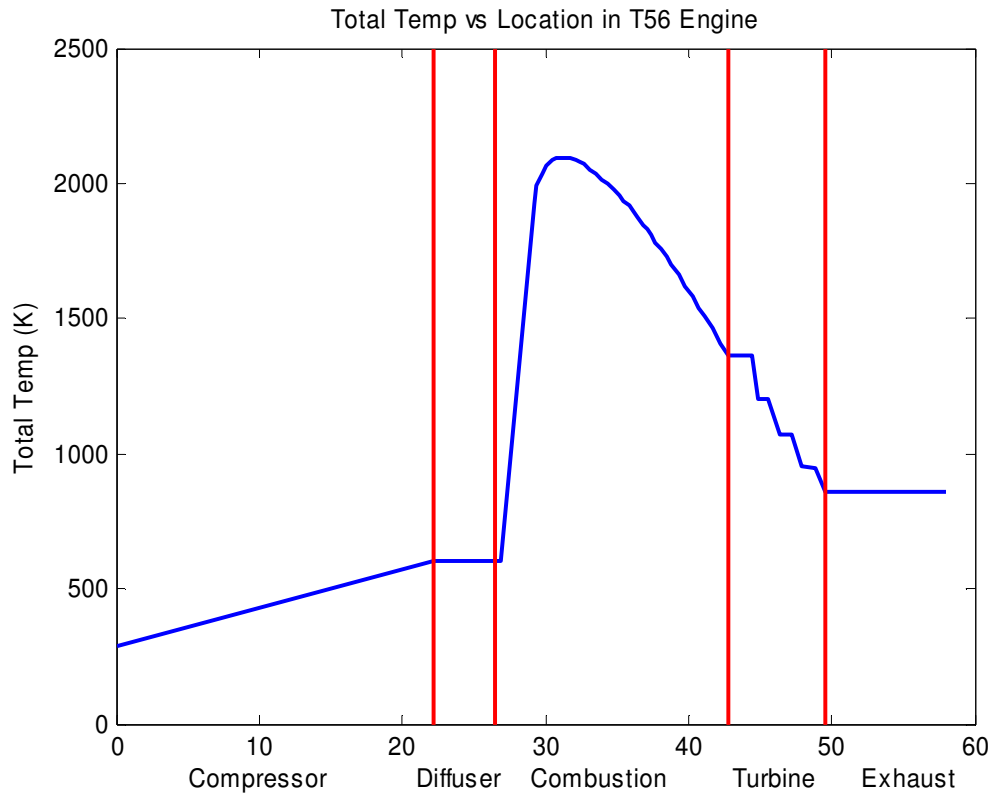
Fig. 3.9 Total temperature vs. location in the T56 engine
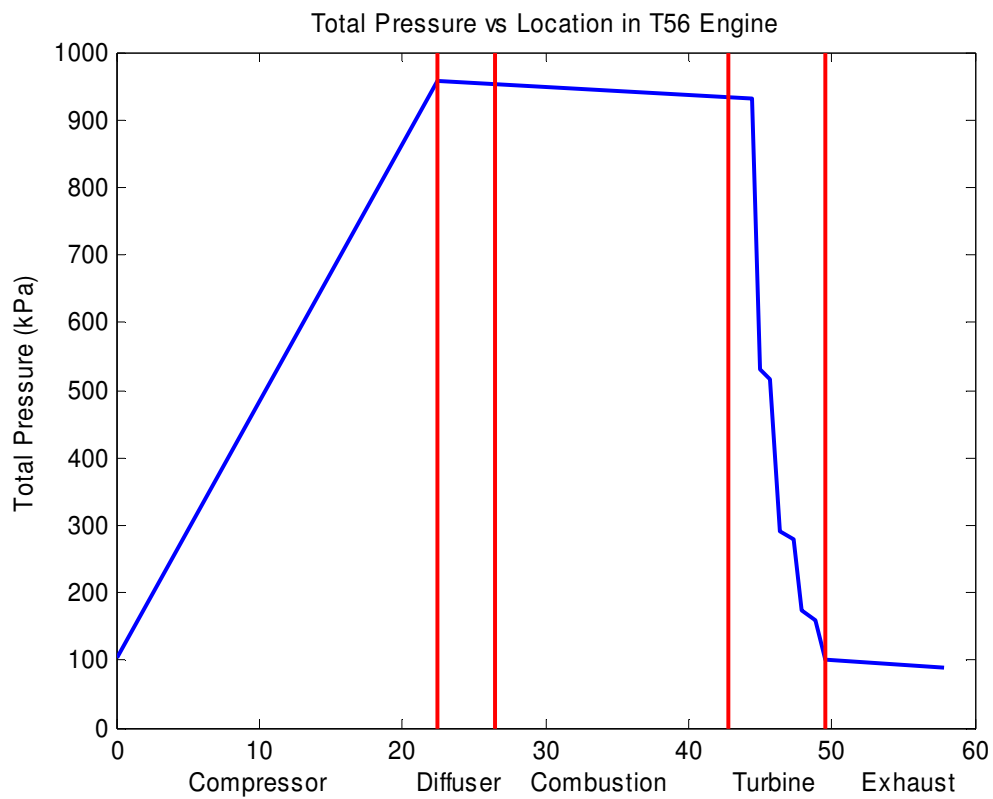
Fig. 3.10 Total pressure vs. location in the T56 engine
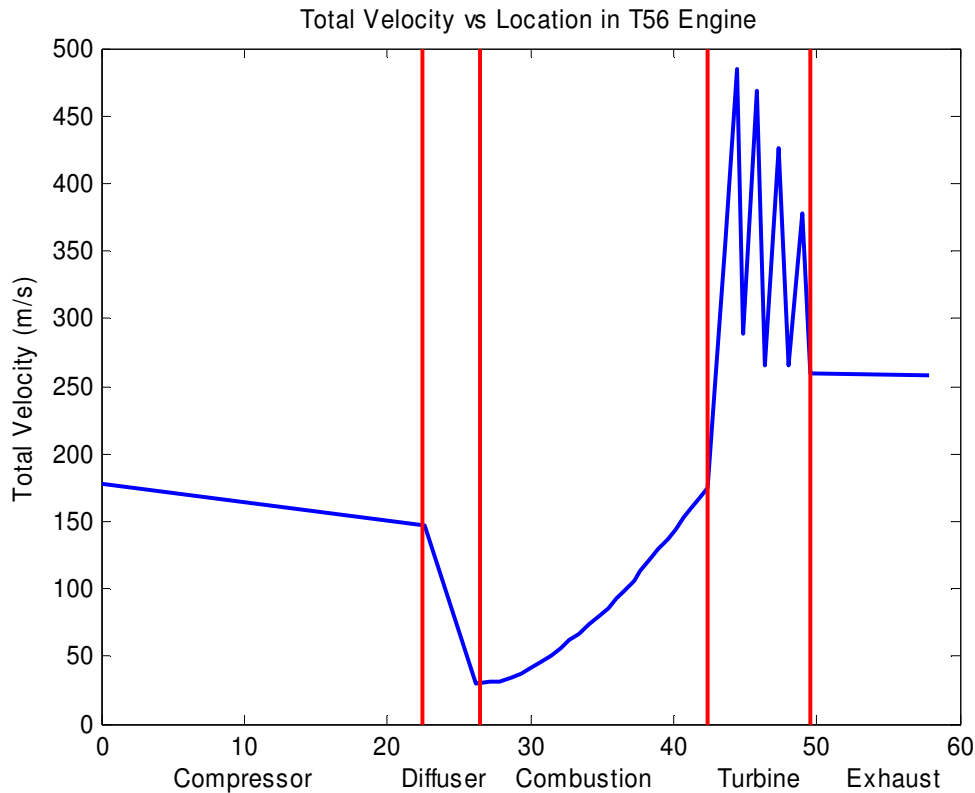
Fig. 3.11 Total velocity vs. location in the T56 engine

3.3.3 Rated Data

The TIT (turbine inlet temperature) is taken as correct due to the fact that it is data published by the OEM (original engine manufacturers). On page 1-1 of the introduction to the T56 series III engine [47] it is revealed that the engine has the following rating:

"4910 E.S.H.P at standard day conditions with an RPM of 100% (13 820 revolutions per minute) and a turbine inlet temperature of 1350 K." [47].

3.3.4 Assumed data

As stated above, it is known that there exists variance in the temperature and pressure profiles represented by the marketing chart [47]. However, this error does not necessarily scale in a linear fashion. It is up to the engineer to investigate the margin of error.

For the above TIT rating, the following environmental boundary conditions were assumed: the temperature of the environment and thus the engine inlet temperature were assumed to be 288 K. The altitude was assumed to be sea level (101.35 kPa).

Further assumptions were drawn from literature [30]. The pressure drop over the combustor was assumed to be 5.1% [43]. This figure is supported by [8] as a theoretical estimate. It was also assumed that the temperature and pressure at the compressor outlet was correct as represented by the marketing diagram [47]. This assumption needed to be made as there was no supplementary documentation listing temperature and pressure as a function of the location in the engine.

3.3.5 Boundary condition formulation for take-off at sea level

2. Compressor Inlet
4. Compressor Outlet
5. Turbine Inlet
6. Turbine Outlet
7. Engine Outlet
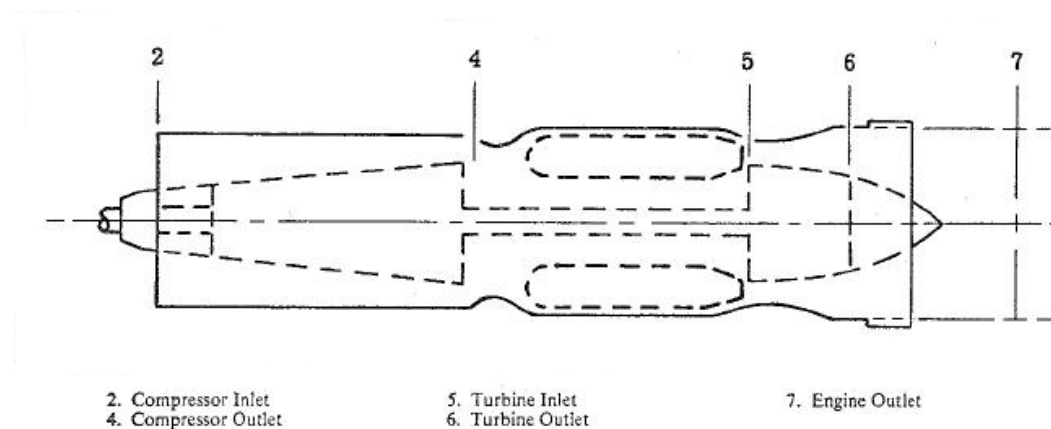
Fig. 3.12 T56 engine layout

P_0 : Ambient pressure = 101325 Pa

P_1 : Engine inlet pressure

P_2 : Compressor inlet pressure

P_3 : Compressor outlet pressure

P_4 : Diffuser outlet pressure

P_5 : Combustor outlet pressure

P_6 : Turbine outlet pressure = 101325 Pa

T_0 : Ambient temperature

T_1 : Engine inlet temperature

T_2 : Compressor inlet tmperature

T_3 : Compressor outlet temperature

T_4 : Diffuser outlet temperature

T_5 : Combustor outlet temperature

T_6 : Turbine outlet temperature

V_{Plane} : Speed of aeroplane

a : Speed of sound

M : Mach number

RPR : Ram pressure ratio

RTR : Ram temperature ratio

PR : Pressure ratio = 9.13

η_{Duct} : Inlet Duct efficiency

η_{Comp} : Compressor efficiency

η_{Diff} : Diffuser pressure drop

ρ_{P-Drop} : Percentage pressure drop across combustor

τ_{T-Gain} : Percentage temperature gain across diffuser

3.3.6   Theoretical Data Evaluation

The data obtained through the T56/501 D Series 3 Training Manual 15RC12 section 2-26 [6] cannot necessarily be taken as accurate and correct. Basic principles were obtained from Cohen, H., Rogers, G.F.C., Saravanamuttoo [1], Sontag et al. [48] as well as Je-Chin, H., Dutta, S., Srinath, V. E [18] were used to verify the accuracy of this data.

See Appendix D for a complete derivation of the T56 Engine Pressure and Temperature for Take-off Conditions. Table 4 shows the data obtained from this derivation.

Table 3.2 Derived T56 engine pressure and temperature for take-off conditions

[Appendix A]

Take-off Conditions	Pressure (kPa)	Temperature (K)
0 Ambient	101.3250	288.00
1 Engine inlet	105.1269	291.04
2 Compressor inlet	104.0757	291.04
4 Compressor outlet	950.2110	601.19
5 Combustor outlet	901.7502	1350.0
6 Turbine outlet	106.3913	873.41

The turbine inlet temperature was used to formulate the temperature profile for the calculated average turbine inlet temperature for take-off. Excel™ and Matlab were

used to formulate a turbine inlet temperature profile corresponding to that for take-off conditions. Experimentally acquired turbine inlet temperatures do exist in the form of DSTO T56 rig data [19]. The integral average of the DSTO T56 rig data profile [49] [50] was computed and compared with the average TIT for take-off conditions. This value is 1350 K and is directly related to the air fuel ratio.
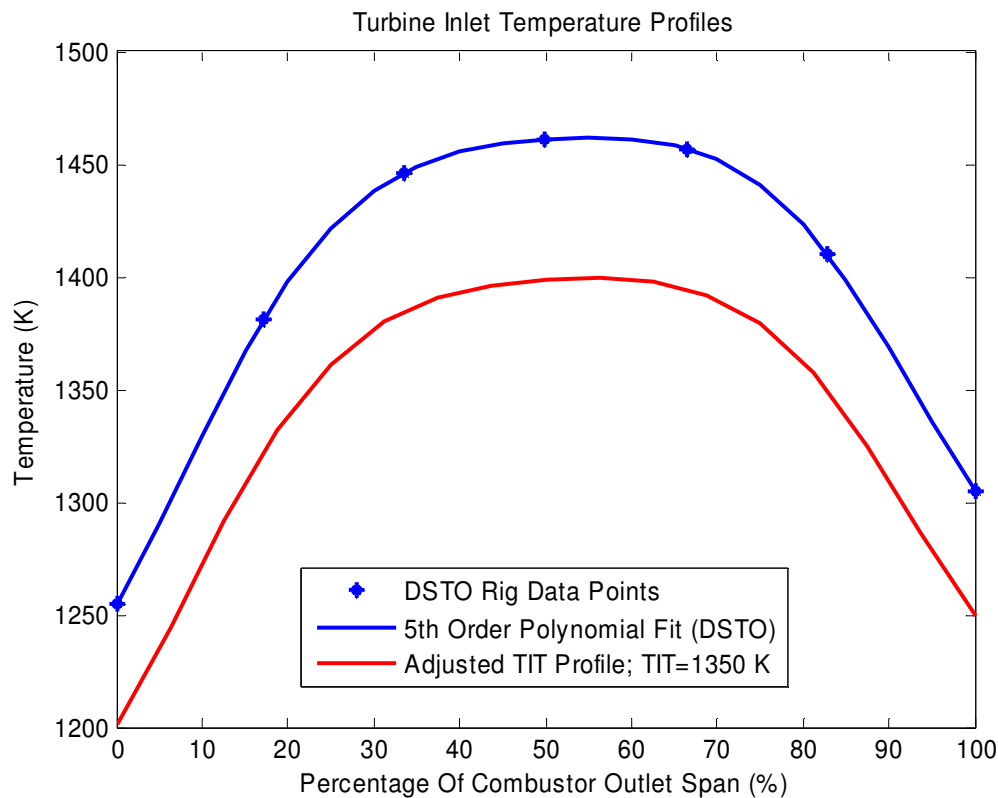
Fig. 3.13 Turbine inlet temperature profile

The TIT profile was adjusted with respect to the DSTO T56 rig data to obtain a new profile that reflects the average of 1350 K, which will be used at take-off conditions *(See Figure 3.13)*. This was based on the assumption that the profile from the DSTO T56 rig data scales according to the integrated average.

The adjusted temperature profile was exported to a text file from where it was used as a boundary condition in NREK (TD3D and TDML) for determining the heat transfer coefficients using STAN5.

3.3.7   LOSS3D, STAN5 and TACT1

The data, acquired from the detail engine analysis above, was used for inputs into the computer programs TDML and TD3D. These include a combustor exit temperature profile as well as the pressure at the inlet to the turbine. These computer packages does not solve for internal coolant flow. The literature survey chapter and Appendix A give more detail on these computer programs. LOSS3D employs a streamline curvature method for solving pressure on the external surface of the NGV. It does this using the boundary conditions derived from the engine analysis as inputs. These inputs include the bulk TIT, pressure, mass flow rate as well as general gas and metal properties. The turbine also requires values for rotational speed and casing tip clearance. LOSS3D takes into account the interaction between the stator and rotor blade and models the entire turbine. From the CAD geometry of the T56 NGV, geometrical measurements were made and the exit flow angle is calculated.

There is a relationship between the exit flow angle and the exit Mach number of any given blade. This relationship was obtained from Cohen et al. [1] and digitised using DGXY [45]. This data, however, can only be used to obtain the correlations shown in Figure 3.14 for flow angles with relevant Mach numbers of 1.0 or 0.5. Matlab was used to plot the data and through interpolation, flow angles for any Mach number between 0.5 and 1.0 were obtained. This relationship is shown in Figure 3.14.
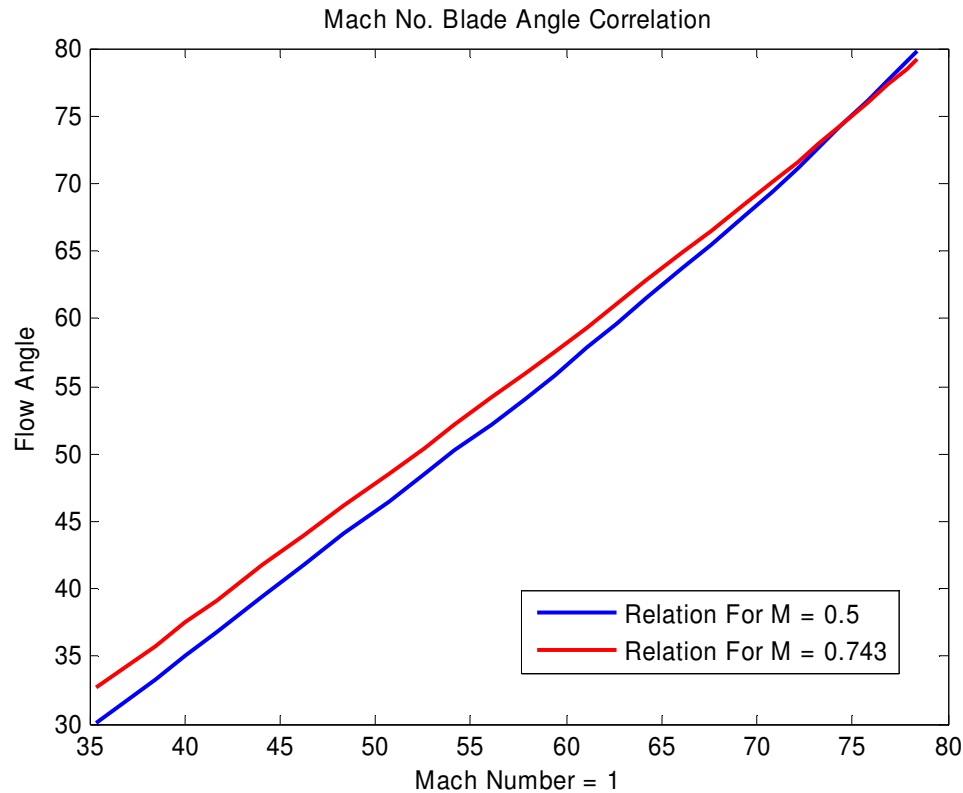
Fig. 3.14 Mach number correlation

After the engine analysis was performed, the blade-to-blade flow was analysed using TDML, a package where the correlation between the exit Mach number and the correct geometrical flow angle can be determined. Due to variations of Cp with respect to fuel/air ratio and temperature, an empirical correlation for kerosene in dry air was used as determined by Walsh and Fletcher [51]. The exit flow angle obtained was compared with the measured geometrical averaged flow angle. Adjustments were made to the swirl velocity and the process was repeated in an iterative fashion until the measured flow angle corresponded to the calculated one. With the correct Mach number known, a further analysis was done using a TIT profile to calculate the pressure profile on the external blade surface.

Geometry for STAN5 was created using a sub-routine after which an implicit Euler solver was used to solve for pressure *(see Figures 3.15 and 3.16)*, Mach number, heat transfer coefficients and temperature distributions on the external blade surface. Heat transfer coefficients were solved for using a marching scheme starting at the leading

edge and working its way to the trailing edge of the blade. These heat transfer coefficients can be seen in Figures 3.17 and 3.18.
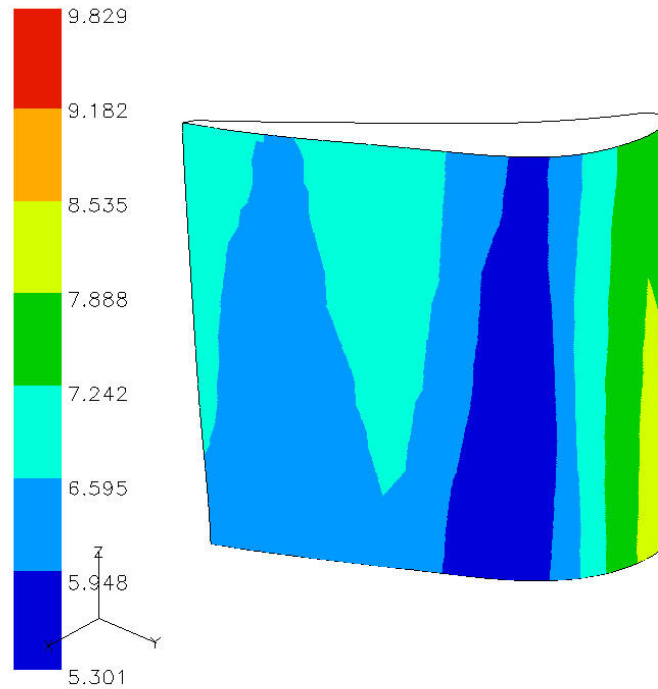
Fig. 3.15 Pressure in bar of the external suction surface
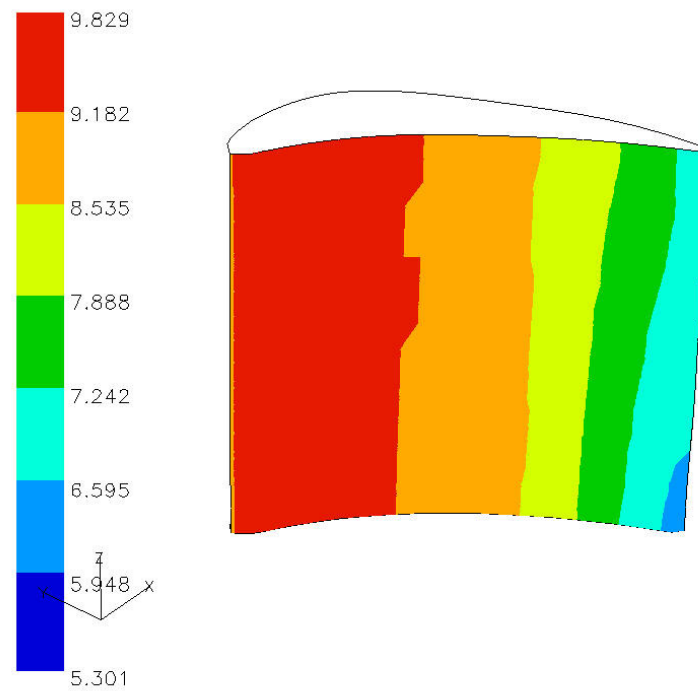
Fig. 3.16 Pressure in bar of the external pressure surface
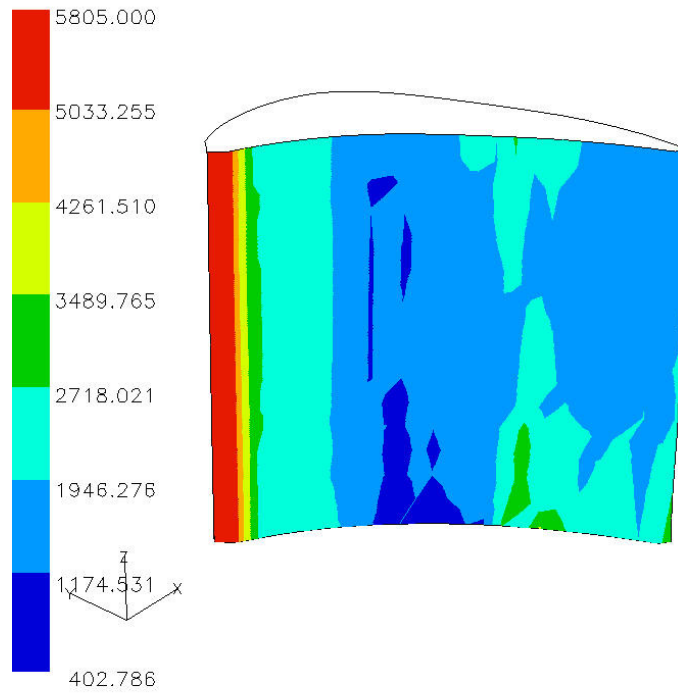
Fig. 3.17 Pressure surface heat transfer coefficients in W.m^{-2}.K obtained from STAN5
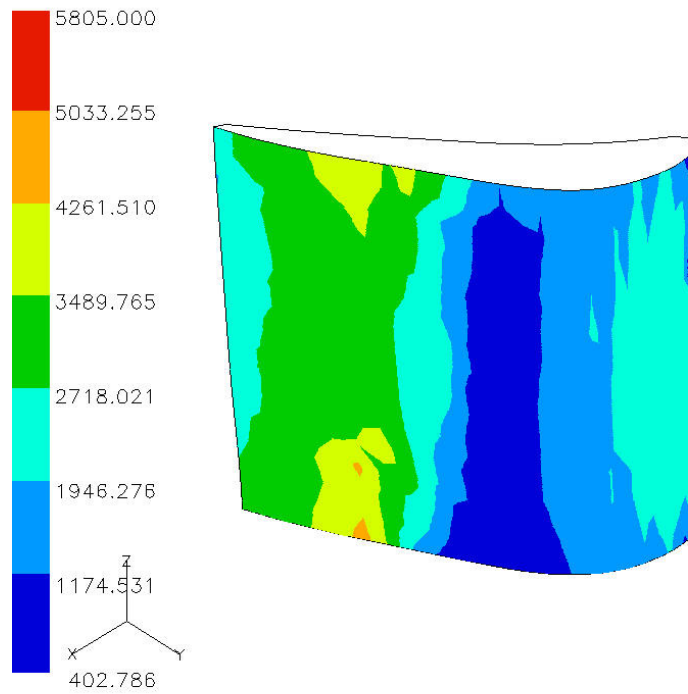
Fig. 3.18 Suction surface heat transfer coefficients in W.m^{-2}.K obtained from STAN5

Seventeen Sections through the blade were considered. Velocity gradients were altered in an iterative fashion until there were no signs of turbulent breakaway. Below, it can be seen that turbulent breakaway occurred towards the trailing edge of the blade when the velocity gradient became positive. This gradient change was forced not to occur and a gentle slope with constant gradient was imposed. The Abu-Ghannam and Shaw [52] model was used to predict the onset of turbulence.
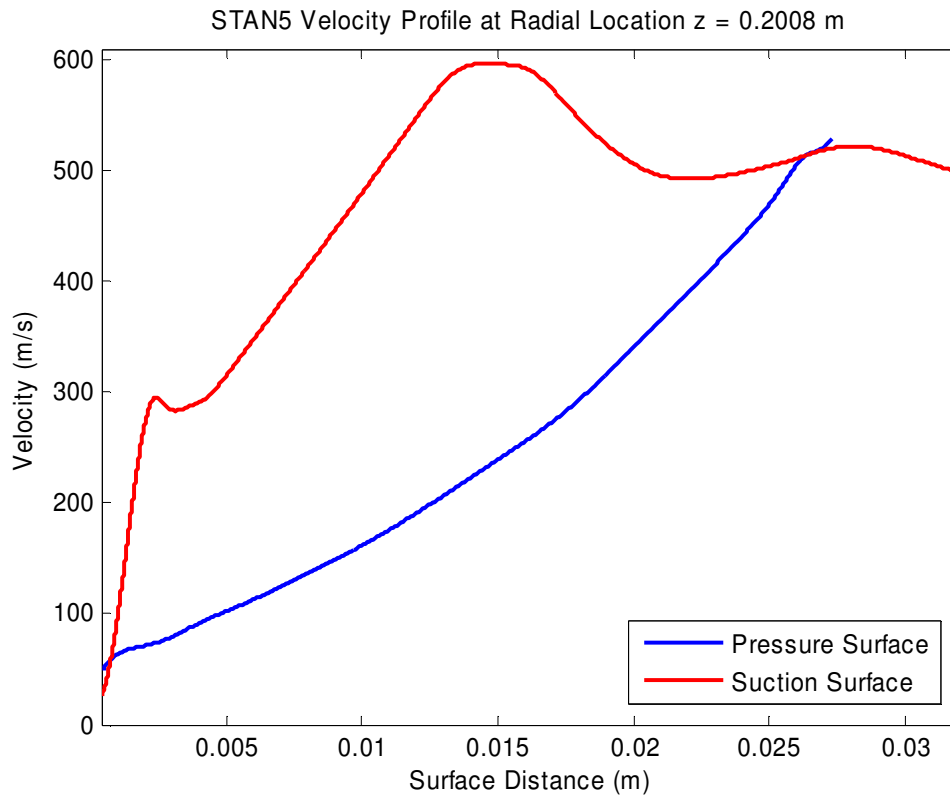
Fig. 3.19 STAN 5 velocity profile for slice 2 – unchanged velocity gradient
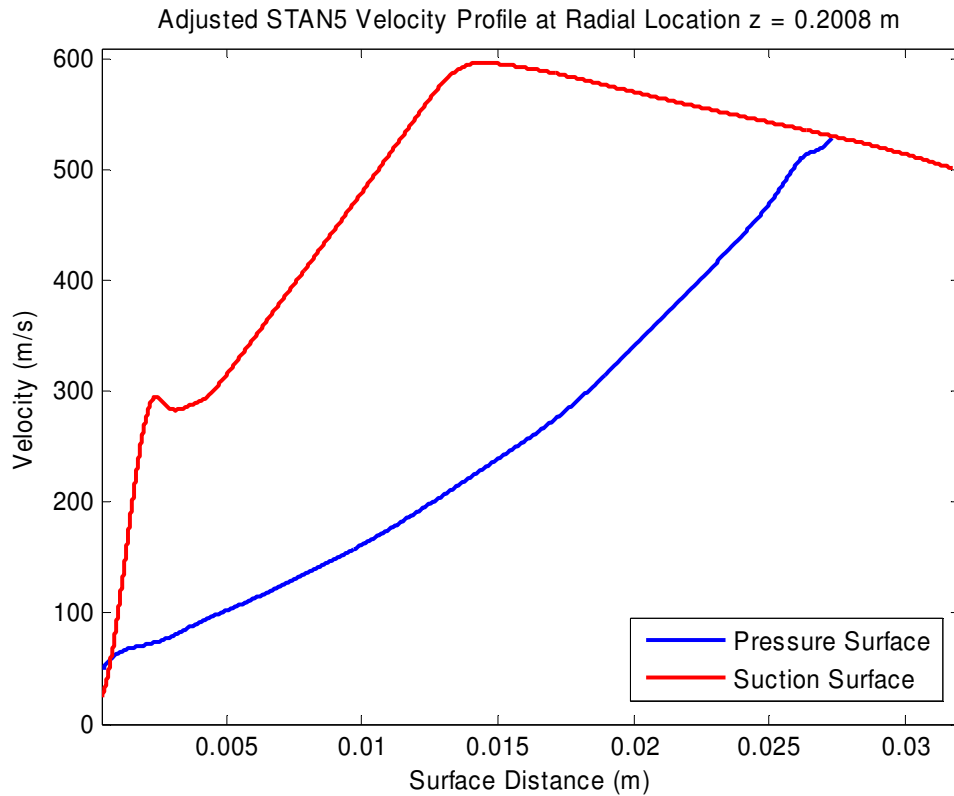
Fig. 3.20 STAN 5 velocity profile for slice 2 – changed velocity gradient

TACT1 uses the heat transfer coefficient and temperature data from STAN5. Values obtained using TACT1 were imposed on the external surface of the blade as a boundary condition when solving for the internal coolant flow. As with NREC and STAN5 slices were taken across the blade in the radial direction. Eight slices were considered for TACT1. Data from STAN5 was interpolated to fit these slices. Locations of impingement zones were stipulated in the radial direction with respect to the number of impingent zones, impingement hydraulic diameter, pressure, mass flow and temperature, plenum hydraulic diameter, dump hole location, hydraulic diameter and span between impingement zones. The physical geometry of the blade also had to be inputted in a geometry text file. Figure 3.21 is a representation of how the shape of the blade was generated. A maximum of 15 slices and 79 stations can be used. Stations are the points located on the external blade surface.

Although a semi-3D result was obtained from TACT1 it still had a 1D nature regarding the method used to calculate heat flux. TACT1 uses empirical correlations to solve for the Nusselt number with regard to impingement cooling in the presence of

cross-flow [33] and turbulent forced convection channel flow [39]. These correlations are used to calculate the heat flux at every station along the blade. Impingement correlations are only used at the stagnation point at station one. Channel flow correlations are used elsewhere. Station one is the station at the leading edge tip.
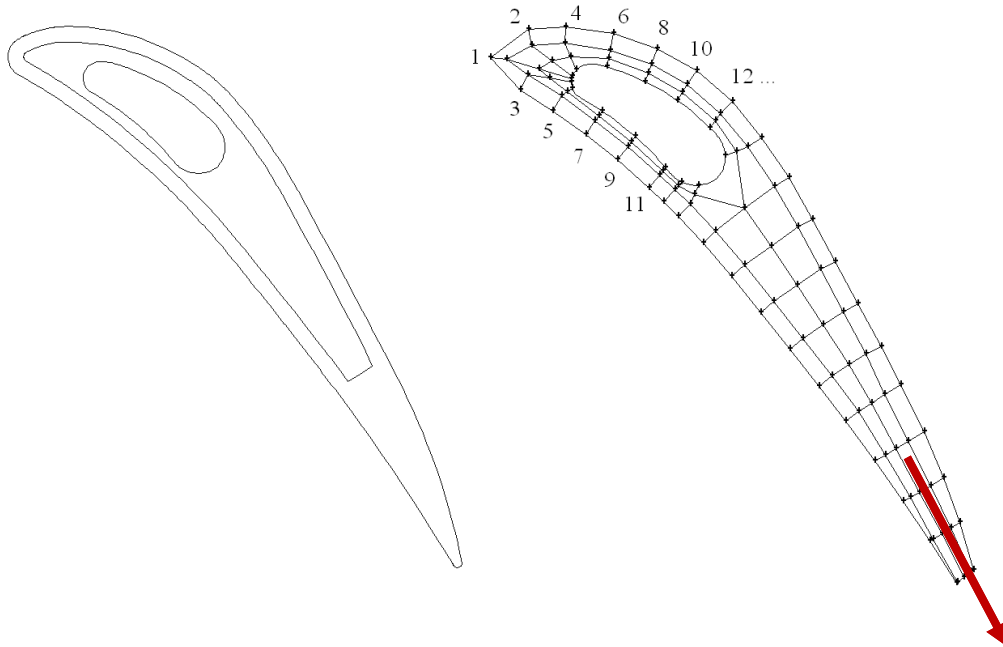
Fig. 3.21 The T56 NGV blade profile and converted TACT1 profile

Figure 3.21 indicates how the geometry was created for input into TACT1. From the original geometry seen on the left of Figure 3.21, stations were created on the outside of the blade. Stations were also created on the plenum as well as midway in the coolant flow channel and midway in the metal walls. Station 1 is the station at the leading edge where stagnation occurs. It can clearly be seen that the coolant fluid exits the blade at a slot at the trailing edge. This is not an exact representation of reality as the coolant fluid exits the blade at four distinct slots on the pressure surface and not at a single slot that runs through the entire radial length of the blade. This implies that the effect of film-cooling on the trailing edge was not taken into account.

3.4 Grid-independency study

3.4.1 Overview

It is essential to study and analyse the effects of the grid size on the numerical results obtained. Not only is it essential to study grid size on solution obtained, but grid size has a huge influence on what RANS model should be employed. Due to the complex flow phenomenon in the T56 NGV flow passages the k-ω SST model was used for the grid-independency study. Ideally, a grid-independency study using the k-ε model would have yielded a good indication of the applicability of these two models. However, the outcome of the literature survey in chapter 2 suggested that the k-ω SST turbulence model favours this particular type of flow.

3.4.2 Grid creation

Four grids were created for this study using the grid-generating software Gambit. Scaling factors were used to scale these grids as linearly as possible for all parametrical aspects. Triangular elements do not scale in the same ratio as hexahedral elements and as the scaling factors become smaller, the grids do not scale in an exactly linear fashion. The following ratios were varied within the grid:

- General spacing: This spacing was employed as a general interval size in the radial and chord-wise direction within the blade on the pressure- and suction-side.

- Skin thickness: This is the interval count of the thickness of the blade itself. It is the blade material separating the inside from the outside of the blade.

- Rib thickness: This interval count is the height of the ribs located in the chord-wise direction of the blade. There are ribs attached to the inside suction surface-side and internal pressure surface-side.

- Plenum and middle flow: This interval count represents the height of the fluid flow in the plenum chamber as well as the height of the fluid flowing in the

chord-wise direction towards the trailing edge. There are ribs attached to the inside suction surface-side and internal pressure surface-side. This interval count is the distance between the top and bottom ribs.

The following table represents the six meshes created for the grid-independency study:

Table 3.3 Grid creation parameters for grid independency study

Mesh	Elements	General Spacing	Skin Thickness	Rib Thickness	Plenum / Middle Flow
1	1 265 549	0.17	4	4	4
2	1 548 647	0.16	5	5	5
3	2 014 343	0.15	6	6	6
4	2 493292	0.14	7	7	7

3.4.3 Grid considerations
3.4.3.1 Skewness

It is imperative that the grids created correspond to each other in quality, which should be high. Figure 4.18 is a good indication of the skewness values as the number of elements increases. As a rule of thumb skewness up to 0.9 is allowed [36]. However, some models with complex flow regimes do not allow for this and it can happen that one cannot obtain all elements to exhibit skewness below this figure. This is not ideal and is an extreme case.

Worst Skewed Element Values
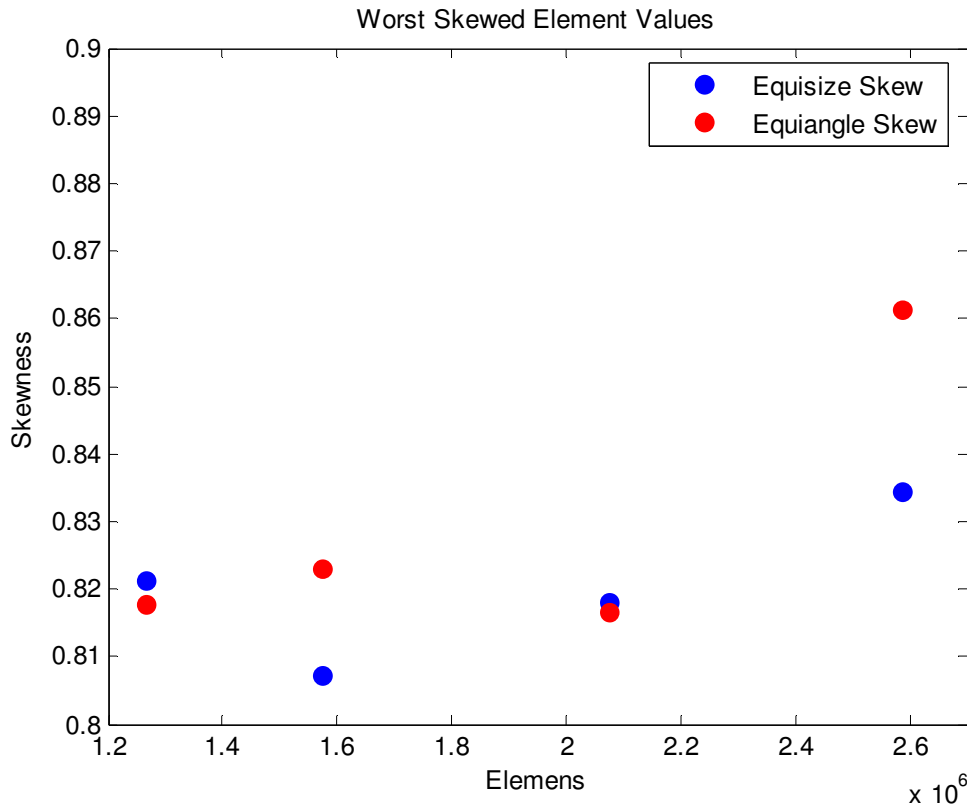
Fig. 3.22 Skewness of the grids

3.4.3.2 Y-plus

Y+ represents a local Reynolds number near the wall. Depending on which turbulence model and/or near-wall treatment is used, the guidelines for the appropriate *Y*+ values should be employed. For general tube or duct flow it is relatively easy to compute appropriate cell distances of the first cell on the wall. The T56 NGV flow field is complex to the extent that it becomes almost impossible to pre-calculate appropriate cell sizes based on known velocity fields.

This preliminary grid study thus also became a study identifying where the grid is too coarse, and where it could be refined. The k-ω SST model requires a *Y*+ value greater than 30 and smaller than 300, although the closer to 30 the better. From Figure 3.23, it can be seen that all four models were too fine.
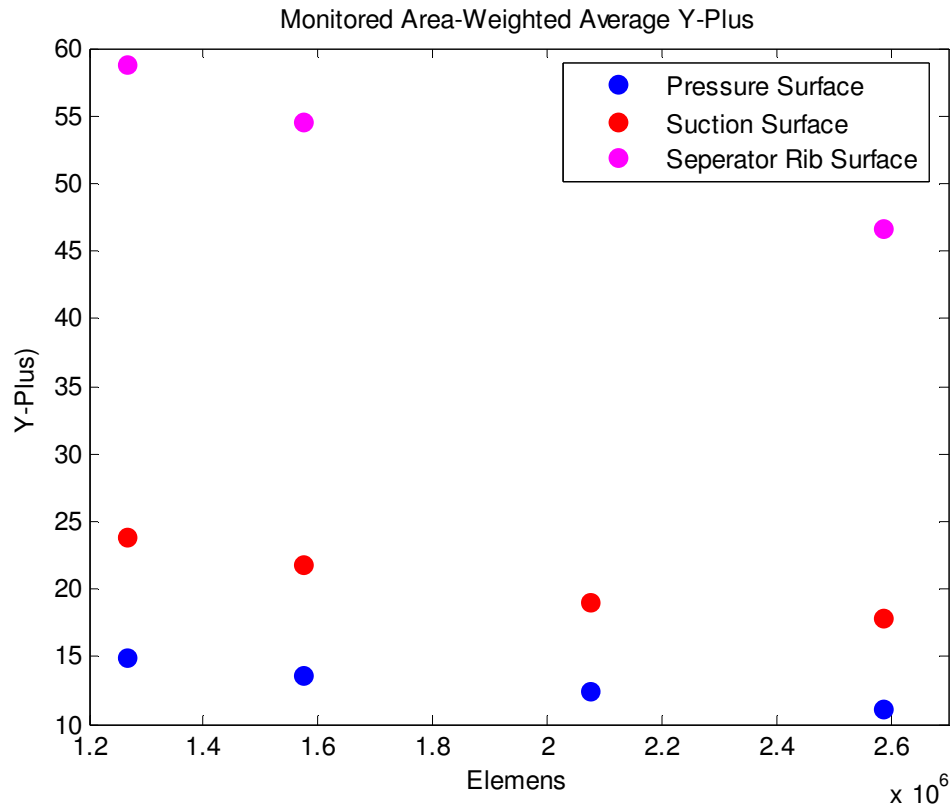
Fig. 3.23 Y+ values of ribs

3.4.3.3 Monitored surfaces

Temperature on the external blade surface, velocity on the four exit ports and pressure on the plenum inlet were monitored *(see Figures 3.24 and 3.25).* Outlet velocities seemed to remain relatively stable regardless of the element increases *(see Figure 3.26).* Temperature values dropped as the element size increases. This cannot necessarily be attributed directly to the element increase but could be a result of the *Y+* values located in the buffer layer.
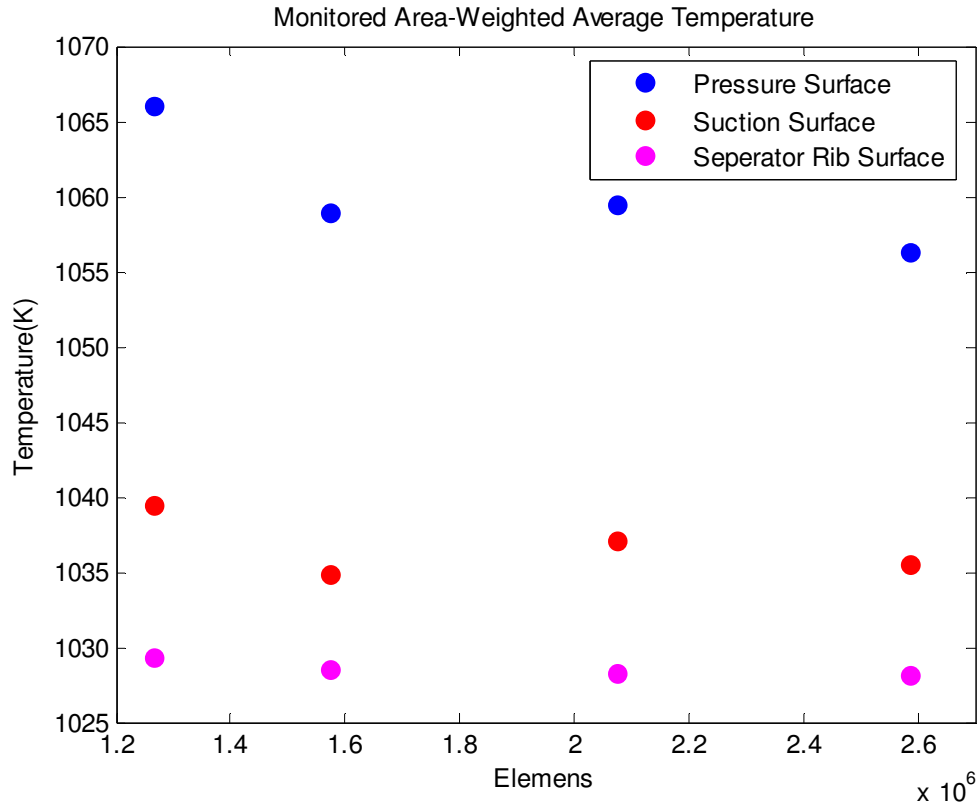
Fig. 3.24 Temperature plots of monitored surfaces
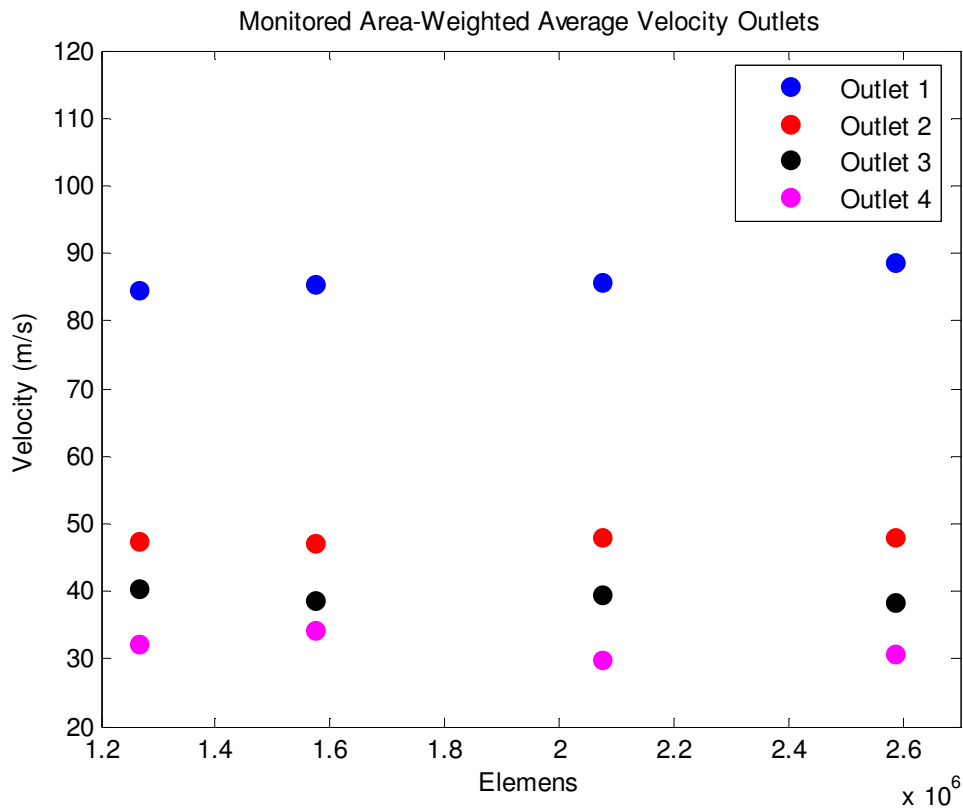
Fig. 3.25 Velocity plots of monitored surfaces

3.4.3.4 Conclusion drawn, grid recommendations

It can be seen clearly that these four models would not have been valid, due to the incorrect values of *Y+*. It is also noted that if the grid were to satisfy required *Y+* values of smaller than five for the low Reynolds number variant of the k-ω model, the grid would have to be larger than 30 million elements (the grid either needed to be coarser or extremely fine). It is this restriction that makes the modelling of this particular problem so complex and computationally intensive. It would not have been feasible to create a grid that was fine enough with *Y+* values below five and it appeared that the only feasible way for modelling the entire flow domain would have been that of using the wall function approach with the appropriate *Y+* values greater than 30. However, when a wall function approach were to be used, separation and vortex formation cannot be predicted.

A detailed study was to be conducted using only a quarter of the blade where the two methods (a low Reynolds number and a high Reynolds number approach) would be compared with each other. This would not entirely be a representation of the truth but it would yield insight into the conductive properties that exist within the blade and trends that are established.

3.5   Computational grid

3.5.1   Coarse mesh

A coarse grid was created satisfying the *Y+* conditions of having values from 30 to 300 *(Figure 3.26 – Figure 3.32)*. This approach used an enhanced wall treatment where wall functions were used to solve for the viscous sub-layer. The grid seemed to be too coarse, resulting in poor capture of heat transfer. Figure 3.26 shows the grid size on the pressure surface. It gives a good indication of the mesh size in the radial direction. This again can be seen from Figure 3.27 and Figure 3.28 where isometric views of the suction and pressure surfaces are shown. The grid was created by creating the casing cross-sectional surface grid first and then extruding this mesh in the radial direction along the blade. The casing surface grid is represented in Figure 3.29 to Figure 3.31. Figure 3.32 shows the grid at the trailing exit ports.
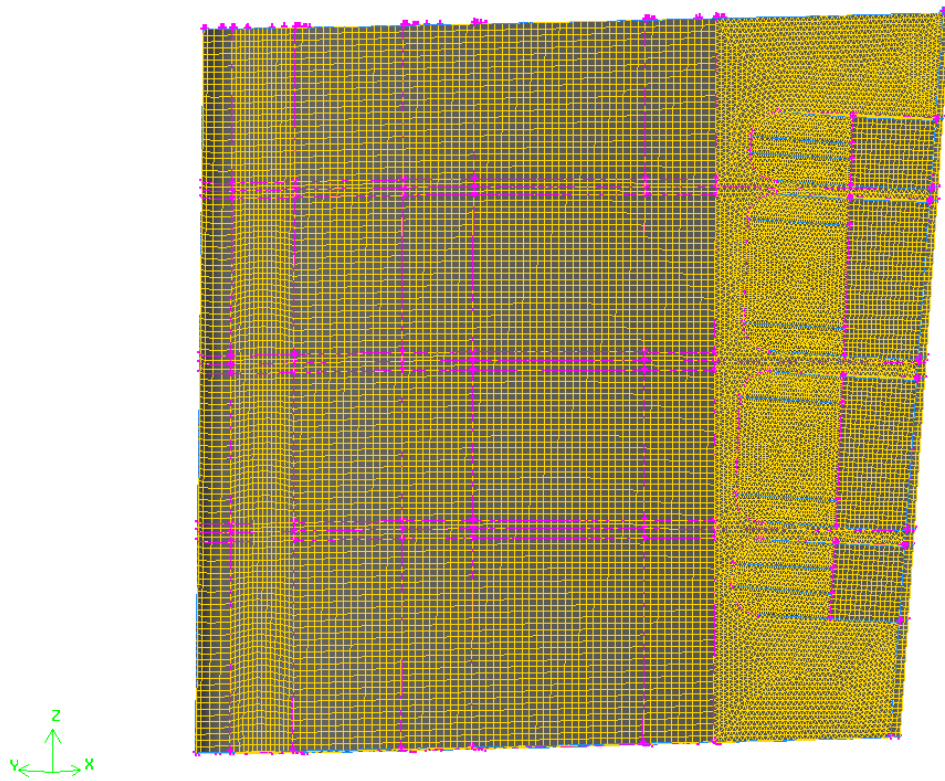
Fig. 3.26 T56 NGV tapered blade from hub to Casing
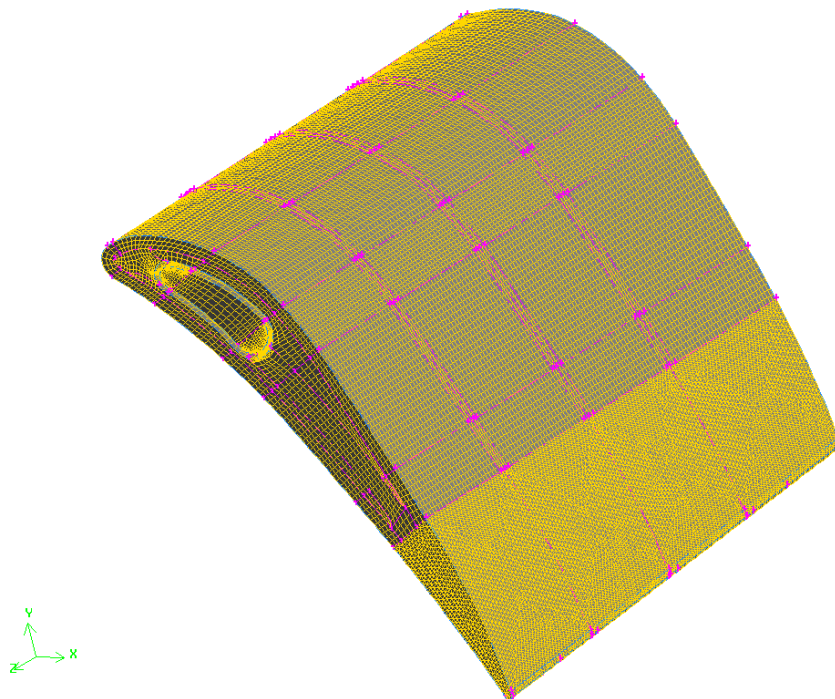
Fig. 3.27 Computational grid of entire domain – suction surface
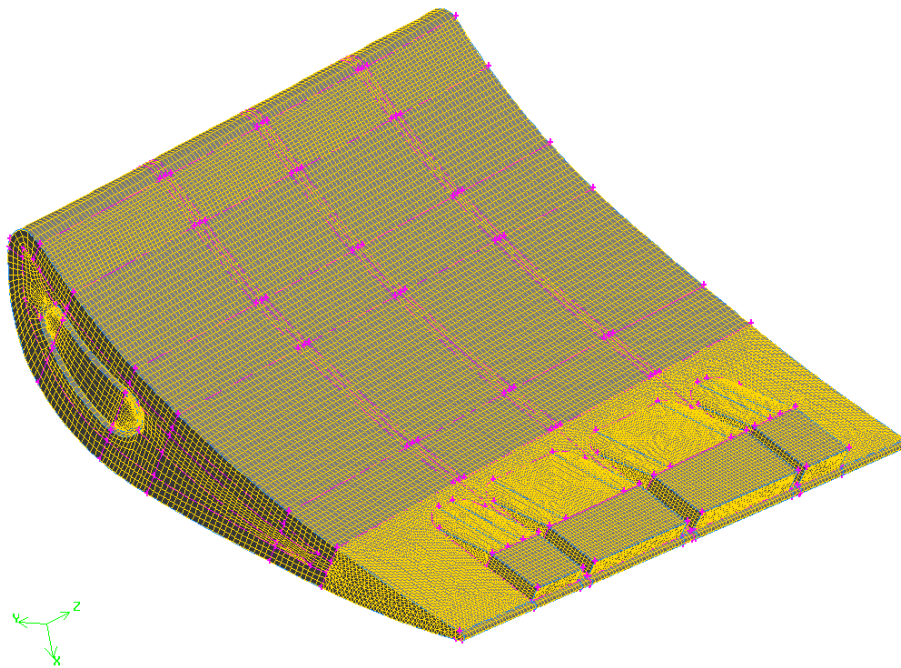
Fig. 3.28 Computational grid of entire domain – pressure surface

Plenum Solid
(Not Modelled)
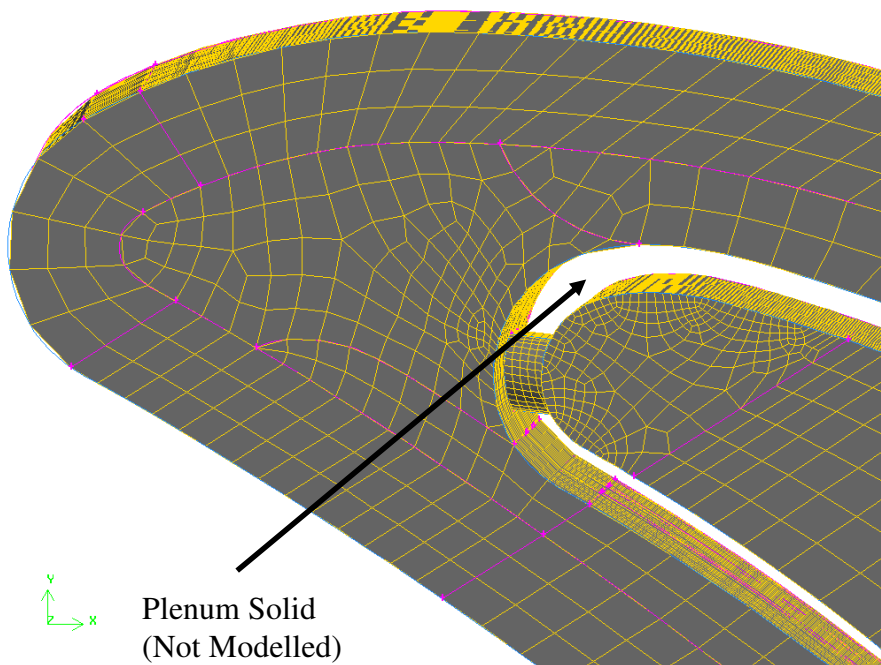
Fig. 3.29 Leading-edge grid to be extruded in the radial direction

Plenum Solid
(Not Modelled)
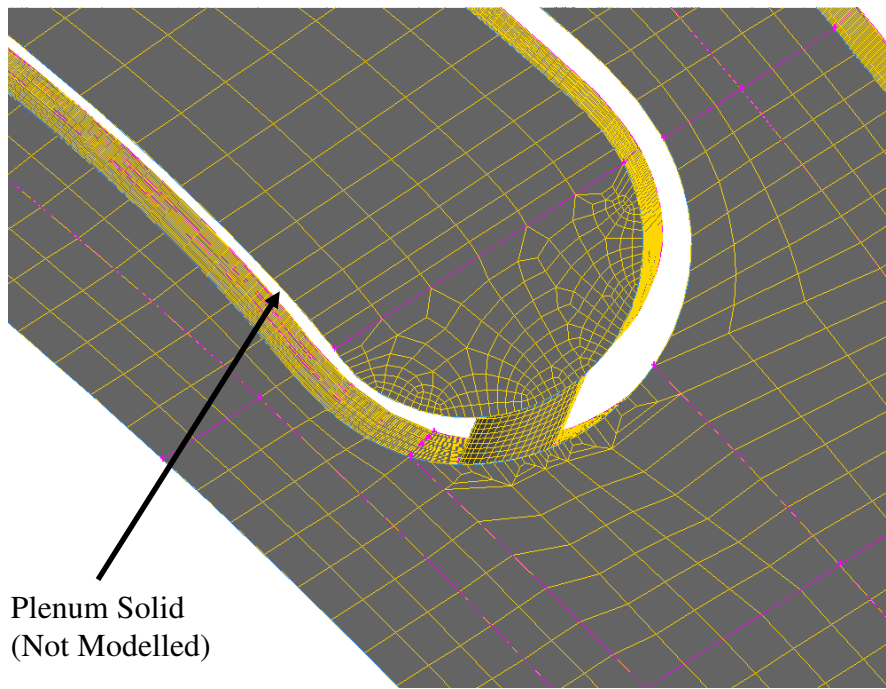
Fig. 3.30 Middle section grid to be extruded in the radial direction
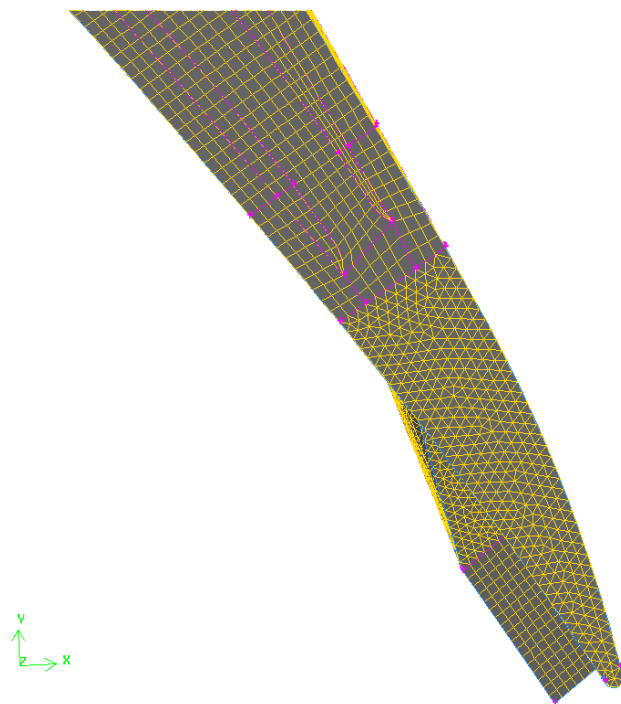
Fig. 3.31 Paved trailing-edge grid

The plenum solid was not modelled. The plenum was not represented by a solid body and thus was not meshed. This can be seen clearly in Figure 3.29 and Figure 3.30. The temperature gradient through the solid walls of the plenum insert was negligible. Due to the small gradient, the metal temperature remained almost constant throughout its thickness causing no or minimal conduction from the plenum coolant to the coolant between the ribs. Adiabatic boundary conditions were assumed at the casing and hub. Had this not been the case, conduction would have been present between the plenum walls and the casing and hub. Not enough information is known about the cooling of the hub and casing and thus no assumptions could be made. This research deals with a comparative study between two methods of resolving flow and heat transfer and thus this assumption was made for both cases. Radiation from the nearby can-annular combustors would also have to be taken into account as well as conduction from the combustor gases to the hub and casing walls.

The plenum metal insert was not meshed due to the adiabatic assumption causing the mesh of the entire domain to be of better quality. The solid plenum would have to consist of triangular elements, causing problems at the interface with the plenum coolant inside the plenum as well as with the trailing-edge coolant.

For ease of meshing, the plenum leading edge holes and trailing hole are connected through interface boundary conditions. Interfaces were also used to link the plenum holes with the leading-edge mesh. These boundary conditions were not ideal but did ease meshing operations.
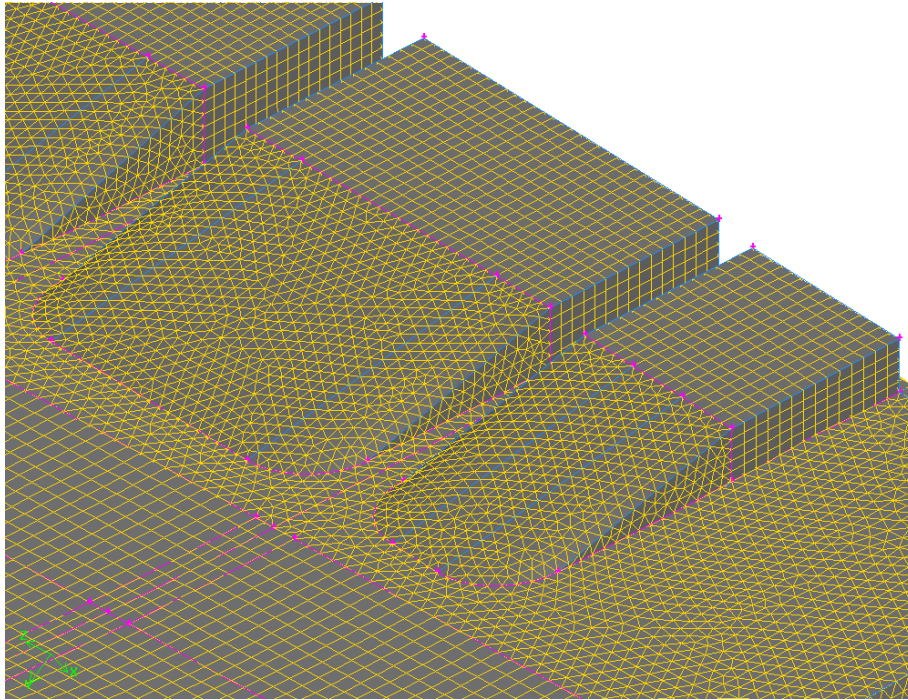
Fig. 3.32 T56 NGV trailing-edge – triangular elements

Although most volumes were mapped or extracted towards the radial direction of the blade, it was impossible to do so for the trailing edge. This was due to the fact that the four exit ports were located in this region where the coolant gas was ejected out of the blade and merged with the combustor gases. See Figure 3.32 for the representation of where the hexahedral elements merge with the triangular ones. The trailing-edge section was thus filled with triangular elements. These elements are in general avoided, however when the computational domain is too complex one is forced to use them.

The quality of the grid also plays a big role. As discussed earlier, elements with skewness values above 0.9 should be avoided. With complex shapes, such as these exit trailing ports where triangular elements are used, skewness becomes a problem and it is not uncommon to find skewness values in these regions higher than 0.9. The worst element for this domain was found in this region and had an equiangular skewness value of 0.927 and an equisize skewness of 0.915. Although not ideal, these values were acceptable.

3.5.2   Fine mesh - Section model

The T56 blade has three separator ribs dividing the flow domain into four distinct flow regions. The separator blades, however, did not cut the blade completely in four sections and flows could still interact with those of other sections at the leading edge. The assumption of symmetry in the radial direction was made at this region.

Due to the complexity of the geometry considered, the hub faces were meshed using unstructured quad elements with sizing functions imposed where applicable. This yielded a mesh size of approximately 7.7 million elements. Of these elements roughly 7.2 million were quadrilateral elements, 34 000 were tetrahedral elements and 473 000 were pyramid elements.

Figure 3.33 to Figures 3.36 give a good indication of how the mesh was constructed. All surfaces had sizing functions to ensure proper resolving of the boundary layer. This mesh was to be used when solving for the low Reynolds number approach. Computational resources restricted this mesh to no greater than eight million elements. It was therefore not feasible to solve for the entire blade using the low Reynolds number approach as elements in the order of 30 million would have been required. The reason why the meshed domain needs to be constructed with such a vast amount of elements was due to the *Y+* restrictions being present when solving a low Reynolds number simulation. *Y+* values were suggested to be in the order of less than five. When thermal effects are taken into account, *Y+* values should preferably be in the region of lower than two or one.
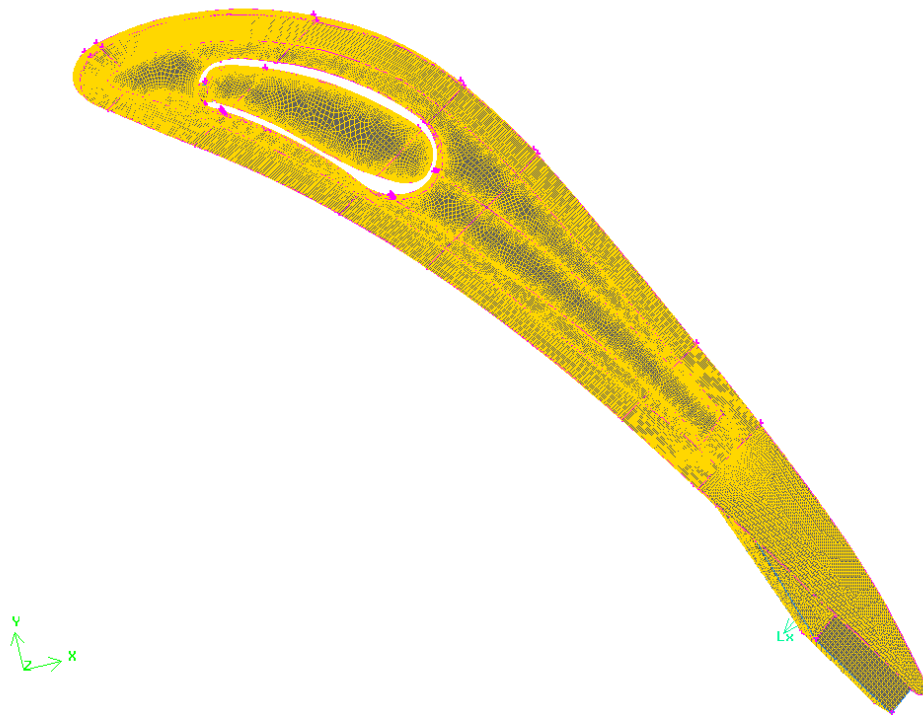
Fig. 3.33 T56 NGV section – Grid mapped through the blade in the radial direction
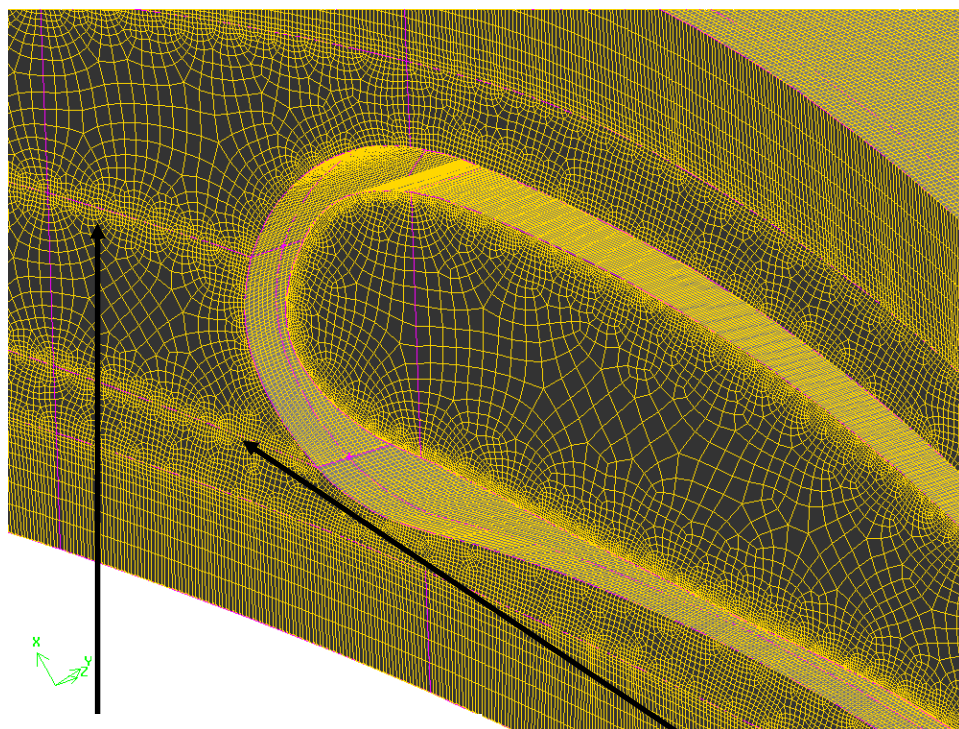
Interface between top ribs and fluid

Interface between bottom ribs and fluid

Fig. 3.34 Face mesh used for mapped volume mesh

Figure 3.34 reveals that the mesh has been grown larger towards the centre of the flow domain where wall-bounded effects became negligible.
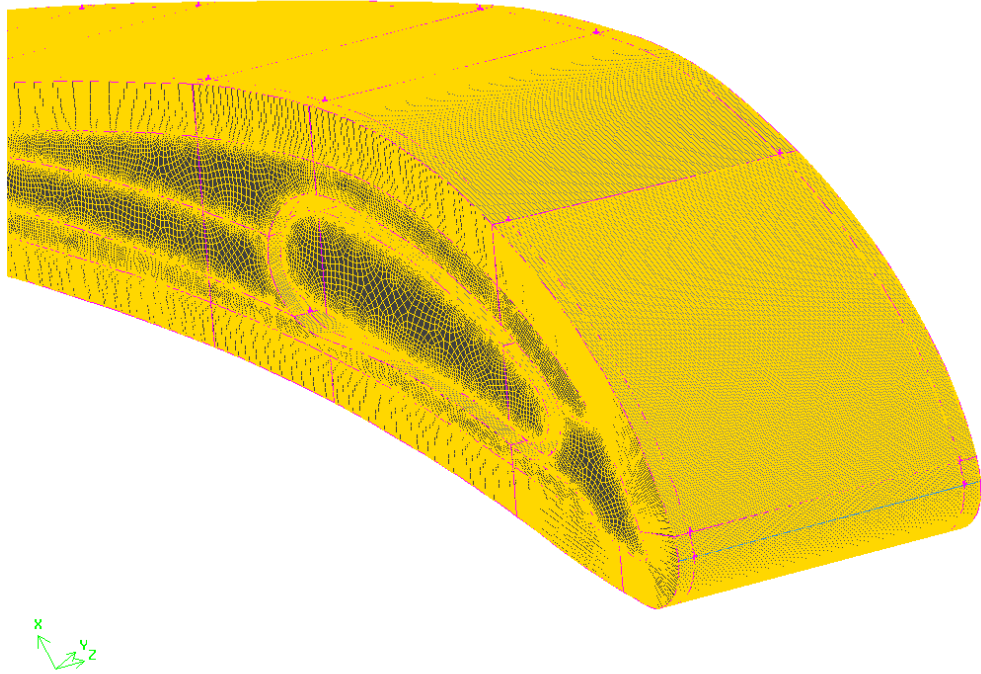
Fig. 3.35 Isoview of meshed section
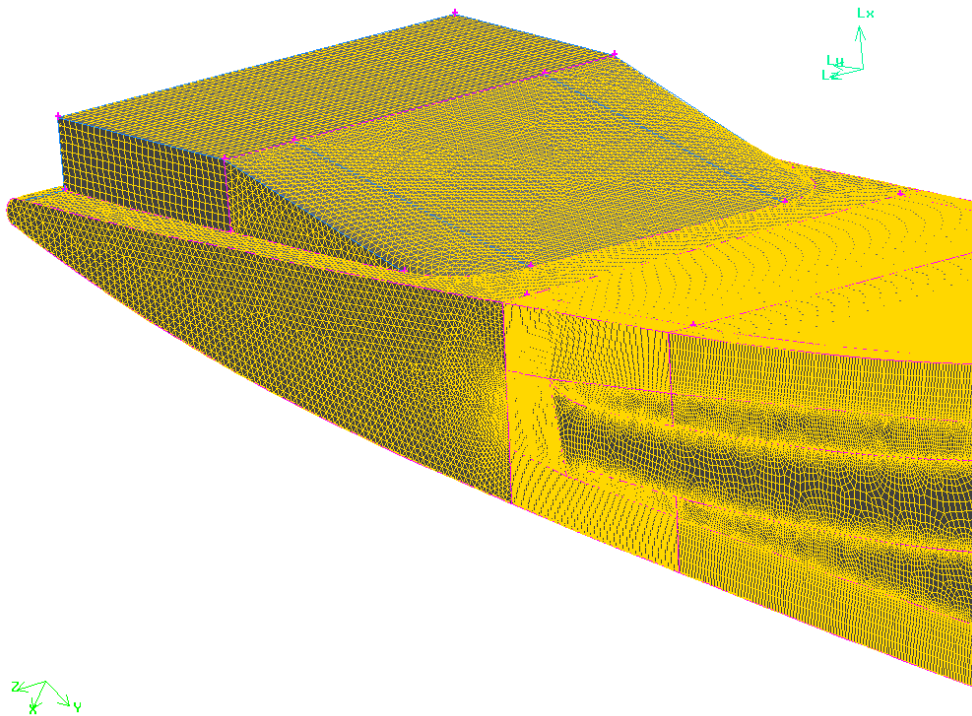
Fig. 3.36 Trailing edge exit port

3.6   Conclusion

An in-depth analysis of the T56 turbine engine yielded the boundary conditions necessary for this CFD study. A worst case scenario was assumed for derivations of these conditions as well as conservative assumptions regarding losses both within the turbine engine itself as well as in the CFD model.

The grid independency study done yielded a great deal of insight into the difficulties surrounding this study. It was established that it was not feasible to solve the entire flow domain using the low Reynolds number k-ω turbulence modelling approach. However, using wall functions, the entire domain could easily be solved.

Acceptable results were obtained using a combination of the standard k-ω turbulence modelling approach as well as a low Reynolds number variant where only a section of the blade is considered with mapped thermal boundary conditions at the hub and casing side of this section obtained from the coarser model.

CHAPTER 4

RESULTS AND DISCUSSION

SUMMARY OF CONTENTS

FLUENT RESULTS

TACT1 RESULTS

COMPARATIVE STUDY

CONCLUSION

4.1   FLUENT results

4.1.1   Case study 1 – Coarse domain

The first case study considered is a model of the entire blade. The k-w-SST option in FLUENT as defined by Menter [53] with the standard wall function approach [36] was used for solving this case. See Chapter 2 for details on this turbulence model. As stated before, the hub and casing have assigned adiabatic boundary conditions attributed to them. The results in Figures 4.1 to 4.5 are oriented such that the hub is always at the bottom of the Figure and the casing at the top. The contour plots were created in order to establish the thermal gradients present and their order of magnitude. The patterns of these gradients are also of interest and were compared with the other models as depicted in table 4.1. It is evident that the results from FLUENT and TACT1 will not exactly correspond to each other due to their respective methods of solving. However, what is of importance is the trends and their behaviour. Table 4.1 summarises the various FLUENT cases considered. These cases are compared with the TACT1 results obtained.

<div align="center">Table 4.1 Summary of Case Studies</div>

Case Study	Elements	Model
1	451,062	Coarse Domain
2	112,195	Coarse Section
3	112,195	Coarse Section with Temperature Profiled Hub/Casing
4	7,698,702	Fine Section
5	7,698,702	Fine Section with Temperature Profiled Hub/Casing

Case study 1 is the most important of all of the case studies as this is a representation of the entire domain considered. This was also the first case to be modelled. The fine sectional model represented by case study 5 yielded more accurate results and secondary flow fields were resolved properly, a phenomenon which would not be captured by the wall function approaches.
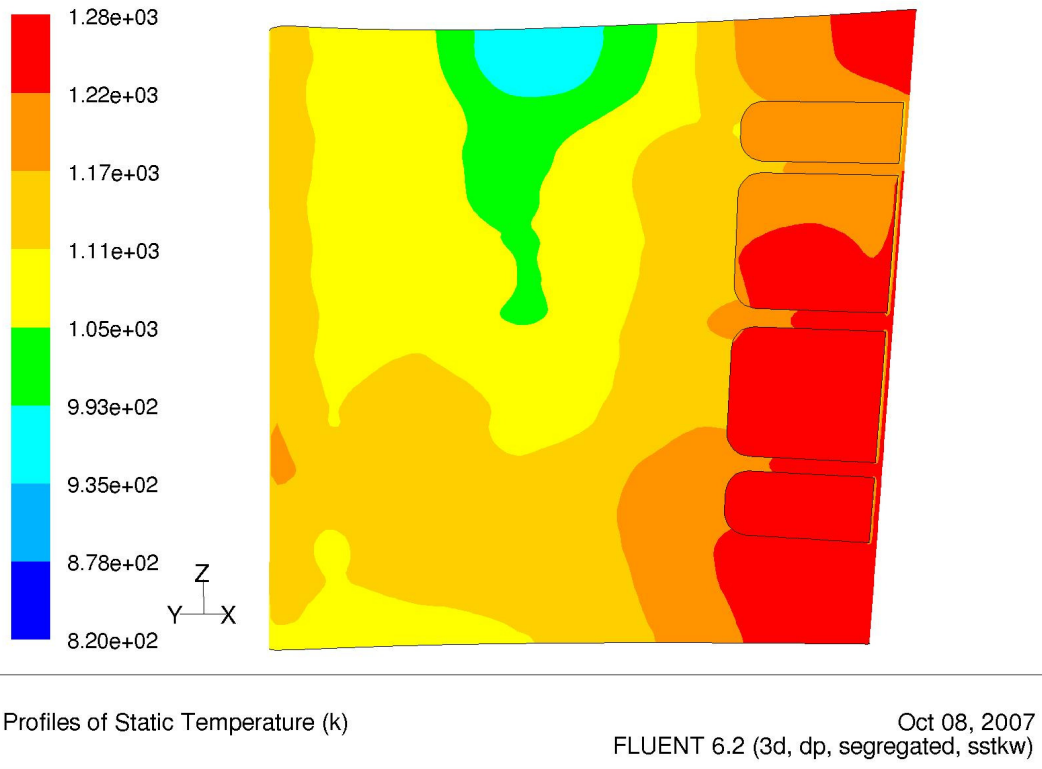
Fig. 4.1 Temperature distribution of external pressure surface of the domain – Case 1
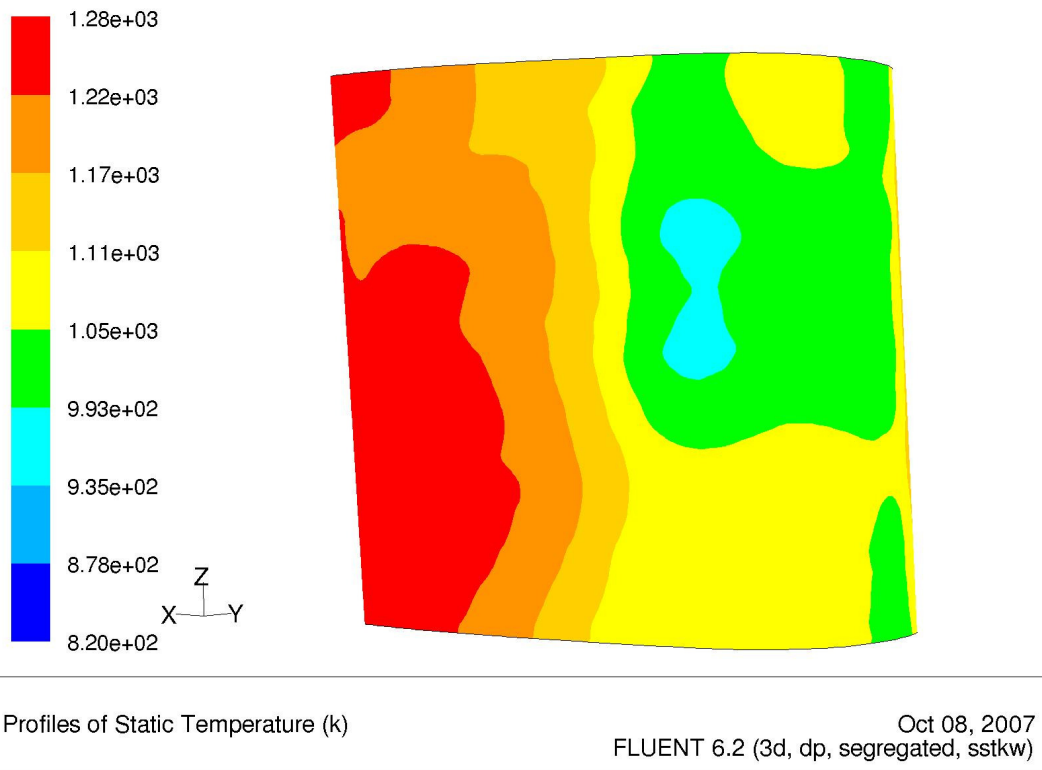
Fig. 4.2 Temperature distribution of external suction surface of the domain – Case 1
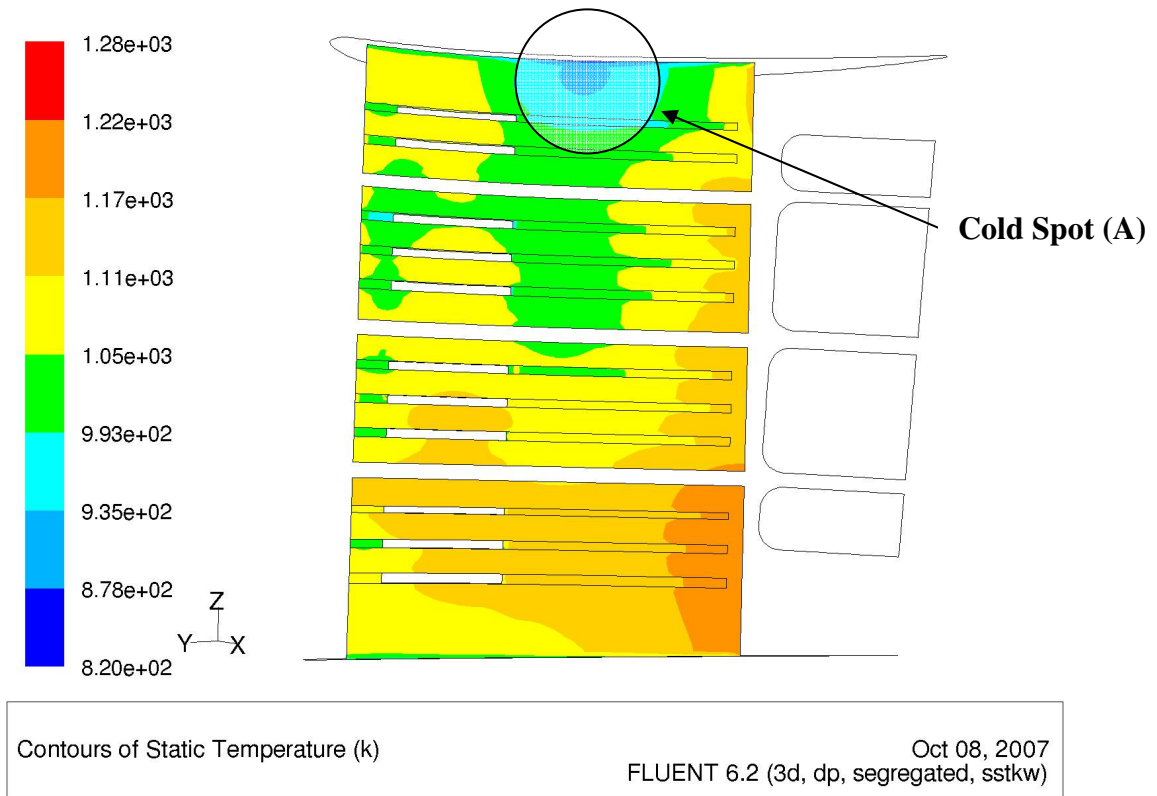
Fig. 4.3 Temperature distribution of internal pressure surface of the domain – Case 1
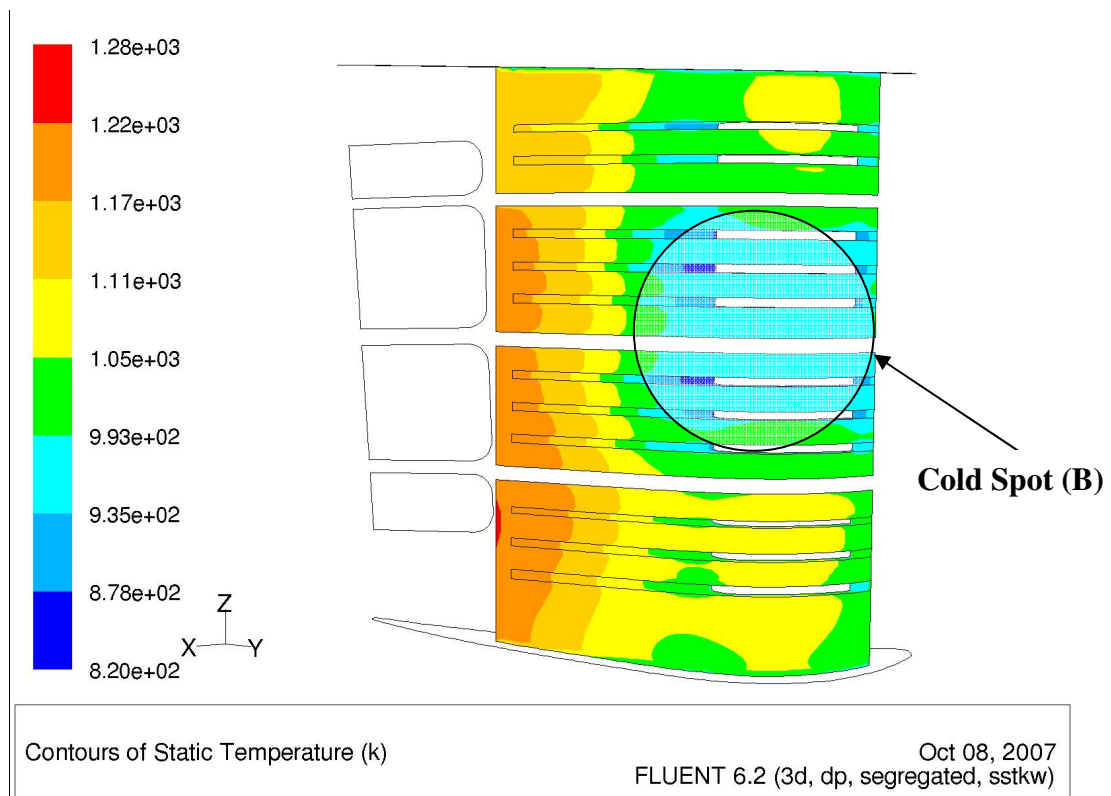
Fig. 4.4 Temperature distribution of internal suction surface of the domain – Case 1

The contour plots in Figures 4.1 to 4.4 yield great insight into how the flow field behaves and the effects it has on thermal conduction. As expected, the hottest areas of the blade are at the leading and trailing edges. This is attributed to the fact that the leading edge was the closest to the combustor outlet and thus faced the highest temperatures. The trailing tip has no internal cooling ducts and was relatively thin compared with the rest of the blade and thus this was also a high-temperature region.

Flow through the plenum dump hole, which is located at the furthermost section from the hub, impinged on the internal pressure surface which caused this local area to be cooled via direct jet impingement cooling *(labelled A in Figure 4.3)*. The dump hole is not a coolant hole as such but a hole to account for the absolute pressure loss through the plenum. Due to geometry interpretations, all the FLUENT models assume this hole to act as an impingement hole. TACT1 cannot model this impingement, due to code restrictions. The geometry analysis of the T56 plenum yielded a geometric model where all the impingement holes and the dump hole actually showed to impinge on the pressure surface.

A similar cold region exists on the suction surface midway between the hub and the casing *(labelled B in Figure 4.4)*. There is a general tendency for the suction surface to be cooler than the pressure surface. The cooler suction surface can be attributed to the fact that the impingement holes did not impinge on the concave surface found at the very internal leading-edge point but instead impinged on the pressure surface. This impinged air formed a very strong clockwise vortex that drove the flow of air towards the suction surface of the blade, from where it flowed to the trailing edge *(see Figure 4.5)*. If the flow, for example, were to impinge on the suction surface instead of the pressure surface, it would in general yield a colder pressure surface, due to a clockwise vortex forming. The strong clockwise vortex forces air to flow towards the trailing-edge along the suction surface rather than the pressure surface and thus to convectively cool this section to a greater degree than the pressure surface.
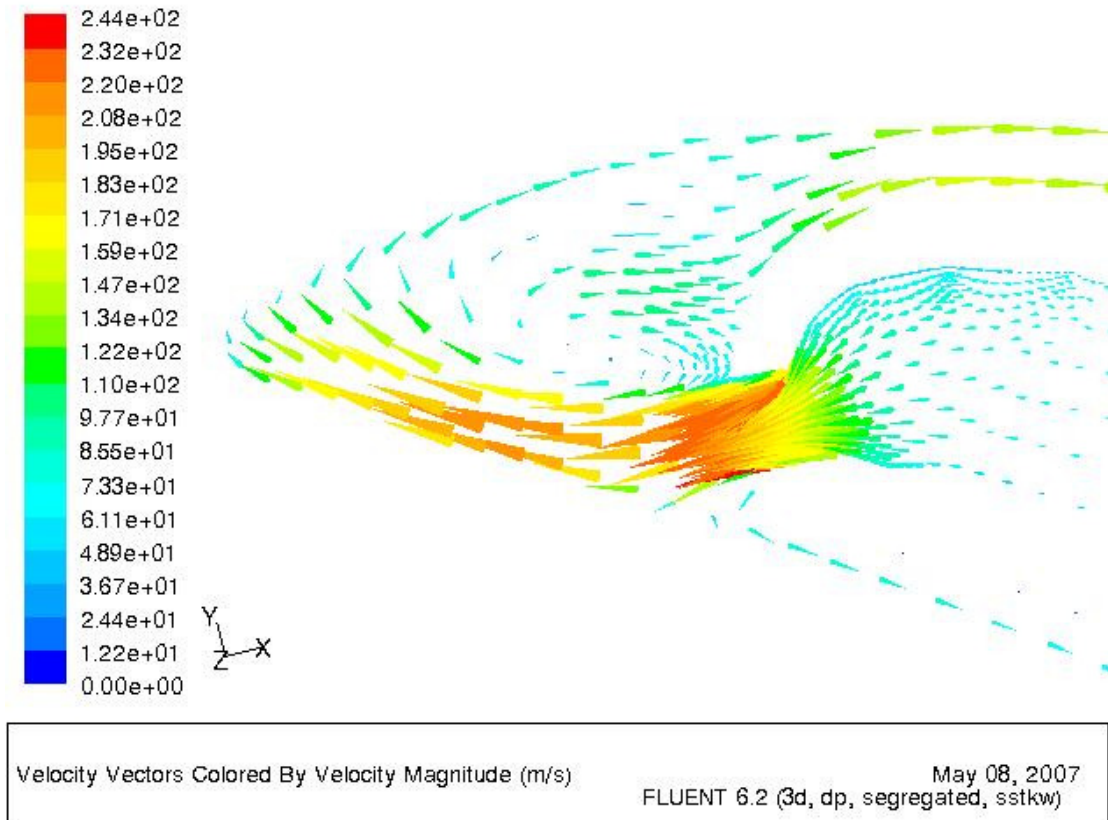
Fig. 4.5 Velocity vectors coloured by velocity magnitude

4.1.2   Case study 2 – Coarse section

As stated before, for all effective reasons, the blade can be divided into four sections via the three separating ribs. The second section as taken from the hub towards the casing was considered for all the sectional case studies, being case 2, 3, 4 and 5. The reason for using this section is its central location in the blade. Sections 1 and 4 were located at the hub and casing and would not have been ideal due to the adiabatic boundary conditions present at the hub and the casing. Thus a section had to be considered that was not bounded by either the hub or the casing. Even though case study 2 had adiabatic walls at the separator ribs, it was chosen to facilitate modelling for case study 3 where a temperature profile was mapped onto these two surfaces. Section 3 was ruled out due the fact that this section was next to section 4 that contained the dump hole. Comparative studies of FLUENT and TACT1 would have to be done and a section was selected that would most accurately correspond.

It was thus the purpose of this case study to establish the behaviour of conduction in the radial direction between the hub and the casing. The hub and casing boundary conditions of this section were kept adiabatic and thus the temperature distribution formed would only be due to the presence of the impingement hole in this section. No effects upstream or downstream would affect this section. This is not entirely accurate and from the domain model (case study 1) the extent of this temperature variation is known already. The k-w-SST turbulence model was employing a wall function approach.
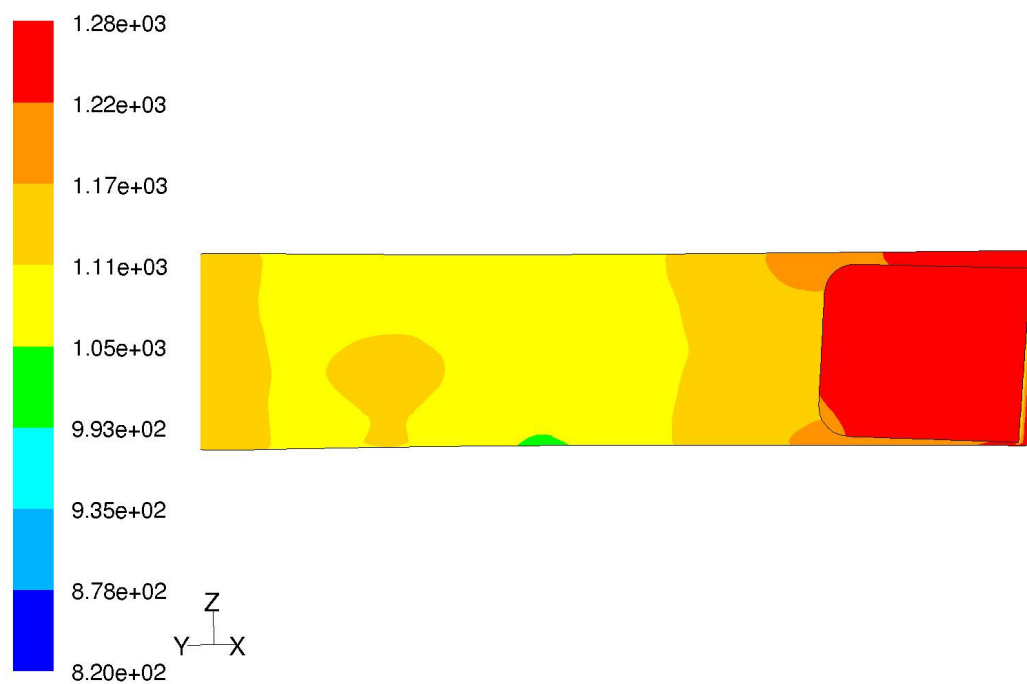
Profiles of Static Temperature (k)   Oct 08, 2007
                              FLUENT 6.2 (3d, dp, segregated, sstkw)

Fig. 4.6 Temperature distribution of external pressure surface of section 2 – Case 2
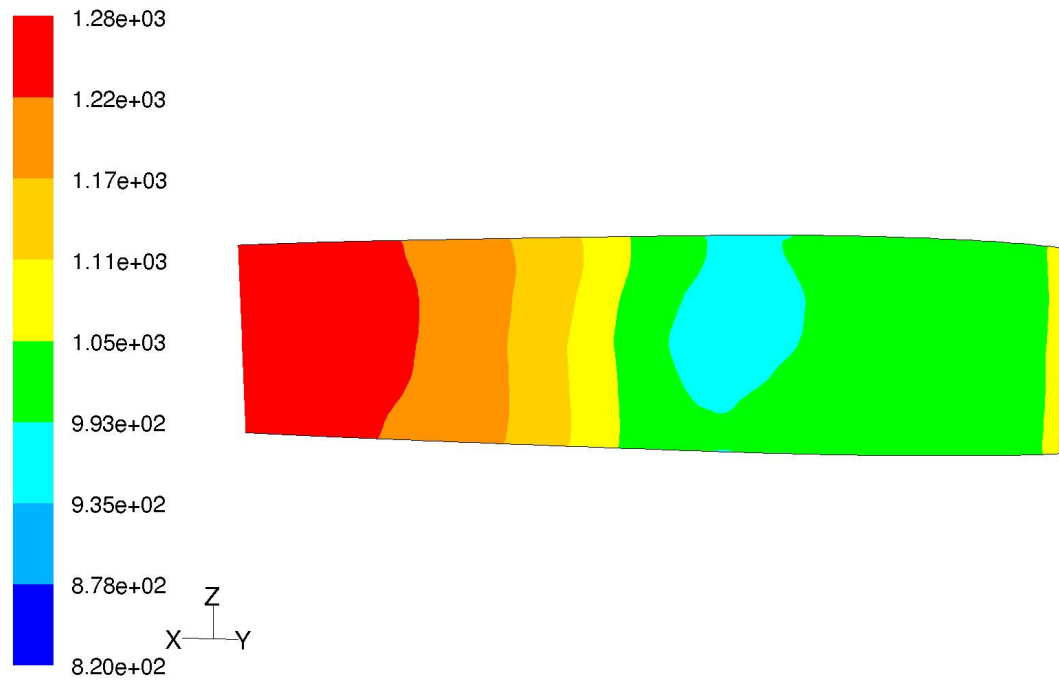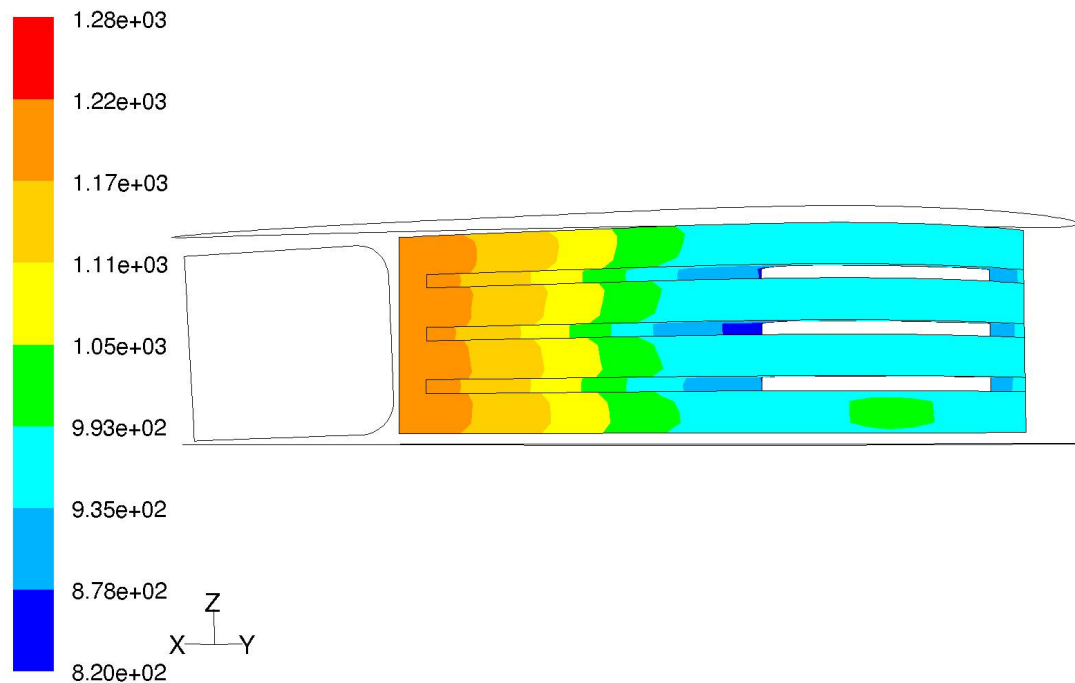
Fig. 4.7 Temperature distribution of external suction surface of section 2 – Case 2

Fig. 4.8 Temperature distribution of internal suction surface of section 2 – Case 2
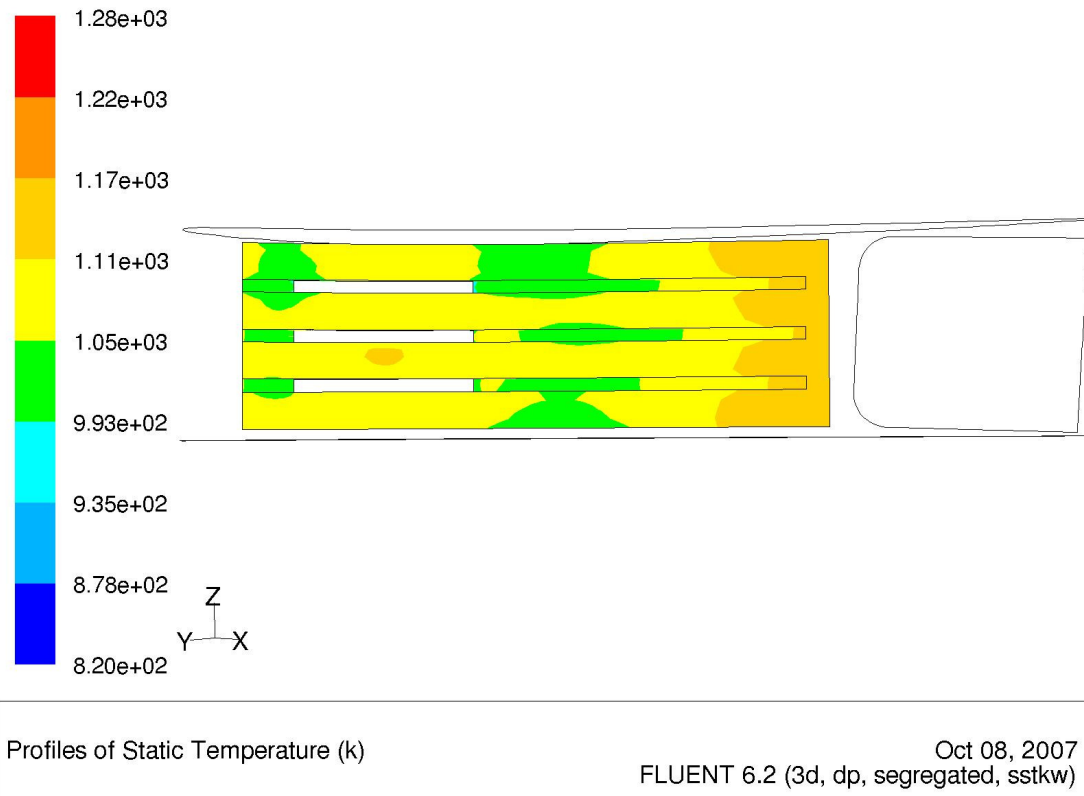
Fig. 4.9 Temperature distribution of internal pressure surface of section 2 – Case 2

Although external blade surface temperatures in general seem to be similar in magnitude and contour shape, the internal temperatures did vary from the domain model of case 1. Temperature distributions of this section were very symmetrical due to the adiabatic separator rib boundary condition imposed. This is shown in Figure 4.8 where contours intersect the hub and casing boundaries normal to their direction.

The sectional model of case 2 was in general colder than the domain model of case 1. This can be observed in the mid-section of the internal suction surface between the leading and trailing edges where a colder region exists. A similar cold spot is observed on the external suction surface as in case 1. This again is due to the way the jet impinged on the pressure surface forcing air to the trailing edge via the suction surface rather that the pressure surface. The temperature of this cold spot lies in the same region for both cases.

It is concluded that conduction in the radial direction is of great importance. This conductive behaviour is driven by thermal gradients formed due to the cooling

configuration of jet impingement and general convective cooling towards the trailing edge with the aid of ribs to increase the surface area for conduction.

4.1.3   Case study 3 – Coarse section with profiled hub/casing

As in case 2, it became clear that the thermal gradient imposed in the radial direction had a huge effect on the sectional temperature distribution. This case study evaluated the same section as in Case 2 but imposing a temperature profile obtained from the domain model (Case 1) on the hub and casing. This profile can be seen as a contour plot in Figure 4.10. In this section, the hub and casing refer to the separator ribs that form the two surfaces where the flow was bounded. As discussed earlier, the flow domain was separated into four flow regimes by separator ribs. This is also why there are four distinct exit ports. Figure 4.10 shows the temperature distribution on two of these separator ribs bounding one of these flow regimes.
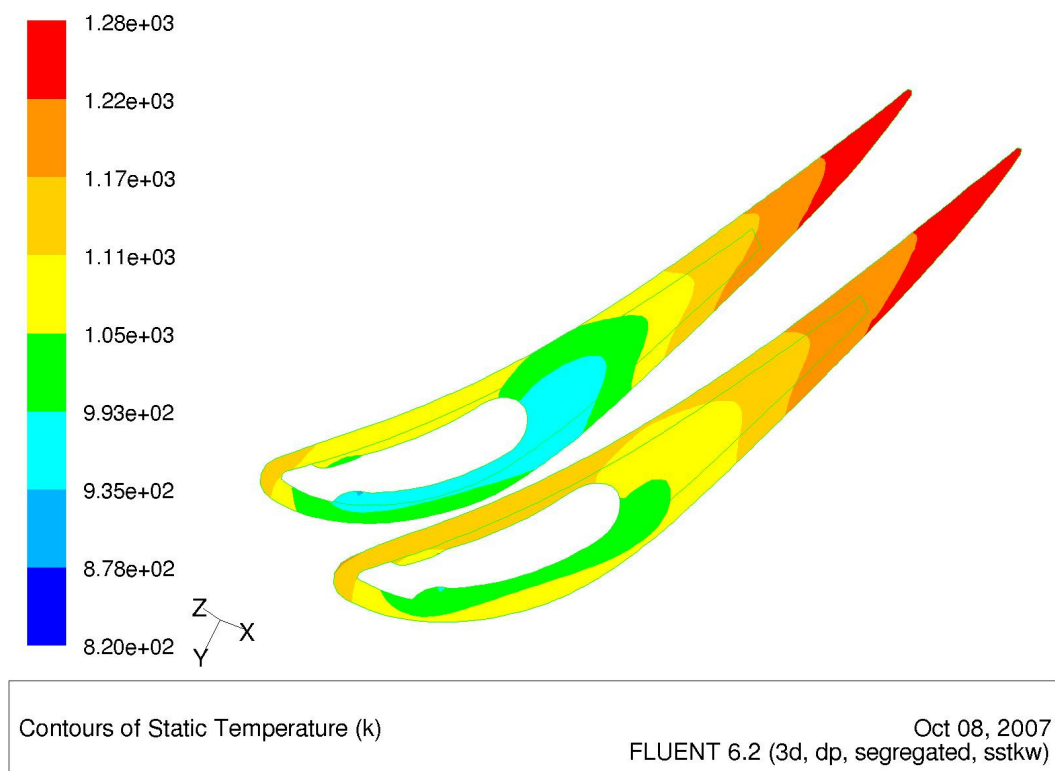
Fig. 4.10 Separator rib temperature profile

The first section as seen from the hub was a great deal hotter than the other sections, imposing a huge thermal gradient on the hub of this section. The reason for this hot

4.1.4   Case study 4 – Fine section

Even though it had already been established that a temperature profile should be imposed at the separator ribs boundary condition, a fine model which omitted this profile and had adiabatic boundary conditions at the hub and casing separator rib boundaries, were still considered. Once again as in case 2 the contours in Figures 4.16 to 4.19 intersected the boundaries normal to the contour direction. The purpose of this case study was a comparison between the fine model and the coarse model using a wall function approach. Figure 4.16 shows no real comparison with Figure 4.6 of case 2. This indicates that using a wall function approach has a strong influence on the flow field.
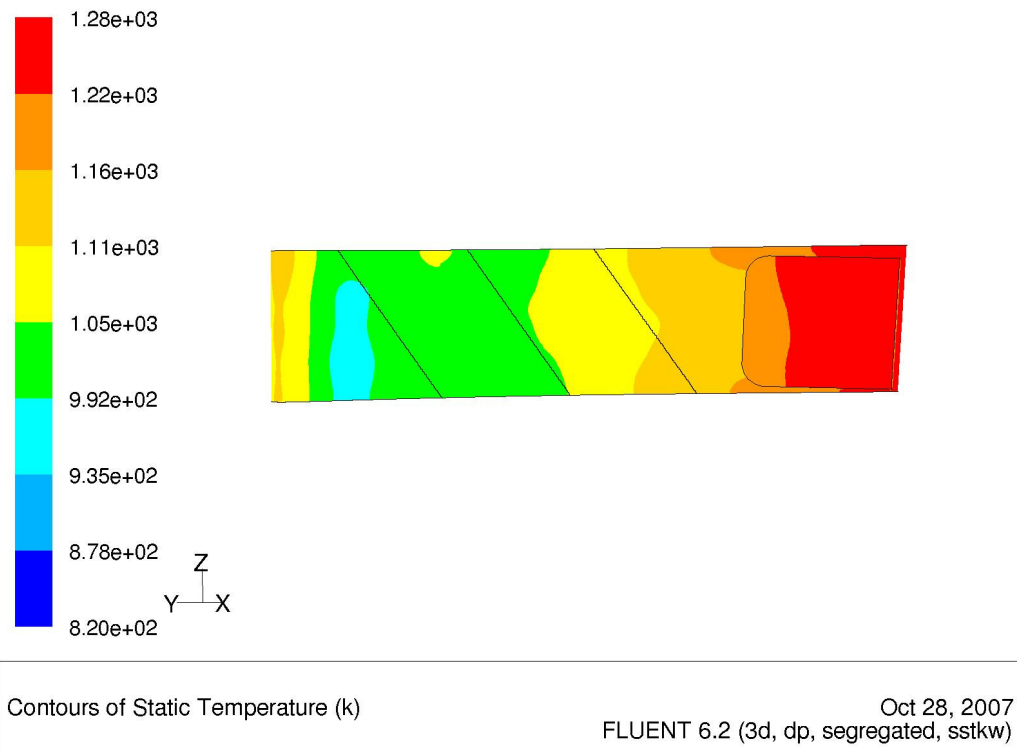
Fig. 4.16 Temperature distribution of external pressure surface of section 2 – Case 4
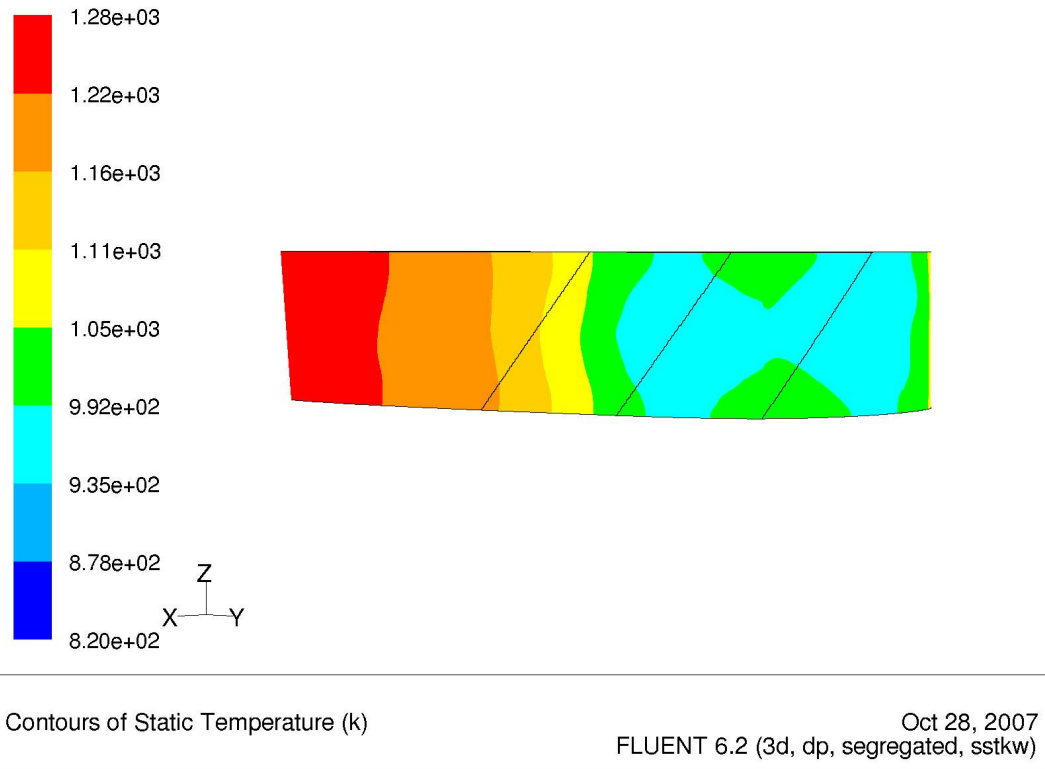
Fig. 4.17 Temperature distribution of external suction surface of section 2 – Case 4
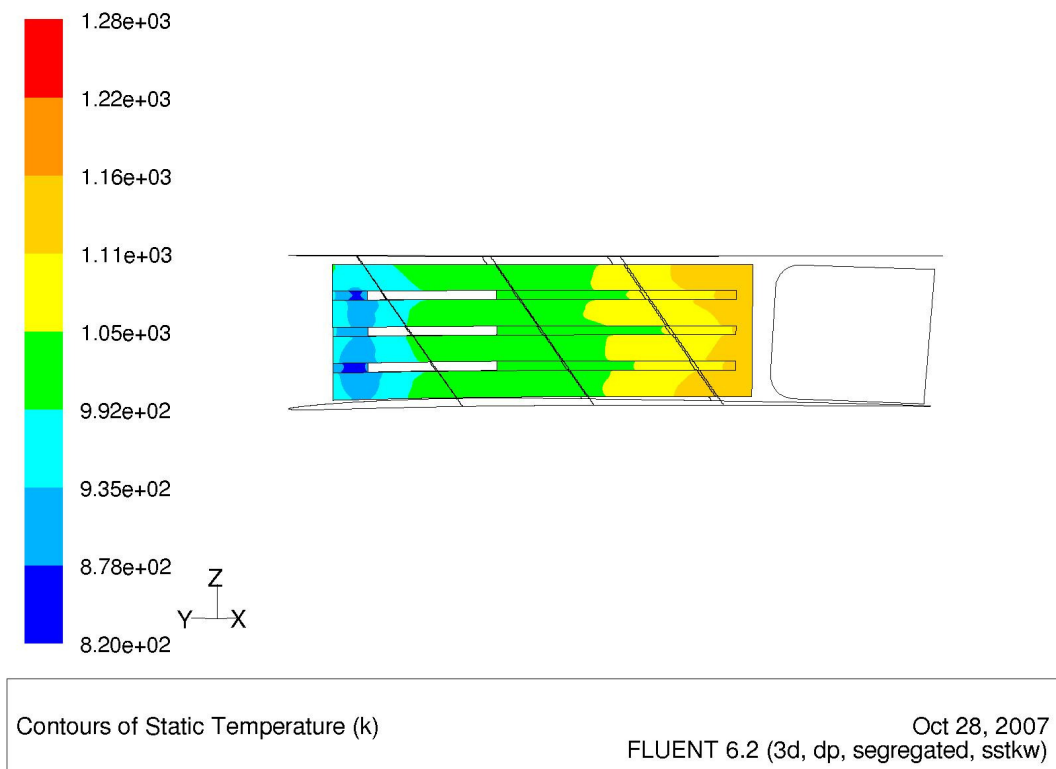
Fig. 4.18 Ttemperature distribution of internal pressure surface of section 2 – Case 4
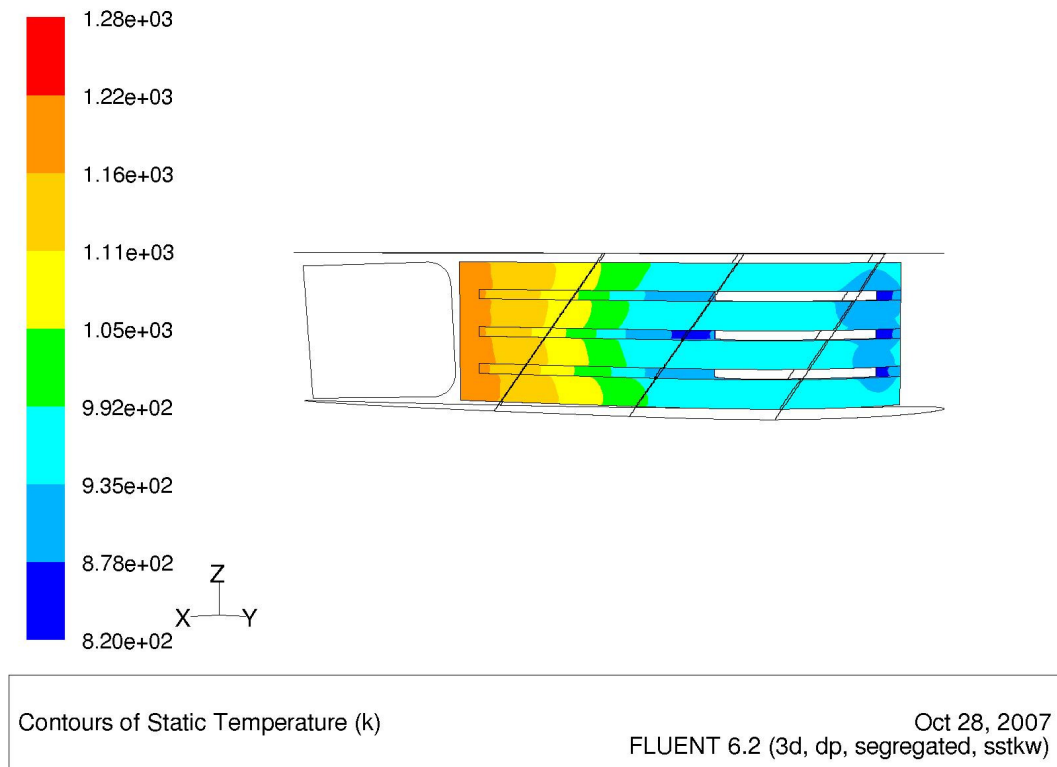
Fig. 4.19 Temperature distribution of internal suction surface of section 2 – Case 4

The results from this section show similar behaviour to those of the coarse section model of case 2. The grid resolution of this case is very fine. Solving for the boundary layer did predict better and more realistic results than wall function approaches. Although the present study did not specifically set out to prove accuracy with respect to grid resolution, it is known [36] that a wall function approach will not accurately predict turbulence and vortex formation, which could have influence heat transfer.

The problem at hand involved intricate flow passages, which means that it was not quite suitable to solve it with the wall function approach. The fine model predicted considerably cooler temperature profiles, as can be seen when comparing Figures 4.12 to 4.19. On the internal suction surface a cold spot, due to jet impingement, is observed in Figure 4.16. This cold spot was not picked up with the wall function approach and neither Figure 4.1 nor Figure 4.6 shows this phenomenon. A similar cold spot is observed on the suction surface of Figure 4.17. Although this cold spot was picked up by the wall function approach as in Figures 4.2 and 4.7, the shape and

size differ. The trailing-edge temperatures of this case were also colder by a magnitude of roughly 60 K.

It can clearly be seen that the grid resolution and turbulence model used had a huge influence on solving internal flow and conduction in NGV blades. Modern-day blades are far more complex than the T56 NGV and it will have an even greater influence on the results. A fine model had to be considered for this type of problem.

4.1.5   Case study 5 – Fine section with profiled hub/casing

This case study was the final model to be considered. This case is similar to the fourth one using a low Reynolds number approach and solving all the way to the wall and resolving the boundary layer. It has been seen from case study 3 that the temperature profile at the radial boundaries had a huge impact on conduction along the radial direction of the blade.
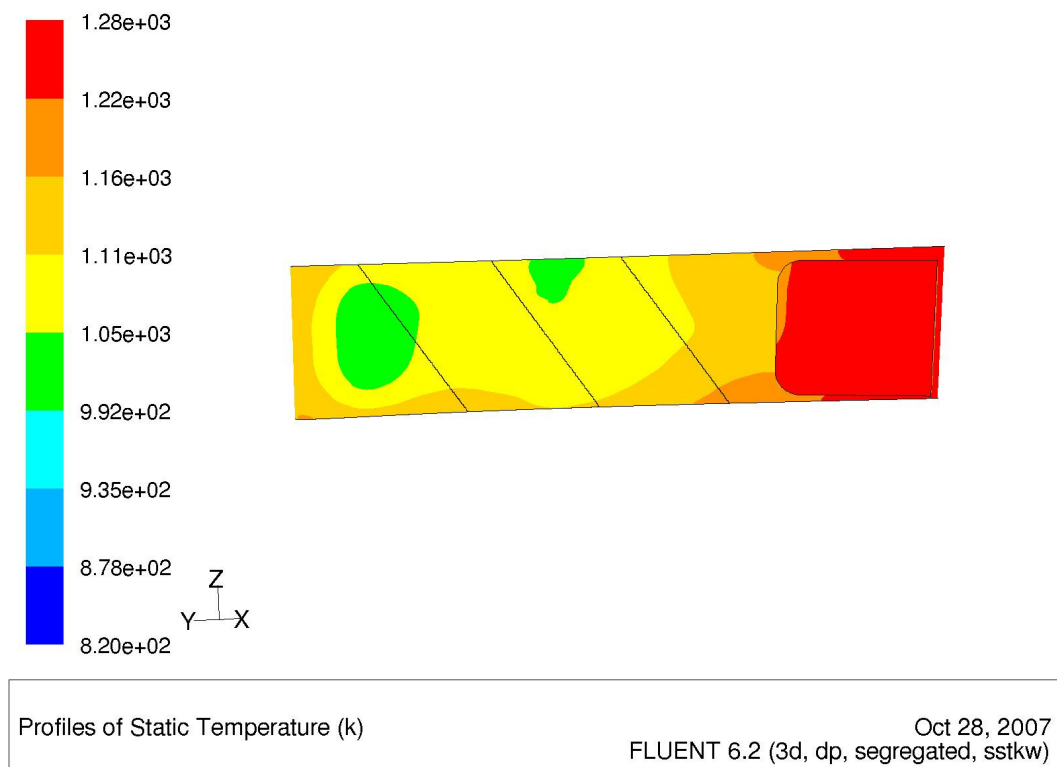
Fig. 4.20 Temperature distribution of external pressure surface of section 2 – Case 5
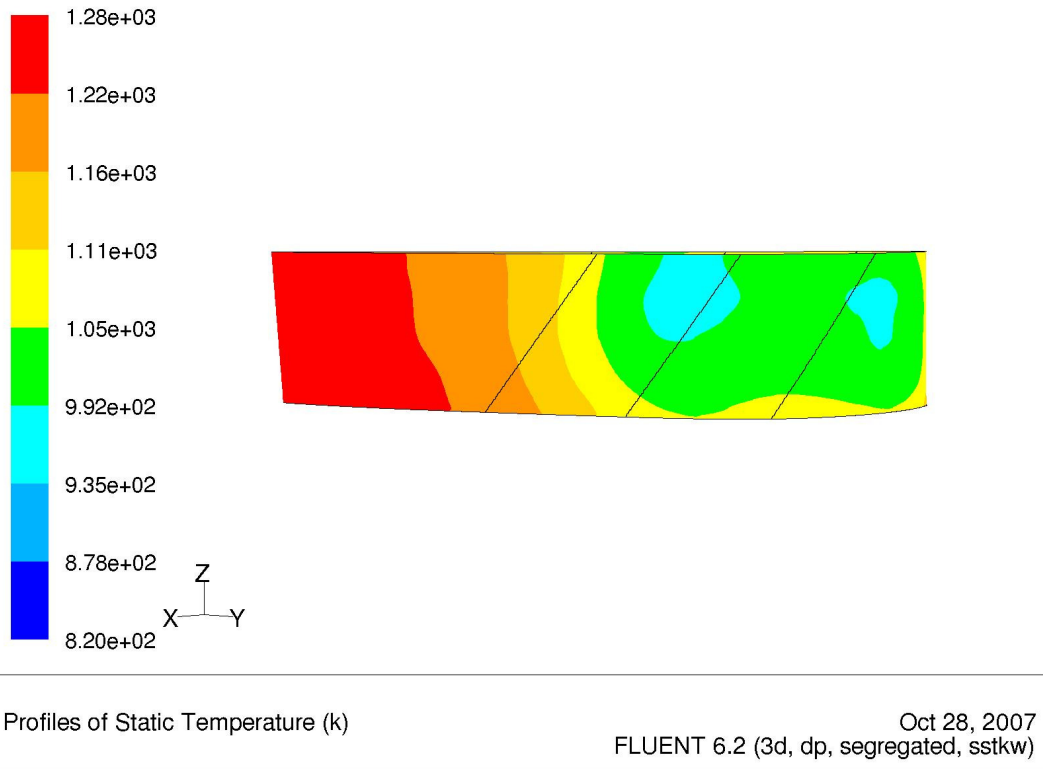
Fig. 4.21 Temperature distribution of external suction surface of section 2 – Case 5
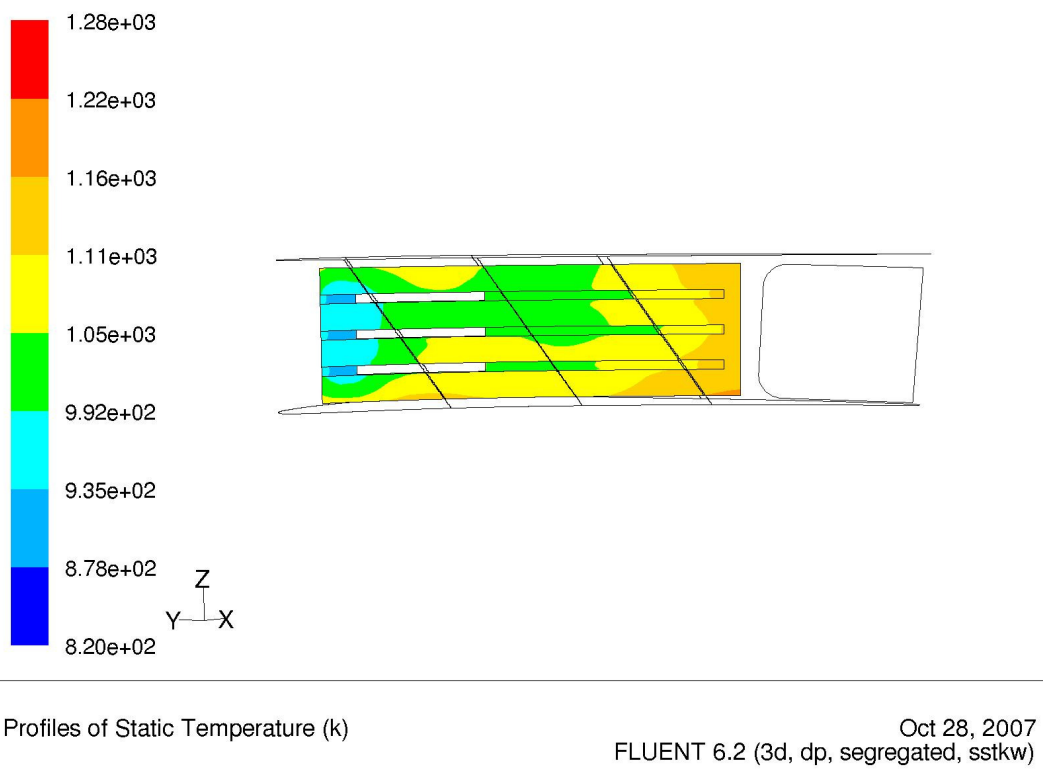
Fig. 4.22 Temperature distribution of internal pressure surface of section 2 – Case 5

|	
1.28e+03	
1.22e+03	
1.16e+03	
1.11e+03	
1.05e+03	
9.92e+02	
9.35e+02	
8.78e+02	
8.20e+02	

Profiles of Static Temperature (k)

Oct 28, 2007
FLUENT 6.2 (3d, dp, segregated, sstkw)
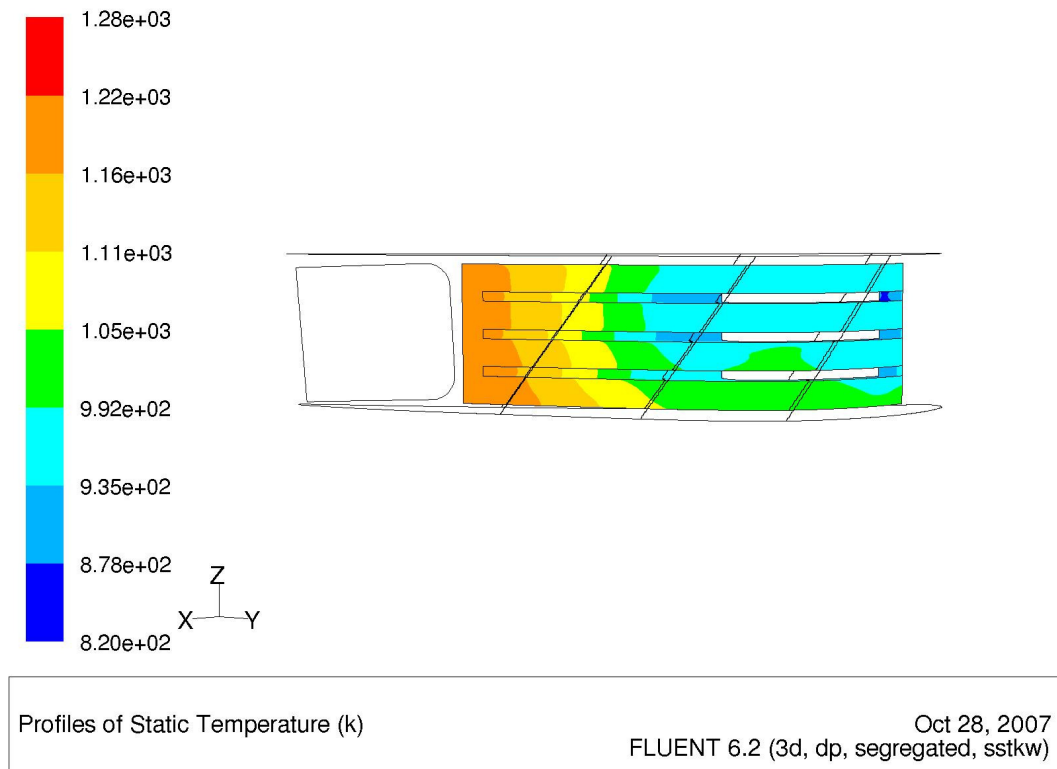
Fig. 4.23 Temperature distribution of internal suction surface of section 2 – Case 5

A definite cold spot can be observed on the internal pressure surface at the impingement zone in Figure 4.22. This cold spot conducts through the wall and is also observed on the external pressure surface of Figure 4.20. There is a general cold region on the internal suction surface at the middle to leading edge of Figure 4.23. The fine sectional model, without temperature profiled boundary conditions at the radial boundaries, yielded definite cold spots on both suction and pressure surfaces as is seen in Figures 4.16 to 4.19. Model 5 seemed to smooth out these cold regions to the extent where no definite spot was identifiable any more, as seen in Figure 4.23. This smoothing effect can be attributed to the presence of the thermal hub and casing boundary condition causing a thermal gradient across the radial direction of the blade section. Without these profiled boundary conditions, the section was subjected to thermal gradients focused on the centre rather than across the blade. Figure 4.17 clearly shows this and the thermal gradients appear to be almost symmetrical at hub and casing. The thermal gradient shape of the suction surface is similar to those on the coarse model of case 3. However, the pressure surface is quite different. There is no cold spot at the impingent zone on the pressure surface for case 3, while the low Reynolds number variant of the k-ω model did capture this.

The low Reynolds number approach is once again confirmed to be far more accurate compared with the wall function approach of the k-ω model. There is a temperature difference of almost 100 K on the leading-edge pressure surface. It confirms that jet impingement cooling is not accurately modelled using a wall function approach.

4.2   TACT1 results

The resolution of the TACT1 results was very coarse. This can be attributed to the coarse mesh imposed. However, being an empirical solver, the accuracy of results are not all that dependent on grid sensitivity.
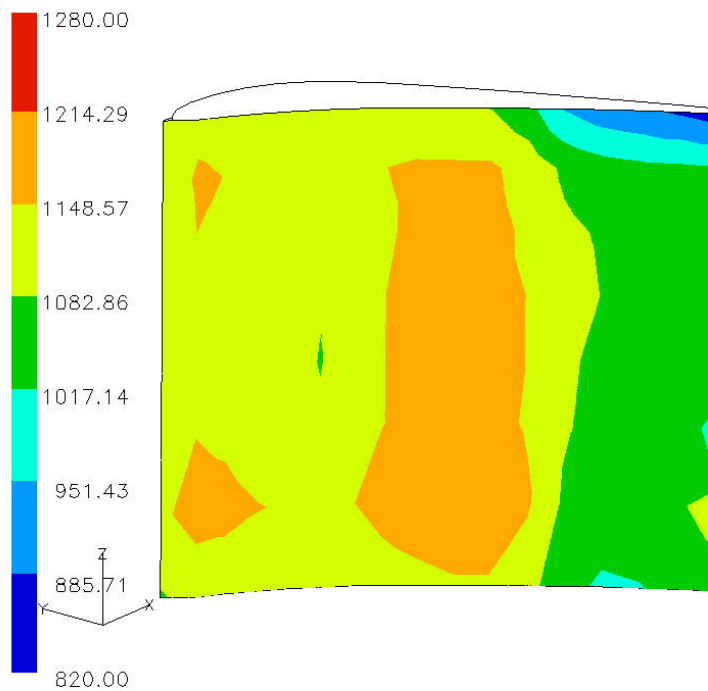
Fig. 4.24 External pressure surface wall temperature
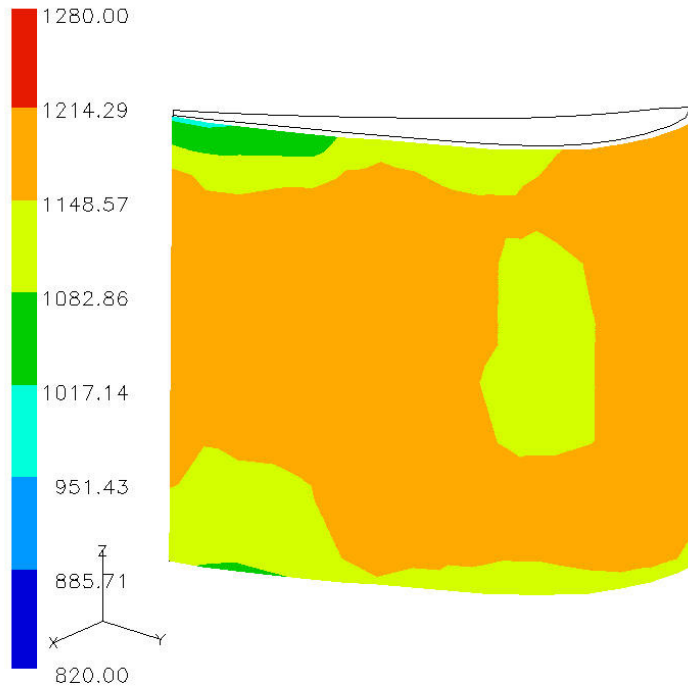
Fig. 4.25 External suction surface wall temperature
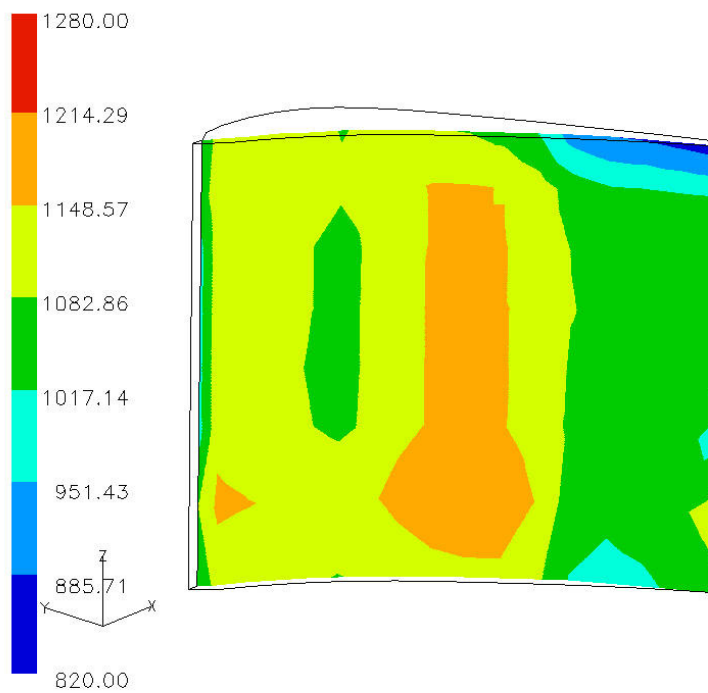
Fig. 4.26 Internal pressure surface wall temperature
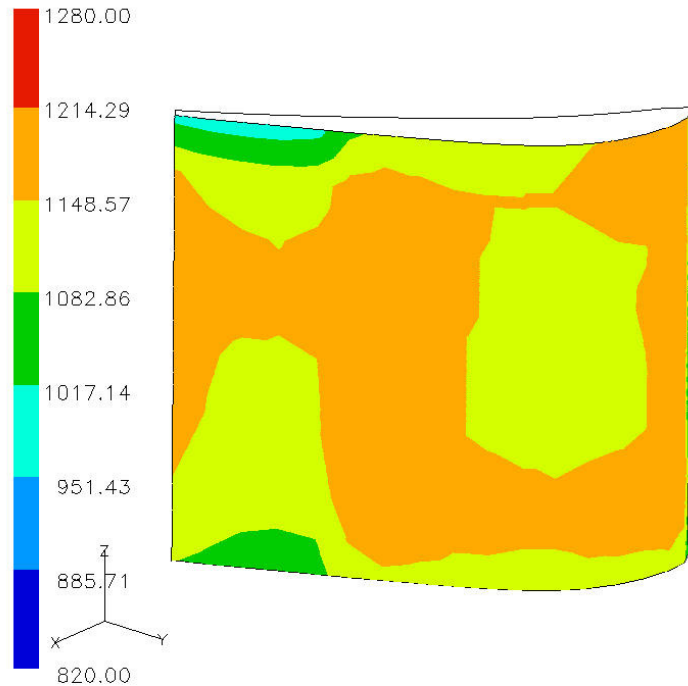
Fig. 4.27 Internal suction surface wall temperature

It is immediately noted that the temperature range of the TACT1 model in general is a great deal colder on the external and internal surfaces when compared with FLUENT results. Variation and temperature difference were discussed in section 4.3. The thermal gradients and temperature contours were analysed, compared and discussed in this section.

There is a definite cold spot on the suction surface that can be seen on both the internal and external suction surfaces. This pattern does correspond to the FLUENT results although the range differs. In Figures 4.24 and 4.27 this spot is observed. It stretches almost the entire radial length of the blade with a temperature of roughly between 1 028 K and 1 148 K. The cold section of the domain model has a temperature ranging between 935 and 993 K.

It is evident that the results of FLUENT were going to differ widely from TACT1 due to the following reasons: TACT1 had impingement on the leading edge where FLUENT had impingement on the pressure surface itself. The dump hole in the FLUENT analysis acted as an impingement hole where it was not modelled in this

way by TACT1. TACT1 did not model cross flow effects in the radial direction as can clearly be seen in Figure 4.11.

4.3   Comparative study

A further comparative study was done in order to better quantify differences and examine the temperature profiles at selected slices. Apart from a visual comparison done with the aid of temperature contour plots on the suction and pressure surface of the T56 blade, 2D plots were made comparing data at selected slices through the blade. Seven slices were considered for comparative purposes. Six slices passed through the jet impingement holes facing the leading edge and a seventh slice passed through the dump hole located in the last section as seen from the hub. The first and last sections, being sections 1 and 4, contained only one slice each. Each of the other two sections contained two slices. The fourth section also contained a slice through the dump hole.

The data represented in the Figures 4.28 to 4.31 is that of section 2. Data for the other three sections is represented in Appendix D. Due to the fact that fine models were constructed for only this section the data in Appendix C is representative of only the FLUENT domain model (case 1) and the TACT1 model.
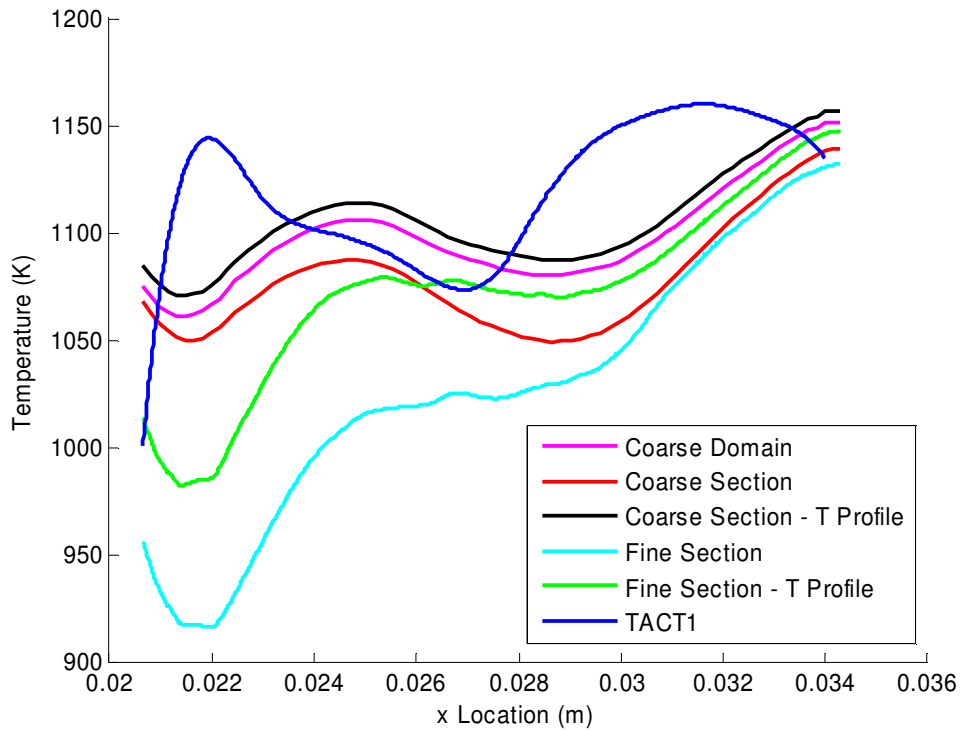
Fig. 4.28 Metal temperature on internal pressure surface at radial distance of
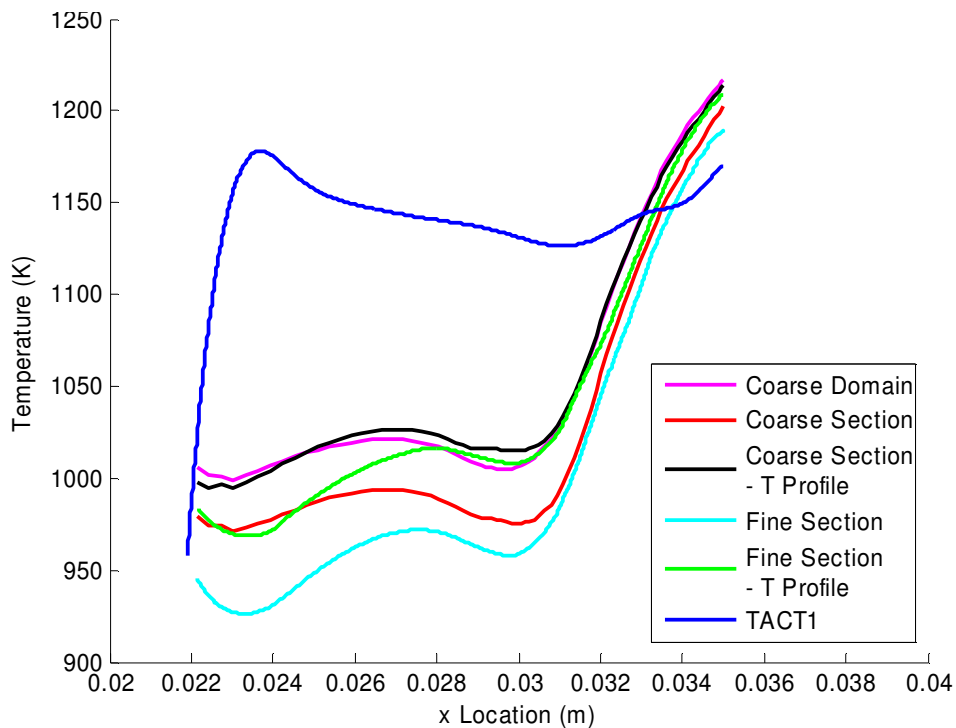
0.2095 m

Fig. 4.29 Metal temperature on internal suction surface at radial distance of

0.2095 m
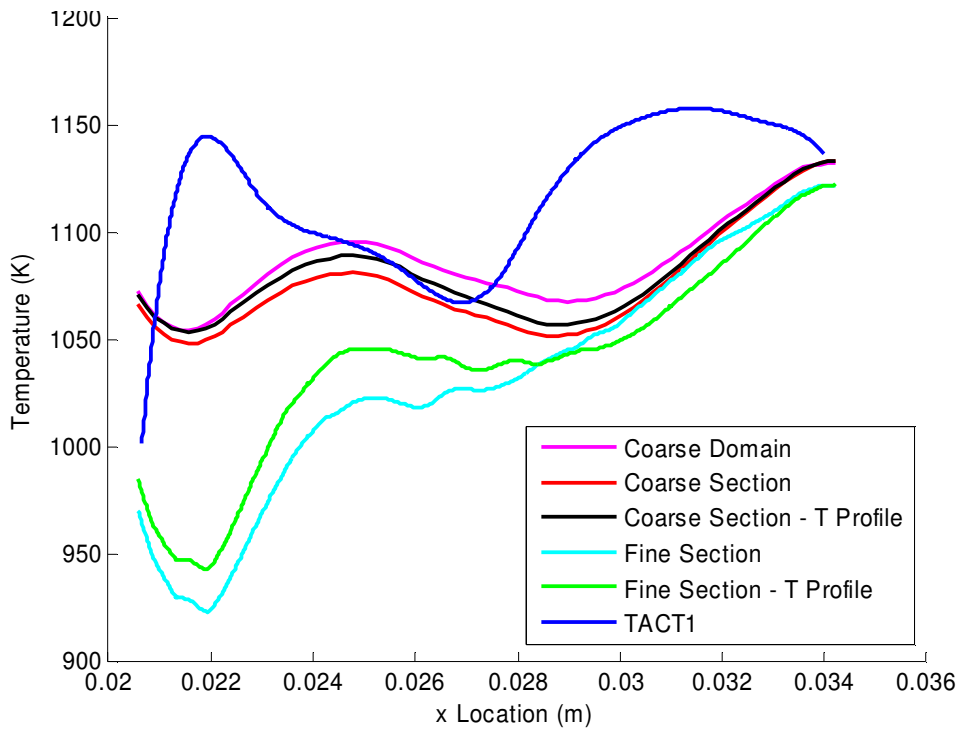
Fig. 4.30 Metal temperature on internal pressure surface at radial distance of
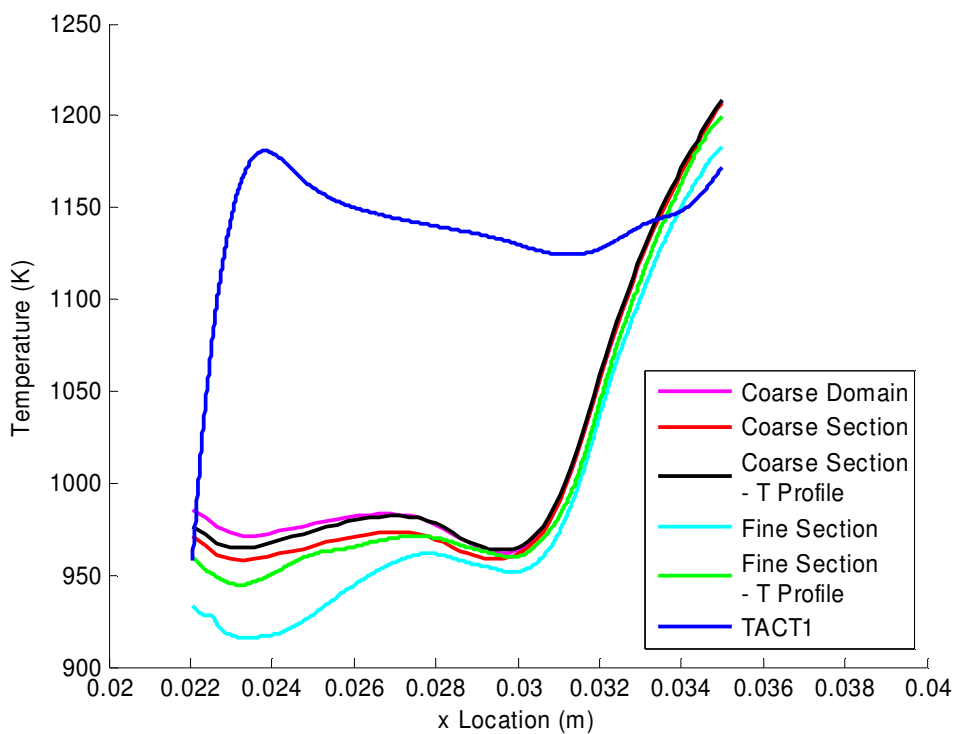
0.2126 m

Fig. 4.31 Metal temperature on internal suction surface at radial distance of

0.2126 m

TACT1 results were vastly different from the FLUENT results. This variation can be seen in Figures 4.28 to 4.31.

FLUENT results on the pressure surface varied considerably between the wall function approach and the low Reynolds number model where the boundary layer was resolved when comparing these two methods as seen in Figure 4.28 and 4.30. The suction surface shows more similarity in Figures 4.29 and 4.31. The two fine models with and without the temperature-profiled separator rib boundaries, predicted temperatures a great deal cooler than the wall function approach at the impingement region. This establishes that, with or without temperature effects being modelled from neighbouring sections, impingement was modelled to be far colder than with a wall function approach. As expected, the case where the temperature profile was present, as depicted in Figure 4.10, yielded slightly hotter temperatures at the leading-edge region but similar temperatures at the trailing edge. Impingement is a complex flow phenomenon and using a wall function approach will not yield accurate results.

TACT1 had an impingement jet that impinged at the furthermost leading-edge concave surface. This is evident from the plots above, where the coldest temperature is at the very start of the TACT1 curves. This is naturally the region where the most cooling took place and thus it is the area with the coldest temperatures. The geometric model constructed in Gambit represents a model where impingement is on the pressure surface and not at the same location as TACT1. TACT1 cannot be modified to account for different impingement angles. The lowest temperature for the FLUENT model is also found at its impingement zone. This zone can be identified in Figures 4.28 to 4.31. There is a sudden dip as one follows the plots from the leading edge to the trailing edge. This dip is where impingement took place for the FLUENT models.

Although there is a slight tendency towards similar trends, the TACT1 plot does not compare well with the FLUENT results. This is not a surprise and vast variation is to be expected. The fine model with temperature profiled hub and casing best fits the TACT1 data. This is due to the fact that impingement was better modelled with fine grid resolution. The TACT1 data was shifted so that the impingement location corresponded to the FLUENT model shown in Figure 4.32.

The following discussion is with reference to the adjusted Figure 4.32. The impingement temperature was almost identical and compared well with case 5 and the TACT1 results. It is also noted that the fine model without the imposed temperature profile did not compare well in the impingement zone and predicted far colder temperatures. This radial temperature gradient thus had a huge influence on impingement. Both models had a sudden temperature increase after the impingement zone, however TACT1 had a very sharp rise in temperature where FLUENT did not show this behaviour and increased at a more gradual slope. Temperatures decreased as the air flowed towards the trailing edge. The gradient of this curve changed once again and temperatures increased as the blade walls became thinner. The change in gradient is at the same location for both models. TACT1 did not model the trailing edge ejection slots as FLUENT does. This is a shortcoming of TACT1. TACT1 models ejection as a slot running the width of the blade in the radial direction. At various locations where there should not be slot ejection, the width of the slot is appropriately adjusted to allow for a simulated slot ejection at the relevant location where there are slots on the Gambit geometry. The trailing-edge section from a location of 0.034 m was discarded and not used for comparative purposes as the air leaves the FLUENT model at this location.
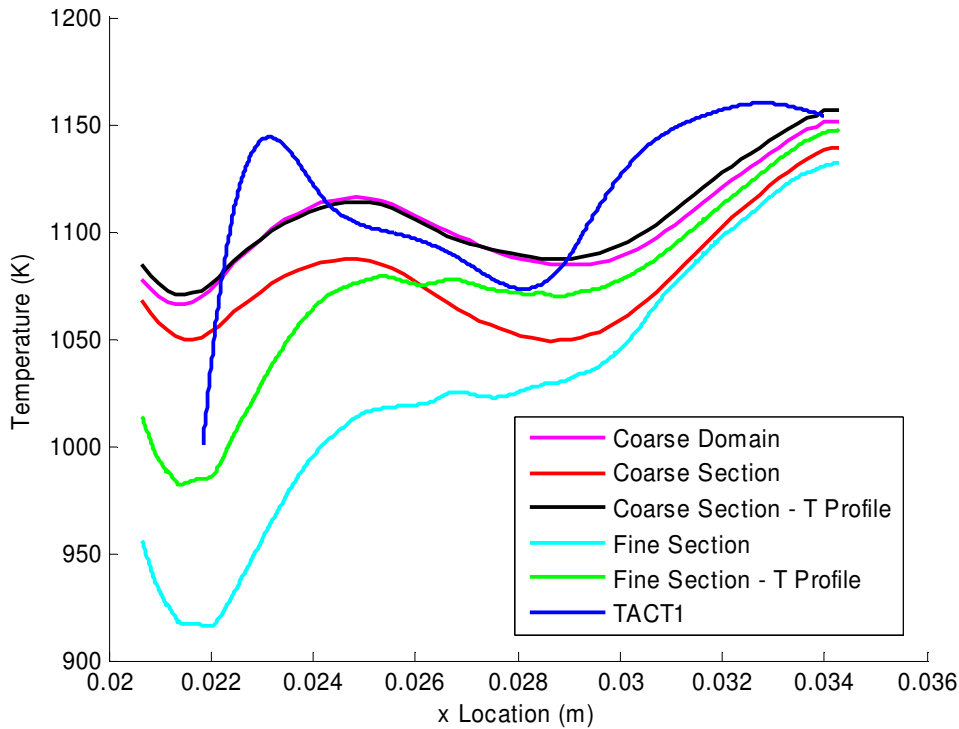
Fig. 4.32 Shifted figure of metal temperature on internal pressure surface at radial distance of 0.2095 m

A further comparative study was performed using the value of cooling effectiveness. This value is defined as follows:

Cooling Effectiveness   …(4.1)

$$\eta_{cooling} = \frac{T_{gas} - T_{blade}}{T_{gas} - T_{coolant\,inlet}}$$

Cooling effectiveness is a direct function of the relation between the mean combustor gas temperature, the external blade temperature and the coolant inlet temperature. However, the blade temperature is the only variable and thus cooling effectiveness directly relates to this value. The mean temperature of the combustor gas profile is used as the value for T_{gass}. This value is 1 350 K. $T_{coolant\,inlet}$ is 601.15 K as stated earlier. The temperature for T_{blade} is that of the external metal temperature at various locations along the chord-wise direction of the blade slice. Again, section 2 is used for this comparison. Figures 4.33 and 4.34 represent the data for cooling effectiveness.
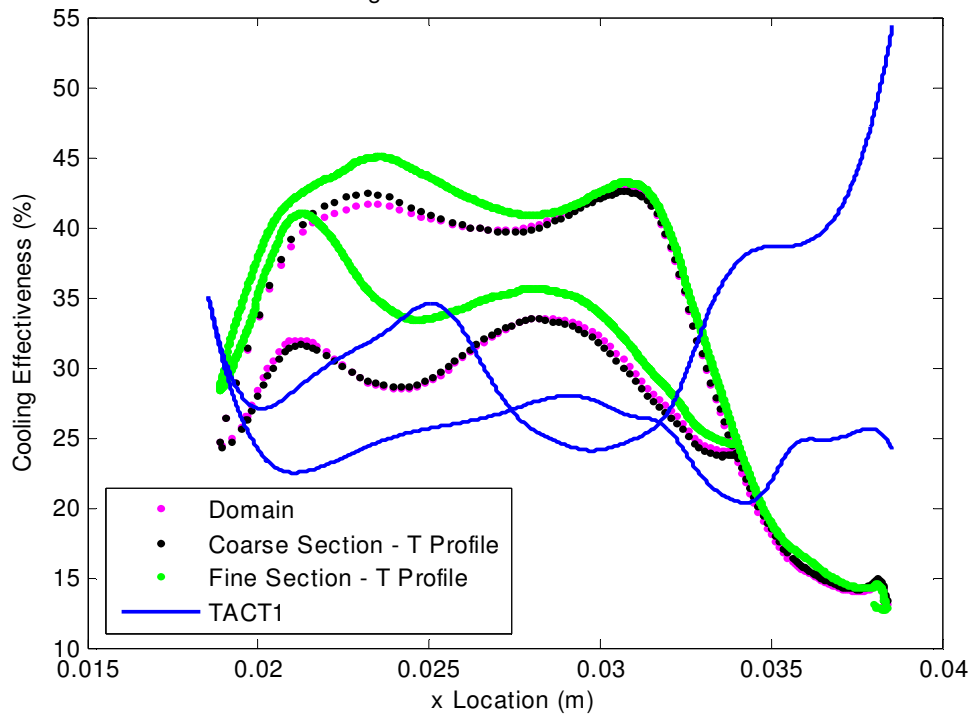
Fig. 4.33 Cooling effectiveness at radial distance of 0.2095 m
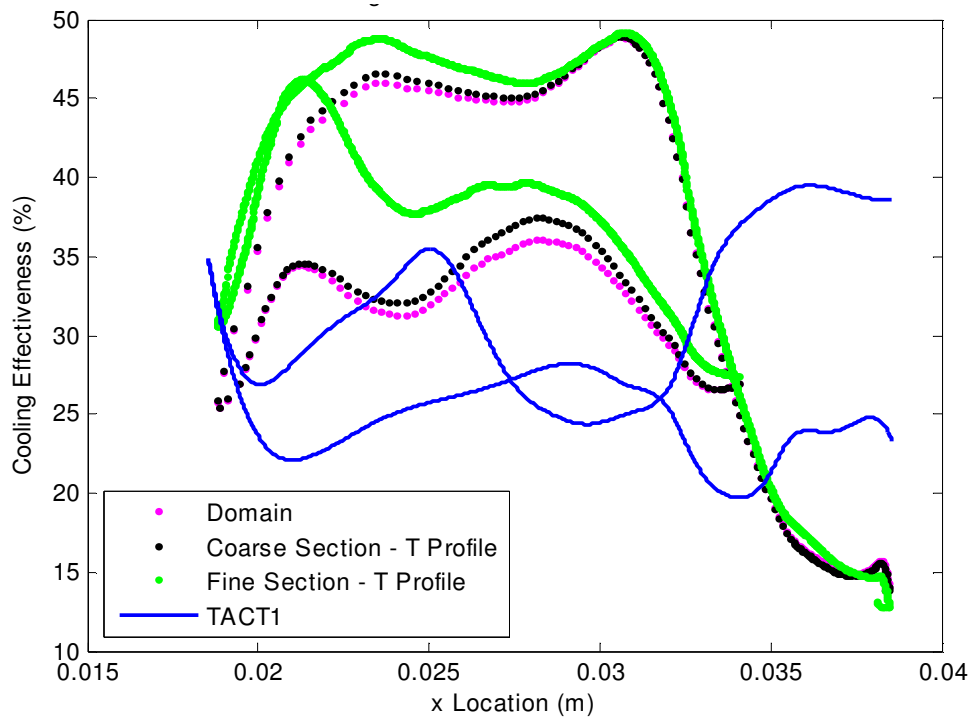
Fig. 4.34 Cooling effectiveness at radial distance of 0.2126 m

The shape of the plots in Figures 4.33 and 4.34 did not correspond well between FLUENT and TACT1. The values of cooling effectiveness also had a large variance

CHAPTER 5

CONCLUSION AND RECOMMENDATIONS

SUMMERY OF CONTENTS

SUMMARY

CONCLUSION

RECOMMENDATIONS

5.1 Summary

It is imperative take into account that TACT1 is a computer code that dates back to the early 1980s. It is an empirical solver that uses basic correlations for flow in channels and jet impingement. FLUENT, on the other hand, is a RANS solver that uses complex numerical schemes for solving for the flow, using the Navier-Stokes equations and applying them to the flow field.

The question posed is not which model is the best but what are the strengths and weaknesses of each model. Before numerical solving capabilities were available to the academic community, let alone industry, empirical correlations were the only method known for solving flow and conduction problems. The introduction of numerical methods vastly changed the field of thermoflow. To date this is a field where advancement is made daily, particularly in the field of turbo-machinery.

The Allison T56 Engine is a fairly old one that dates back four decades. Chapter 2 provided more details of the T56 engine history and development. Although not confirmed, the T56 NGV blades were probably designed using the design codes and/or philosophies of NREC, STAN5, LOSS3D and TACT1. Intensive numerical modelling was still in its infancy and would definitely not have been used for design purposes of this blade. NREC is thus an ideal tool to use for analysing this blade along with the STAN5, LOSS3D and TACT1 codes. Although widely used at this time, a comparative study has not yet been done between a RANS solver and an empirical code.

It was the purpose of this study to do such an analysis and report on the applicability of each of these two codes with respect to the relevant problem at hand. Due to the age of the T56 engine, these planes will not be flown indefinitely and the SAAF will be replacing them with a similar type of transport aircraft such as the Military Airbus A400M in the near future. Modern-day aircraft employ complex cooling technologies and countries are often restricted to the amount allocated for servicing these engines themselves. The TACT1 code would not be used for any analysis on these types of engines and analyses are often done using off-the-shelf RANS solvers. This points to a time when CFD codes will replace the age old empirical codes for coolant flow

modelling. It was not the purpose of this study to discuss and model a particular NGV blade but to do a back-to-back comparison with an existing blade that could be modelled with TACT1. The aim was not to seek a result that portrays reality and accuracy in the modelling but truth with respect to the methods employed.

5.2 Conclusion

The geometry obtained for modelling the NGV in FLUENT was kept as close to the original as possible. TACT1 could not use this complex geometry and vast assumptions were made with respect to impingement location and the extrusion of the blade. This blade extrudes in the radial direction with a twist and a draught angle. This was not modelled in TACT1 and the geometry was extruded with a straight radial direction. It was not the purpose to draw out the mismatches between RANS solvers and empirical solvers but to discuss the applicability of each.

As discussed in Chapter 5, the sectional model with temperature-profiled boundaries yielded the most favourable results. The following conclusions are drawn from this:

➢ TACT1 does treat conduction in the blade material as a 3D problem and conducts through the blade from the hot gas to the interior coolant. It also conducts in the radial direction. Conduction in the radial direction plays a huge role in the temperature profiles formed on blade surfaces.

➢ Impingement cannot be successfully modelled with a wall function approach and such an approach under predicts cooling. For an accurate FLUENT model the grid resolution has to be very fine to facilitate the use of a low Reynolds number approach to better model impingement.

➢ TACT1 yielded good conduction but poor flow solution with no radial flow taken into account. No secondary flow such as vortex formation or breakaway could be modelled. This is not necessarily a downfall as general temperature fields were predicted to an acceptable level from where areas of interest could be identified such as cold spots and steep gradients.

➢ TACT1 could not model the presence of ribs and this leaded to an under prediction of cooling effectiveness. Again this is not a complete drawback as

an under prediction is far more acceptable than an over-prediction. However, the drive to increase combustor temperatures will always facilitate a drive for cooler blades where even the smallest error elimination is welcomed.

➤ The sectional fine model of case 5 is the favoured model when using a RANS solver.

5.3   Recommendations

➤ Because of the inconsistency in geometry between the Gambit and TACT1 models, it is recommended that a further study be done where the Gambit geometry is adjusted such that it closely resembles the TACT1 geometry with impingement on the concave inner surface at the tip of the leading edge. The dump hole will also have to be adjusted so as not to impinge. This study will yield an insight into what errors are made between an accurate geometry and an assumed geometry and the effect it has on the final solution pertaining to temperature profiles.

➤ It is recommended that the RANS solver FLUENT is coupled with a finite element package such as Abaqus or MSC Patran in order to solve for the thermal stress induced. From this, one would be able to do a basic thermal fatigue analysis. A later study would also include a transient problem setup where thermal stress is updated in a transient environment after each iterative step. Depending on the computer power available, this problem would most likely have to be run on the entire domain with a wall function approach.

➤ If a further analysis were to be done using an empirical code it should be one relating to a more modern engine where empirical data could also be obtained using a basic experimental setup.

between these methods of solving. The TACT1 cooling effectiveness was a great deal lower than that of FLUENT. This is attributed to the fact that in general FLUENT temperatures are colder, causing a higher cooling effectiveness. Impingement for TACT1 when referring to Figure 4.33 yielded a cooling effectiveness of 35% compared with a 41% for the FLUENT case 5 fine model at a radial location of 0.095. However, when looking at the next slice downstream at a radial location of 0.2126 in Figure 4.33, FLUENT case study 5 showed a cooling effectiveness at impingement of 46% where the TACT1 slice again showed an effectiveness of 35%.

The coarse section with the imposed temperature profile showed good correlation with the domain model. This is due to the fact that the same turbulence model with wall function approach was used and again confirms that imposing a temperature profile at the radial boundaries yielded far more accurate results than the exclusion of them. These wall function approach models showed similar effectiveness at impingement of roughly 35%.

The suction surface of TACT1 showed better cooling effectiveness than the pressure surface. This is an indication that the suction surface was better cooled than the pressure surface and more flow had to pass on the suction surface between the plenum and blade wall than on the pressure surface-side. This is also true for the FLUENT models where the suction surface experienced better cooling effectiveness than the pressure surface. The suction surface also correlated better between the sectional and domain models. The colder suction surface had already been established from Figure 4.5. A vortex formed at the leading edge, due to impingement, forced more air towards the suction surface. This, however, is not necessarily the case for TACT1, as impingement was at the leading edge tip and a correlation was used for impingement.

The trailing edge of TACT1 showed a false increase for effectiveness that was not real. This was discarded and not used for any comparisons.

4.4   Conclusion

Various modelling variations were tried relating to both turbulence model used as well as only solving for a quarter section of the blade. These sectional models were further varied with respect to the application of a temperature profile to the hub and casing side of the section.

Computational cost was an important aspect for determining which model was preferred. Turbine manufacturing companies and research institutions still widely use in-house-developed codes for solving for heat transfer and flow.   FLUENT simulations can take a very long time to reach convergence, depending on the size of the model. Even when a wall function approach is used, convergence could still take in the order of a couple of hours depending on the computer resources available. The domain model and the coarse sectional models discussed in Chapter 4 were run on a Pentium IV 3.2 GHz with hyper-threading, using 2GB of RAM. These simulations typically converged in a couple of hours where the sectional fine models took roughly 68 hours to converge using a four-PC cluster. Each machine had 2GB RAM with clock speeds ranging from 2.8 GHz to 3.2 GHz. The cluster had a combined RAM capacity of 8GB.   In contrast, TACT1 results were obtained after roughly 400 iterations, taking no longer than five minutes. This gives a good indication of the computational expense difference between these two codes.

When considering computational cost as well as accuracy with respect to obtaining realistic results the sectional model using the low Reynolds number k-ω turbulence modelling approach seemed to perform best for this particular application. This can clearly be seen in Figure 4.32 where the course models fell short in comparison with TACT1 results.

first section is the limited flow in this region. The flow of air had to take quite a sharp corner at the trailing edge before it exited at the trailing edge exit port. This slowed down the flow and caused convective cooling to decrease. This first section was also furnished with only one impingement hole allowing for a mass flow through this section of almost half of that going through any of the other sections.

The path line plot in Figure 4.11 shows this sudden change in flow direction at the trailing edge. It also shows that a great deal of flow actually left section 1 after impingement and joined the flow of the second section. This leaded to an even greater loss of cooling capacity. The black line that can be seen in Figure 4.11 indicates the position of the solid metal of separator rib 1. The middle sections, being sections 2 and 3 have minimal coolant spreading to adjacent sections, while section 4 with the dump hole again shows a considerable leakage to its adjacent section, being section 3. In this region, the leakage did not have a great effect on the coolant capacity, due to the dump hole supplying more air to this section than to any of the other sections.

It is difficult to specify or predict the amount of flow and direction in the leading edge region, due to complex impingement-related turbulence and flow being present. Impinging jets in general collide with each other, causing flow to diverge away from each adjacent jet in a symmetrical fashion. This leads to the symmetry boundary condition as described in Chapter 3.

2.00e+02	
1.75e+02	
1.50e+02	
1.25e+02	
1.00e+02	
7.50e+01	
5.00e+01	
2.50e+01	**Black Line Indicating Separator Rib Location**
0.00e+00	

Path Lines Colored by Velocity Magnitude (m/s)   Oct 08, 2007
                                              FLUENT 6.2 (3d, dp, segregated, sstkw)
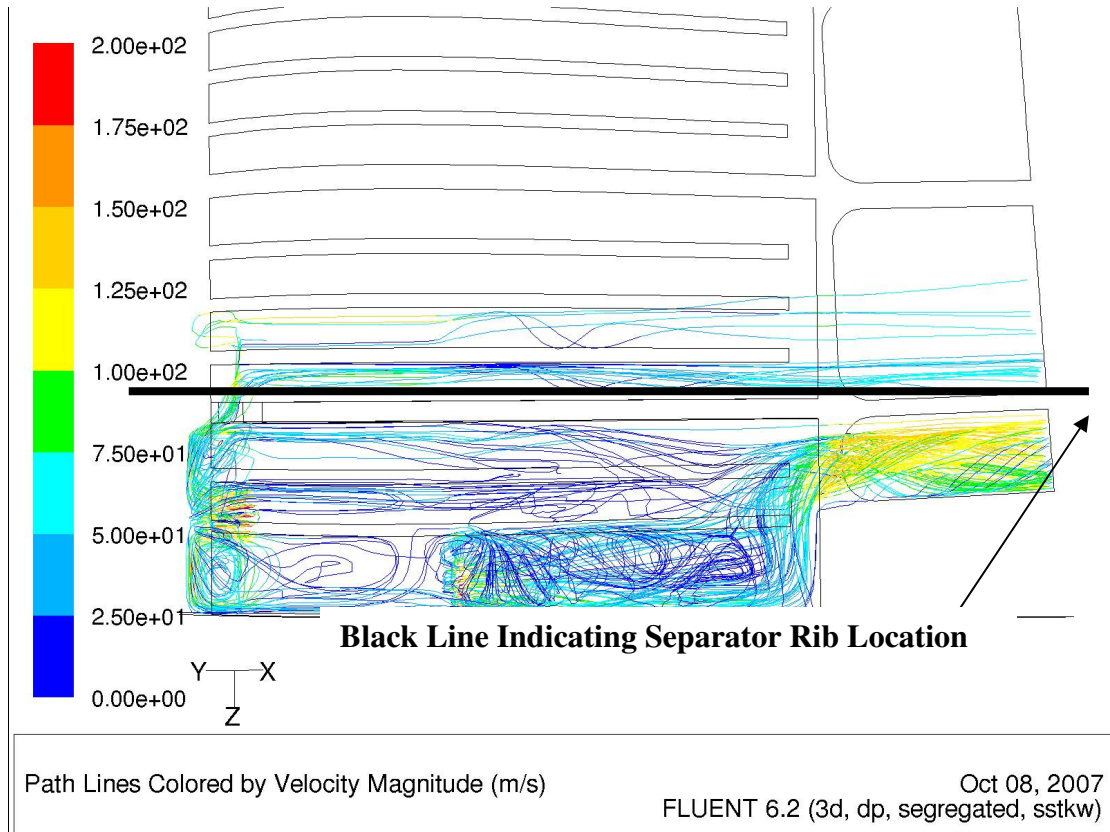
Fig. 4.11 Path lines coloured by velocity magnitude for the coarse domain model

1.28e+03
1.22e+03
1.17e+03
1.11e+03
1.05e+03
9.93e+02
9.35e+02
8.78e+02
8.20e+02

Contours of Static Temperature (k)   Oct 08, 2007
                                              FLUENT 6.2 (3d, dp, segregated, sstkw)
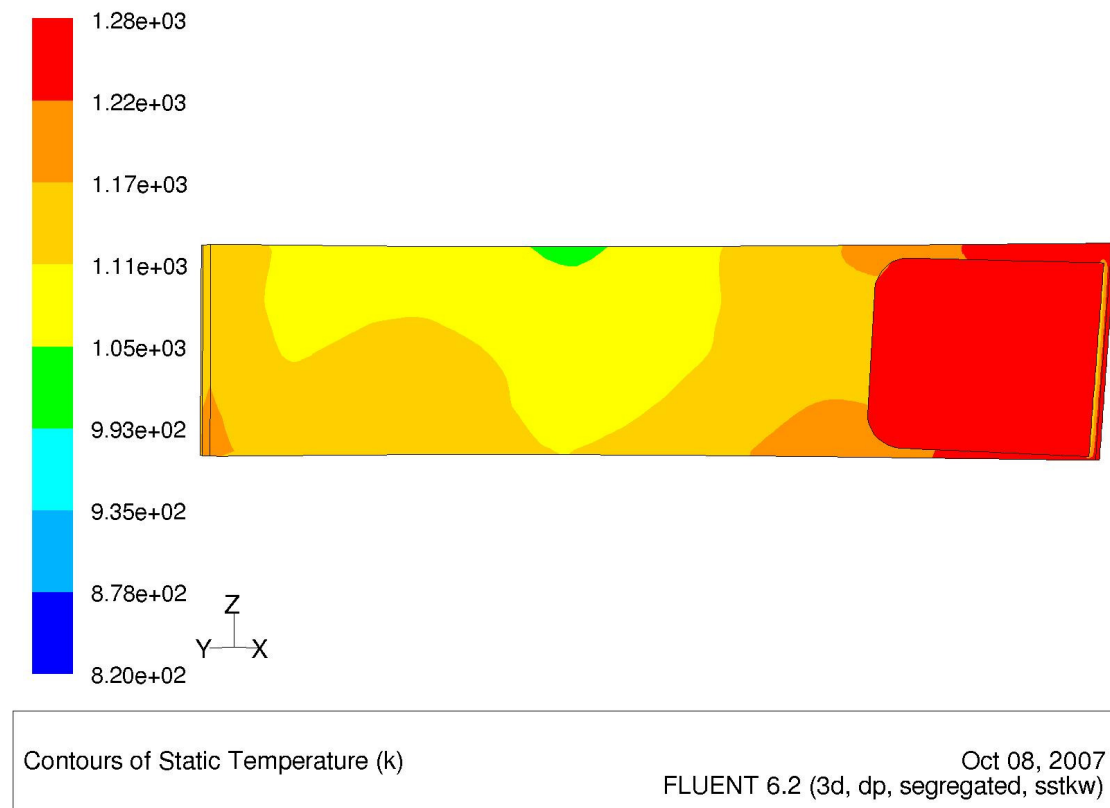
Fig. 4.12 Temperature distribution of external pressure surface of section 2 – Case 3
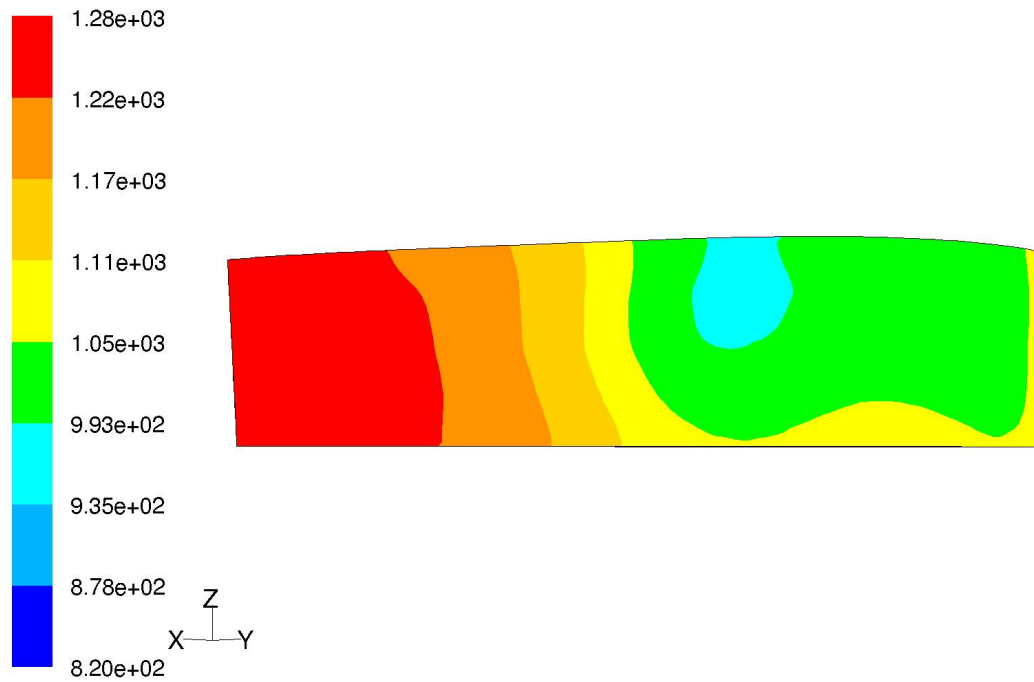
Contours of Static Temperature (k)   Oct 08, 2007
                                                    FLUENT 6.2 (3d, dp, segregated, sstkw)

Fig. 4.13 Temperature distribution of external suction surface of section 2 – Case 3
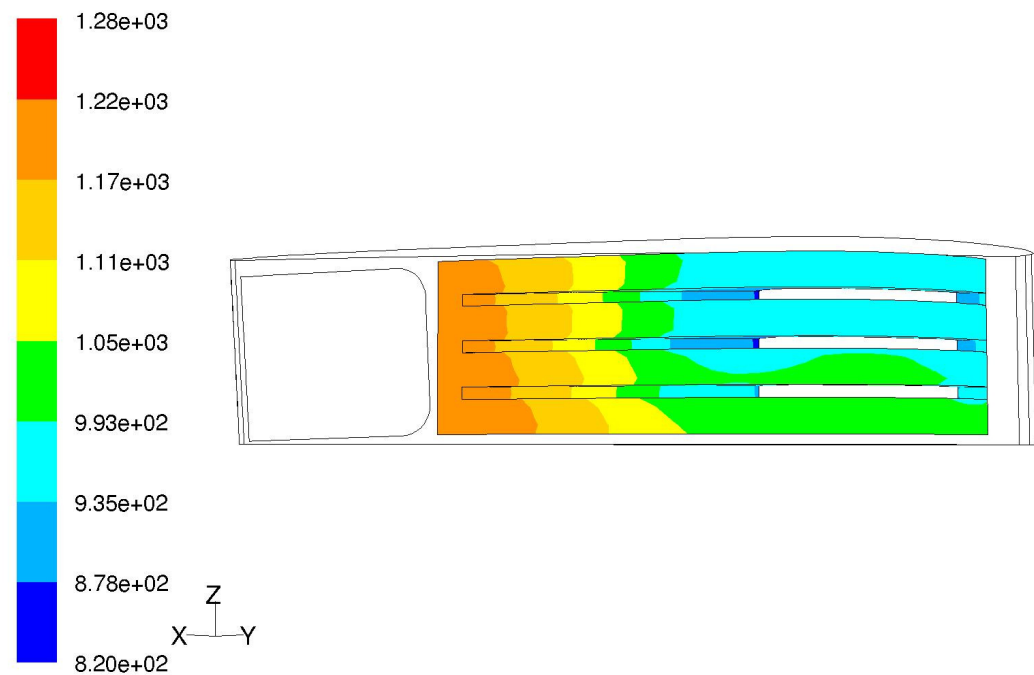
Contours of Static Temperature (k)   Oct 08, 2007
                                                    FLUENT 6.2 (3d, dp, segregated, sstkw)

Fig. 4.14 Temperature distribution of internal suction surface of section 2 – Case 3
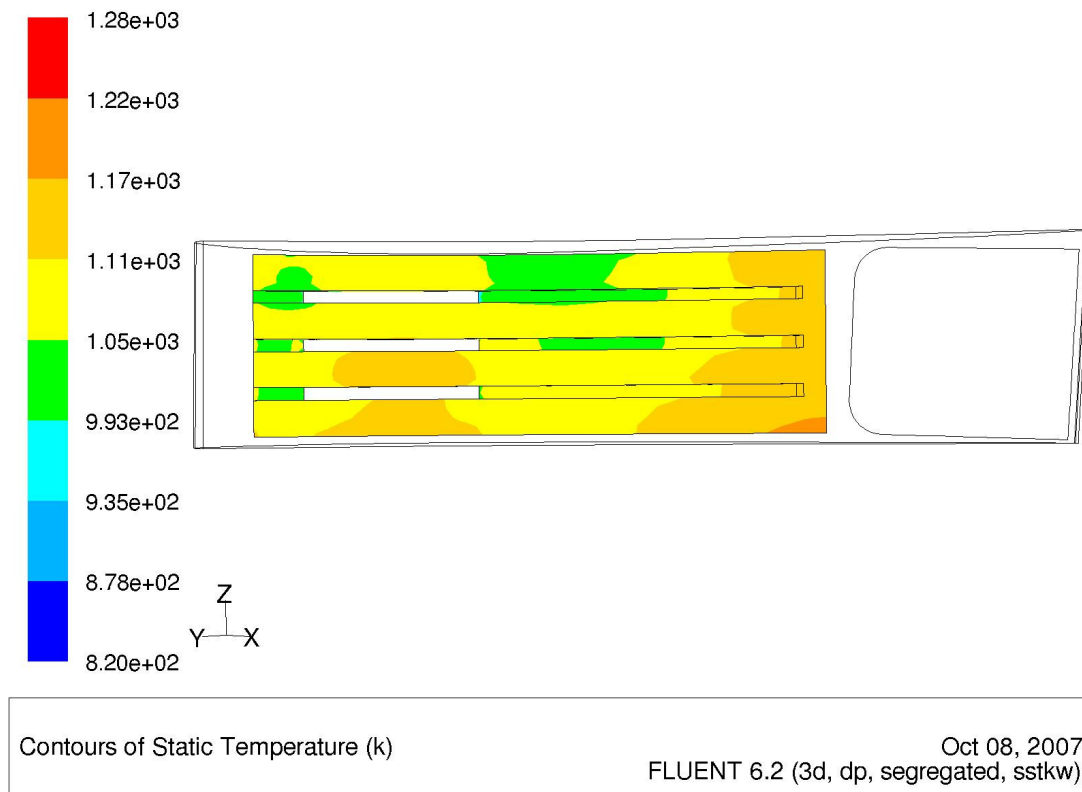
Fig. 4.15 Temperature distribution of internal pressure surface of section 2 – Case 3

Results for this case study are favourable when compared with the domain model of case 1. These two models yielded results of similar magnitude. Figures 4.1 to 4.4 were compared with Figures 4.12 to 4.15. The contour patterns as well as the order of magnitude of temperatures on the suction and pressure surfaces corresponded well with each other. Figure 4.13 reveals the presence of a colder region in the interior of the blade halfway between the trailing and leading edge. Figure 4.2 has a similar cold spot on the suction surface. The pressure surface of case 1 as is seen in Figure 4.1 seems to match that of Figure 4.12. Figures 4.3 and 4.4 are compared with Figures 4.14 and 4.15 and the internal ribbed surfaces also show remarkable similarity.

It is now established that for an accurate sectional model, a temperature profile has to be imposed as a boundary condition on the hub and casing. The effect that the hot first section had on the upstream sections is too great to ignore. In the domain model of case 1, a great deal of air leaked from the first section into the second section. This is not modelled in the sectional model causing less mass flow to be present compared with the same section of case 1.

REFERENCES

[1]   Cohen, H., Rogers, G.F.C., Saravanamuttoo, H.I.H., *Gas Turbine Theory*, Fifth Edition, Prentice Hall, 2001.

[2]   Rolls Royce, *T56 Power for the Hercules, Orion, Hawkeye and Greyhound,* T56 Fact Sheet, Rolls Royce Group plc TJ602, 2004

[3]   Mills, A. F., *Heat Transfer*, Second Edition, Prentice Hall, 1999.

[4]   United States Air Force, *C130 Hercules Fact sheet*, October 2005.

[5]   Allison Engine Company, *T56/501D Series III Training Manual, 15RC12*, 7610-18-019-3202, May 1996.

[6]   Allison Engine Company, *BT56/501 D Series III Training Manual 15RC12*.

[7]   Sontag, E. R., Borgnakke, C., Van Wylen, G.J., *Fundamentals of Thermodynamics*, Fifth Edition, John Wiley & Sons, 1998.

[8]   Rahman, F., *Numerical Modelling of Heat Transfer and Thermal Stresses in Gas Turbine Guide Vanes*, Master's Dissertation, November 2003.

[9]   Lippert, A. M., *Numerical Prediction of Internal Coolant Flow in Gas Turbine Blades*, Master's Dissertation, March 1994.

[10]   Rubensdorffer, F. G., *Numerical and Experimental Investigations of Design Parameters Defining Gas Turbine Nozzle Guide Vane Endwall Heat Transfer*, Doctoral Thesis, 2006.

[11]   Unger, D., Herzog, H., *Comparative Study on Energy R&D Performance: Gas Turbine Case Study*, Massachusetts Institute of Technology, Prepared for Central Research Institute of Electric Power Industry (CRIEPI), August 1998.

[12]   Sakowski, B., Darling, D., Roach, R. L., Van de Wall, A., *Evaluation and Application of the Baldwin-Lomax Turbulance Model in Two-Dimensional, Compressible Boundary Layers*, National Aeronautics and Space Administration, Lewis Research Centre, 1992.

[13]   Bardina, J. E., Huang, P.G., Coakley, T.J., *Turbulence Modelling, Validation, Testing and Development*, NASA Technical Memorandum 110446, 1997.

[14]   Edurado Oliveira de Suza, L. C., Dias de Moura, M., Brazil Junior, A. C. P., Nilsson, H., *Assessment of Turbulence Modelling for CFD Simulations into Hydroturbines: Spiral Casings*, Department of Mechanical Engineering, University of Brazil, Brazil, Department of Thermo and Fluid Dynamics, Chalmers University of Technology, Gőteborg, Sweden, 2003.

[15]   Martini, P., Schulz, A., Wittig, S., *Experimental and Numerical Investigation of Trailing Edge Film Cooling by Circular Coolant Wall Jets Ejected from a Slot with Internal Rib Arrays*, School and Institute for Flow and Thermal Machines, University Karlsruhe, Germany, GT2003-38157, Proceedings of the ASME Turbo Expo, June 2003.

[16]   Martini, P., Schulz, A., Bauer, H. J., Whitney, C. F., *Detached Eddy Simulation of Film Cooling Performance on the Trailing Edge Cut-Back of Gas Turbine Airfoils*, School and Institute for Flow and Thermal Machines, University Karlsruhe, Germany, ALSTROM Power Technology Centre, GT2005-68084, Proceedings of the ASME Turbo Expo, June 2005.

[17]   Martini, P., Schulz, A., Bauer, H. J., Whitney, C.F., *Film Cooling Effectiveness and Heat Transfer on the Trailing Edge Cut-Back of Gas Turbine Airfoils with Various Internal Cooling Designs,* School and Institute for Flow and Thermal Machines, University Karlsruhe, Germany, GT2005-68083, Proceedings of the ASME Turbo Expo, June 2005.

[18]   Je-Chin, H., Dutta, S., Srinath, V. E., *Gas turbine Heat Transfer and Cooling Technology*, ISBN. 1-56032-841-X, Taylor & Francis, 2000.

[19]   Florschuetz, L. W., Metzger, D. E., Truman, C. R., *Jet Array Impingement With Crossflow – Correlation of Streamwise Resolved Flow and Heat Transfer Distributions*, NASA Contractor Report 3373, January 1981.

[20]   Florschuetz, L. W., Metzger, D. E., Takeuchi, D. I., Berry, R. A., *Multiple Jet Impingement Heat Transfer Characteristics – Experimental Investigation of In-Line and Staggered Arrays With Crossflow*, NASA Contractor Report 3217, 1980.

[21]   Yeh, F. C., Stepka, F. S., *Review and Status of Heat-Transfer Passages of Air-Cooled Turbine Blades*, Lewis Research Centre Cleveland, Ohio, NASA Technical Paper 2232, 1984.

[22]   Hannis, J. M., Smith, M. K. D., *The Design and Testing of Air-Cooled Blading for an Industrial Gas Turbine,* Ruston Gas Turbines Ltd., Lincoln LN2 5DJ England., Transactions of the ASME, Journal of Engineering for Power, Vol. 105, July 1983.

[23]   Sunden, B., Jia, R., Abdon, A., *Computation of Combined Turbulent Convective and Impingement Heat Tranfer,* Division of Heat Transfer, Lund Institute of Technology, Lund, Sweden, International Journal of Numerical Methods for Heat and Fluid Flow, Vol. 14, No. 1, 2004, pp 116-133.

[24]   Heidmann, J. D., Kassab, A. J., Divo, E. A., Rodriguez, F., *Conjugate Heat Transfer Effects on a Realistic Film-Cooled Turbine Vane*, Proceedings of the ASME Turbo Expo, Power for Land, Sea, and Air, June 16-19, 2003, Atlanta, Georgia, USA.

[25]   Colban, W., Gratton, A., Thole, K. A., *Heat Transfer and Film Cooling Measurements on a Stator Vane with Fan-Shaped Cooling Holes*, Mechanical Engineering Department, Virginia Tech, Blacksburg, Virginia, ASA, Proceedings of the ASME Turbo Expo, Power for Land, Sea, and Air, June 6-9, 2005, Reno-Tahoe, Nevada, USA.

[26] Uzol, O., Camci, C., *Aerodynamic Loss Characteristic of a Turbine Blade with Trailing Edge Coolant Ejection: Part 2 – External Aerodynamics, Total Pressure Losses, and Predictions*, Transactions of the ASME Journal of Turbomachinery, Vol. 1, April 2001.

[27] Denton, J. D., *A Suite Of Computer Programs for Calculating Fully 3D Flow Through All Types of Turbo Machine Blade Rows*, Whittle Laboratory, Cambridge University, UK, 1983.

[28] Denton, J. D., *A Suite of Computer Programs for Calculating Fully 3D Flow Through All Types of Turbomachine Blade Rows,* Whittle Laboratory, Cambridge University, UK, 1983.

[29] Lau, S. C., Han. J. C., Batten, T., *Heat Transfer, Pressure Drop, and Mass Flow Rate in Pin Fin Channels With Long and Short Trailing Edge Ejection Holes*, Transactions of the ASME Journal of Turbomachinery, Vol. 111, April 1989.

[30] Crawford, M. E., Kays, W. M., *STAN5 – A Program for Numerical Computation of Two-Dimensional Internal and External Boundary Layer Flows*, NASA Contractor Report, NASA CR-2742, Stanford University, November 1976.

[31] Snedden, G. C., *Quasi-3D Simulation of a Real Disc Cavity with Conjugate Heat Transfer*, SCIR, Defencetek, 2001.

[32] Gaugler, R. E., *TACT1, A Computer Program for the Transient Thermal Analysis of a Cooled Turbine Blade or Vane Equipped with a Coolant Insert – I-Users Manual,* NASA Scientific and Technical Information Office, NASA TP-1271, 1978.

[33] White, F. M., *Viscous Fluid Flow*, Second Edition, McGraw-Hill ISBN 0-07-069712-4, 1991.

[34] Iacacarino, G., *Prediction of the Turbulent Flow in a Diffuser with Commercial CFD codes,* Center for Turbulence Research, Annual Research Briefs, 2000.

[35] Iacacarino, G., *Prediction of the Turbulent Separated Flow Using Commercial CFD Codes,* Center for Turbulence Research, Stanford University, Stanford, CA 94305-3030, Journal of Fluids Engineering, Vol. 123/891, December 2001.

[36] FLUENT 6.2 Documentation Manual, FLUENT Inc., 2006.

[37] Cheng, L., Wu, T., *Confined and Submerged Turbulent Jet Impingement Cooling Heat Transfer,* Report for ME 605 Final Project, School of Nuclear Engineering, Purdue University, December 2003.

[38] Kalitzin, G., Iaccarini, G., *Towards Immersed Boundary Simulation of High Reynolds Number Flows*, Centre for Turbulence Research, Annual Research Briefs, 2003.

[39] Magi, A., Montomoli, F., Adami, P., Carcasci, C., *Experimental and Numerical Investigation of Stationary Ribbed Ducts*, University of Florence, GT2004-53180, Proceedings of the ASME Turbo Expo, June 2004.

[40] Garg, V. K., Rigby, D. L., *Heat Teansfer on a Film-Cooled Blade – Effect of Hole Physics*, AYT Corporation, Cleveland, Ohio, NYMA, Inc, Brook Park, Ohio, NASA/CR-1998-206609, Prepared for Turbo Expo, 1998.

[41] Ameri, A. A., Rigby, D. L., Steinthorsson, E., *Computation of Turbulent Heat Transfer on the Walls of a 180 degree Turn Channel With a Low Reynolds Number Reynolds Stress Model*, University of Toledo, Ohio, QSS Group, Inc, Cleveland, Ohio, A&E Consulting, Inc, Westlake, Ohio, NASA/CR-2002-211515, GT-2002-30211, Prepared for the Turbo Expo, June 2002.

[42]   NREC Manual, *The Design and Performance Analysis of Axial-Flow Turbines, Volume II – User Guide to the Computer Programs,* Northern Research and Engineering Corporation, Cambridge, Massachusetts, 14 September 1972.

[43]   NREC Manual, *The Design and Performance Analysis of Axial-Flow Turbines, Volume I – Theory and Practice of Design,* Northern Research and Engineering Corporation, Cambridge, Massachusetts, 14 September 1972.

[44]   Patankar, S. V., Spalding, D. B., *Heat and Mass Transfer in Boundary Layers*, Morgan-Grampian: London, 1967.

[45]   DGXY Application Version 1. Copyright Mark James, 1994 – 1998.

[46]   MATLAB Version 7.0.1.24704 (R14) Service Pack 1 September 16, 2004. Copyright 1984 – 2004, The MathWorks Inc.

[47]   Detroit Diesel Allison, *Allison Gas Turbines 501-D22, D22A Operating Manual,* Revised 18 September 1975.

[48]   Sontag, R. E., Borgnakke, C., Van Wylen, G. J., *Fundamentals of Thermodynamics,* Wiley and Sons, ISBN 0-471-18361-X, Fifth Edition, 1998.

[49]   Skidmore, F. W., *Smoke Emission Test on Series II and III Allison T56 Turboprop Engines,* Aero Propulsion Technical Memorandum 438, AR-004-511, Department of Defence, Defence Science and Technology Organisation (DSTO), Aeronautical Research Laboratories (ARL), March 1990.

[50]   Skidmore, F. W., Hunt D. R., Doogood, P. N., *The Reduction of Smoke Emissions from Allison T56 Engines*, ARL-PROP-R-182, AR-006-055, Department of Defence, Defence Science and Technology Organisation (DSTO), Aeronautical Research Laboratories (ARL), March 1990.

[51]   Walsh, P. P., Fletcher. P., *Gas Turbine Performance,* Blackwell Science Ltd., ISBN 0-7918-0067-9, 1998.

[52]   Abu-Ghannam, B. and Shaw, R., *Natural Transition of Boundary Layers - The Effects of Turbulence, Pressure Gradient and Flow History*, Journal of Mechanical Engineering Science, Vol. 22, pp. 213-228, 1980.

[53]   Menter, F. R., *Improved Two-Equation k-ω Turbulence Models for Aerodynamic Flows,* NASA Technical Memorandum 103975, October 1992.

[54]   Van Niekerk, J. E., Meyer, C. J, Morris, R. M, *Prediction of the T56 Turbine Inlet Temperature Profile with an Abnormal Fuel Distribution,* ISABE-2005-1229, 2005.

APPENDIX A

NREC, LOSS3D, STAN5 AND
TACT1 PROCEDURE

TDML

The first step in the analysis process of the T56 NGV used TDML, a package where the correlation between the exit Mach number and the correct geometrical flow angle is determined. Due to variations of Cp with respect to fuel/air ratio and temperature, an empirical correlation for kerosene in dry air was used as determined by Walsh [51].

The following input data was used: Figure A1 represents the inlet boundary conditions to the NGV. Station 1, as seen in Figure A2, represents the first-stage NGV. Station 2, as seen in Figure A3, is the first rotor blade section. Station 3, as seen in Figure A4 is the exit of the first-stage rotor blades.

```
Comment describing the case to be considered (may be left blank):
T56 take-off maximum
Turbine inlet configuration (Duct = 2, Diffuser = 1, Neither = 0): 0
Turbine outlet configuration (Duct = 2, Diffuser = 1, Neither = 0): 0
Required turbine loss correlation (Small = 0, Large = 1): 1

Number of stages in unit: 1          Gas constant of fluid: 287.0 (J/kg K)
Inlet total temperature: 1350.0 (K)  Inlet total pressure:  901.7 (kPa)
Mass flow rate:  14.024 (kg/s)       Inlet swirl velocity:   0.0  (m/s)
Critical Reynolds number: 3.0E5      Rotor metal density:  7800.0 (kg/m^3)
```

Fig. A1 NGV inlet boundary conditions

```
                Input Data for Station #1
Specific heat (Cp): 1246.0 (J/kg K)   Viscosity: 5.040E-5 (N-s/m²)
Hub radius: 198.9 (mm)                Tip radius: 229.0 (mm)

                Input Data for Blade Row #1
        Stator Exit Flow Data:        either Flow angle:  0.0 (°)
                                        or Swirl velocity: 428.5 (m/s)
Number of blades:  60                 [leave one blank]
Trailing edge thickness: 1.00 (mm)    Tip clearance: 0.00 (mm)
```

Fig. A2 First stage NGV input data

Input Data for Station #2	
Specific heat (Cp): 5230.8 (J/kg K)	Viscosity: 5.074E-5 (N-s/m²)
Hub radius: 199.4 (mm)	Tip radius: 229.6 (mm)

Input Data for Blade Row #2	
Stage power required: 2364.5 (Kw)	Rotor rotational speed: 13820 (RPM)
Number of blades: 102	Rotor hub-to-tip area ratio: 1.5
Trailing edge thickness: 1.00 (mm)	Tip clearance: 0.10 (mm)

Fig. A3 First rotor blades

Input Data for Station #3	
Specific heat (Cp): 1231.0 (J/kg K)	Viscosity: 4.925E-5 (N-s/m²)
Hub radius: 199.4 (mm)	Tip radius: 230.0 (mm)

Fig. A4 Rotor blade exit section

The following results are obtained from TDML:

(file name: T56MAR2 .OUT)

Comment:
T56 take-off maximum

Turbine Performance	w/o diffusers	with diffusers
Total efficiency	0.9512	0.9512
Static efficiency	0.7980	0.7980
Total pressure ratio	1.6222	1.6222
Static pressure ratio	1.7917	1.7917

Fig. A5 Turbine performance values

122

Stage Data	
Loading factor	0.663
Flow factor	0.7132
Rotor efficiency	0.9556
Total efficiency	0.9512
Static efficiency	0.7980
Total press ratio	1.622
Reaction	3.0294

Blade Row Data	Stator	Rotor
Inlet (abs) Mach no	0.2156	------
Exit (abs) Mach no	0.7434	0.3927
Exit (rel) Mach no	0.3629	0.7124
Hub Exit (abs) Mach no	0.7926	0.3883
Exit loss coefficient	0.0754	0.0941
Exit flow angle	65.150	-24.76
Blade row reaction	0.6772	0.5303
Blade aspect ratio	0.00	0.00
Optimum blade number	0	0

Fig. A6 Stage 1 data

The exit flow angle obtained was compared with the measured geometrical averaged flow angle. Adjustments were made to the swirl velocity and the process was repeated in an iterative fashion until the measured flow angle corresponded to the calculated one.
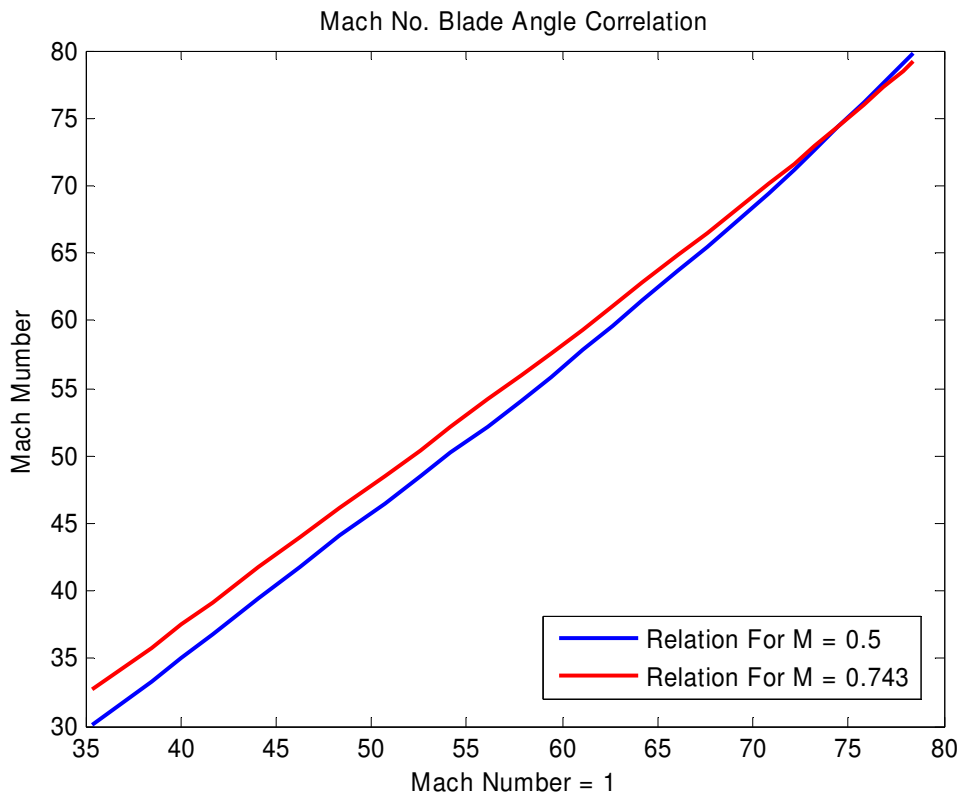
Fig. A7 Mach number correlation

TD3D

Now the Mach number, corrected with respect to the actual geometry of the blade, pressure and temperature, was taken into account as well. Modified turbine inlet temperature profile as obtained from DSTO T56 rig data [49] [50] was used along with combustor exit pressure as calculated before. The following input data was used.

```
Comment describing the case to be considered (may be left blank):
T56 take-off maximum
Required turbine loss correlation (Small = 0, Large = 1): 0
Coolant schedule? (None = 0, Mass Flow = 1, Mass Flow & Total Temp = 2): 0
Mixing schedule? (None = 0, Mixing Specified = 1): 0
Gas forces to be calculated? (No = 0, Yes = 1): 1

Number of spools in turbine: 1        Gas constant of fluid: 287.0 (J/kg K)
Mass flow rate: 14.024 (kg/s)         Number of streamlines considered: 17
Number of radii at which inlet conditions are to be specified: 17
```

Fig. A8 TD3D input data - General

Data Specifying Conditions at Turbine Inlet	Radial Station	Radial Posn. (mm)	Total Temp. (K)	Total Press. (kPa)	Flow Angle (°)
	1	198.3	1201.4	901.7	0.0
	2	200.8	1244.5	901.7	0.0
	3	202.6	1291.4	901.7	0.0
	4	204.5	1331.6	901.7	0.0
	5	206.4	1361.0	901.7	0.0
	6	208.3	1379.9	901.7	0.0
	7	210.2	1390.6	901.7	0.0
	8	212.0	1396.1	901.7	0.0
	9	213.9	1398.7	901.7	0.0
	10	215.8	1399.4	901.7	0.0
	11	217.7	1387.8	901.7	0.0
	12	219.6	1392.0	901.7	0.0
	13	221.5	1379.3	901.7	0.0
	14	223.3	1357.3	901.7	0.0
	15	225.2	1325.4	901.7	0.0
	16	227.1	1286.4	901.7	0.0
	17	229.0	1249.3	901.7	0.0

Fig. A9 TD3D temperature, pressure and flow angle input data

```
Input Data for Spool #1
Rotor rotational speed: 13820.0 (RPM)
Spool power output required:  2364.5 (kW)
Number of stages on the spool: 1
Number of radii at which exit blade row conditions are to be specified:  3
```

Fig. A10 TD3D input data - Rotor rotational speed

```
Input Data for Spool #1, Stage #1

Fraction of spool power produced by stage: 1.000

   Specification of stator outlet conditions: 0
   (Derivative of meridional velocity = 0,
    Flow angle and subsonic solution = 1,
    Flow angle and supersonic solution = 2)

Axial co-ordinate at one station upstream of 1st stator: -20.1 (mm)

Hub radius at one station upstream of 1st stator: 199.9 (mm)

Tip radius at one station upstream of 1st stator: 229.0 (mm)
```

Fig. A11 TD3D input data – Spool number 1

```
Swirl velocity at mean radius: 384.0 (m/s)


Rotor exit distribution type: 1
(Uniform power output = 0,
 Specification of a gradient
 of meridional velocity = 1)
```

Radial Station	Radial Posn. (mm)	Deriv. of Merid'l Vel.
1	199.4	1550.0
2	214.5	350.0
3	229.6	-640.0
0	0.0	0.0
0	0.0	0.0
0	0.0	0.0
0	0.0	0.0
0	0.0	0.0
0	0.0	0.0
0	0.0	0.0
0	0.0	0.0
0	0.0	0.0
0	0.0	0.0
0	0.0	0.0
0	0.0	0.0
0	0.0	0.0
0	0.0	0.0

Fig. A12 TD3D input data – Swirl velocity at stator exit

Radial Station	Radial Posn. (mm)	Deriv. of Merid'l Vel.
1	199.4	0.0
2	215.0	0.0
3	229.6	0.0
0	0.0	0.0
0	0.0	0.0
0	0.0	0.0
0	0.0	0.0
0	0.0	0.0
0	0.0	0.0
0	0.0	0.0
0	0.0	0.0
0	0.0	0.0
0	0.0	0.0
0	0.0	0.0
0	0.0	0.0
0	0.0	0.0
0	0.0	0.0

Fig. A13 TD3D input data – Rotor exit

```
                    ┌─────────────────────────┐
                    │        Spool #1         │
                    └─────────────────────────┘

        ┌───────────────────────────────────────────────┐
        │         Input Data for Station #1             │
        ├───────────────────────────────┬───────────────┤
        │ Specific heat (Cp): 1197.8 (J/kg K) │ Axial co-ordinate:    0.0 (mm) │
        │ Hub radius: 198.9 (mm)              │ Tip radius: 229.0 (mm)         │
        └───────────────────────────────┴───────────────┘

        ┌───────────────────────────────────────────────┐
        │          Input Data for Blade Row #1          │
        ├───────────────────────────────┬───────────────┤
        │ Trailing edge thickness: 1.00 (mm) │ Tip clearance: 0.00 (mm)       │
        │ Number of blades:  60              │                                │
        └───────────────────────────────┴───────────────┘
```

Fig. A14 TD3D input data for station 1

```
                    ┌─────────────────────────┐
                    │        Spool #1         │
                    └─────────────────────────┘

        ┌───────────────────────────────────────────────┐
        │         Input Data for Station #2             │
        ├───────────────────────────────┬───────────────┤
        │ Specific heat (Cp): 1197.8 (J/kg K) │ Axial co-ordinate:   21.3 (mm) │
        │ Hub radius: 204.9 (mm)              │ Tip radius: 234.4 (mm)         │
        └───────────────────────────────┴───────────────┘

        ┌───────────────────────────────────────────────┐
        │          Input Data for Blade Row #2          │
        ├───────────────────────────────┬───────────────┤
        │ Trailing edge thickness: 1.00 (mm) │ Tip clearance: 0.10 (mm)       │
        │ Number of blades: 102              │                                │
        └───────────────────────────────┴───────────────┘
```

Fig. A15 TD3D input data for station 2

```
                    ┌─────────────────────────┐
                    │        Spool #1         │
                    └─────────────────────────┘

        ┌───────────────────────────────────────────────┐
        │         Input Data for Station #3             │
        ├───────────────────────────────┬───────────────┤
        │ Specific heat (Cp): 1180.0 (J/kg K) │ Axial co-ordinate:   45.9 (mm) │
        │ Hub radius: 201.9 (mm)              │ Tip radius: 237.5 (mm)         │
        └───────────────────────────────┴───────────────┘
```

Fig. A16 15 TD3D input data for station 3

```
        ┌───────────────────────────────────────────────────────┐
        │ Input Data at One Station Downstream of Turbine Unit  │
        └───────────────────────────────────────────────────────┘

                ┌───────────────────────────────────────┐
                │ Axial co-ordinates:   54.5 (mm)       │
        ┌───────────────────────────────┬───────────────────────┐
        │ Hub radius: 201.0 (mm)        │ Tip radius: 239.3 (mm) │
        └───────────────────────────────┴───────────────────────┘
```

Fig. A17 15 TD3D input data – One station downstream of turbine unit

The following output data are obtained:

```
(file name: T56MAR2 .OUT)
```

```
Comment:
T56 take-off maximum
```

Mass Averaged Turbine Performance	
Total efficiency	0.8767
Static efficiency	0.7561
Total-total pressure ratio	1.6970
Total-static pressure ratio	1.8586

Fig. A18 TD3D output data – Mass-averaged turbine performance

Spool #1, Stage # 1	Stator			Rotor		
Blade Row Data	Hub	Mean	Tip	Hub	Mean	Tip
Inlet (abs) Mach no	0.1706	0.2206	0.2619	-------	-------	-------
Exit (abs) Mach no	0.6701	0.6031	0.5595	0.3641	0.3748	0.3759
Exit (abs) flow angle	66.26°	64.51°	62.17°	−30.42°	−38.50°	−34.55°
Exit (rel) Mach no	0.3144	0.2773	0.2652	0.7157	0.7600	0.8077
Exit (rel) flow angle	30.71°	19.58°	−2.81°	−64.08°	−67.30°	−67.64°
Reaction	0.7373	0.6254	0.5231	0.5478	0.6218	0.6576
Pressure loss coeff.	0.0858	0.0989	0.1057	0.1787	0.1715	0.1377
Efficiency	0.934	0.922	0.915	0.876	0.888	0.913

Fig. A19 TD3D output data – Stage 1 blade row data

Stage Data	Hub	Mean	Tip
Loading factor	1.7441	1.7027	1.3745
Flow factor	0.6375	0.6005	0.5445
Reaction	0.5461	0.6694	0.7507

Stage Data – Mass Averaged			
Pressure ratio	1.6970	Loading factor	1.6616
Total efficiency	0.8767	Stator loss coefficient	0.0982
Static efficiency	0.7561	Rotor loss coefficient	0.1682
Reaction	0.6644	Stator efficiency	0.9225
Flow factor	0.5962	Rotor efficiency	0.8935

Fig. A20 TD3D output data – Stage 1 mass-averaged stage data

Mass Averaged Spool Performance	
Power	2364.48
Total efficiency	0.8767
Static efficiency	0.7561
Total-total pressure ratio	1.6970
Total-static pressure ratio	1.8586

Fig. A21 TD3D output data – Spool 1 mass-averaged performance

From the output data, implied flow angles due to the relevant Mach numbers at hub, midspan and casing are determined using the same interpolation technique as before with the help of data obtained by Cohen, Rogers and Saravanamuttoo [1]. As before, an iterative process was required to obtain the correct flow angles. This was a very tricky step in the analysis procedure due to the fact that four variables had to be changed during this iterative procedure. The swirl velocities were again changed along with the derivative of the meridinal velocity at the stator exit for hub, midspan and casing. This process is time-consuming as one needs to develop a feel for the derivative of meridinal velocity effects along with swirl velocity magnitude.

STAN5

Data obtained from NREC was used for creating an input file for LOSS3D. Below is the input file used for take-off condition. Seven sections were made through the blade and its three dimensional co-ordinates specified. The correct Cp and gamma values are used as determined by Walsh and Fletcher [51]. Geometry was created using a sub-routine after which an implicit Euler solver was used to solve for pressure, Mach number, heat transfer coefficient and temperature distributions on the blade surface.

Convergence is quick and takes roughly 500 iterations.

```
$TITL TITLE  = 'T56 Take off – (14/06/2006) M Botha',
      LOSS3D = .TRUE. ,
      BTOB3D = .FALSE.,
 $END
 $CCVI IM     =    17,
       JM     =    55,
       KM     =    17,
       NBLADE =    60,
       NMAX   =    1000,
       INPUT  =    1,
       NOSECT =    7,
       INMACH =    2,
       INVR   =    0,
 $END
 $CCVR FAC1   = 0.001,
       FAC2   = 0.001,
       FAC3   = 0.001,
       FAC4   = 0.001,
       RPM    = 0.0,
       CP     = 1246.219,
       GA     = 1.299202,
 $END
 $DATAIN PERIN  = 25.0,
         PERON  = 50.0,
         PEROUT = 25.0,
         SWIRL  = 0.0,  0.0,  0.0,  0.0,  0.0,  0.0,  0.0,  0.0,
0.0,
                  0.0,  0.0,  0.0,  0.0,  0.0,  0.0,  0.0,  0.0,
         PITCH  = 0.0,  0.0,  0.0,  0.0,  0.0,  0.0,  0.0,  0.0,
0.0,
                  0.0,  0.0,  0.0,  0.0,  0.0,  0.0,  0.0,  0.0,
         RLE= 195,  204.18,  207.98,  214.88,  222.16,  225.56,
230,
         RTE= 195,  204.18,  207.98,  214.88,  222.16,  225.56,
230,
         AMERIN = −8.82, −8.82, 0.0, 0.0, 0.0,  3.16,  3.16,
         AMEROT = 2.32,   2.32, 0.0, 0.0, 0.0, −5.83,  −5.83,
         PINLET = 884647.5, 862151.7,
```

```
        PEXIT  = 663782.3, 723621.6,
        PO11   = 950211,        950211,        950211,        950211,
950211,
                 950211,        950211,        950211,        950211,
950211,
                 950211,        950211,        950211,        950211,
950211,
                 950211,        950211,
        TO11   = 1201.481,     1244.552,     1291.459,     1331.612,
1361.043,
                 1379.95,      1390.683,     1396.16,      1398.729,
1399.454,
                 1397.849,     1392.036,     1379.353,     1357.383,
1325.433,
                 1286.438,     1249.311,
        VTIN1  = 0.0,  0.0,  0.0,  0.0,  0.0,  0.0,  0.0,  0.0,
0.0,
                  0.0,  0.0,  0.0,  0.0,  0.0,  0.0,  0.0,  0.0,
        VM11   =    115.272, 122.003, 129.022, 135.54, 141.312,
146.477, 151.209, 155.661, 159.657,
                 163.42, 167.197, 170.542, 173.09, 175.083, 176.614,
177.851, 179.029,
        RIN    =    198.93,    199.48,
        ROUT   =    229.03,    229.6,
 $END
 $BLAD   BLDMAG = 1.0,
         TRANS  = 0.0,
         ANGIN  = 0.0, 0.0, 0.0, 0.0, 0.0, 0.0, 0.0,
         ANGOUT = 66.5, 67.0, 70.4, 67.6, 68.0, 68.5, 69.1,
         NSUCT=   26,    27,    27,    28,    28,    26,    29,
         NPRES=   23,    25,    23,    24,    24,    25,    23,
         ICUSP  = 1,
         LECUSP = 0,
         TECUSP = 0,
         SHIFLE = 0.5,
         SHIFTE = 0.5,
         IDATA  = 0,
         XSHIFT = −18.0,
         YSHIFT = 3.5,
 $END
 $RELGRD
```

```
$END
$SUCT COORDS=
      18.96763,   -2.290976,
      18.999182,  -2.094238,
      19.190666,  -1.790506,
      19.465171,  -1.541072,
      19.7, -1.428043,
      20.2, -1.321932,
      21.2, -1.170838,
      22.2, -1.098458,
      23.2, -1.133713,
      24.2, -1.269693,
      25.2, -1.488097,
      26.2, -1.871454,
      27.2, -2.414883,
      28.2, -3.114381,
      29.2, -4.003923,
      30.2, -5.177006,
      31.2, -6.705734,
      32.2, -8.638005,
      33.2, -10.67587,
      34.2, -12.811069,
      35.2, -15.058846,
      36.2, -17.509279,
      37.2, -20.382221,
      37.761225,  -22.365763,
      38.0429,    -23.622686,
      38.093116,  -23.873279,
$END
$PRES COORDS=
      18.974972,  -2.379069,
      19.119759,  -2.665956,
      19.358151,  -2.907451,
      20.2, -3.563374,
      21.2, -4.171322,
      22.2, -4.854338,
      23.2, -5.590202,
      24.2, -6.381284,
      25.2, -7.237515,
      26.2, -8.165976,
      27.2, -9.168459,
```

```
        28.2, -10.250403,
        29.2, -11.386823,
        30.2, -12.574647,
        31.2, -13.830407,
        32.2, -15.162458,
        33.2, -16.579302,
        34.2, -18.07989,
        35.2, -19.646859,
        36.2, -21.255088,
        37.2, -22.999391,
        37.590055,  -23.670767,
        37.830846,  -24.037702,
$END
$SUCT COORDS=
        18.932651,  -2.407606,
        19.014038,  -2.083642,
        19.2, -1.829467,
        19.403067,  -1.659986,
        19.7, -1.521624,
        20.2, -1.408489,
        21.2, -1.257837,
        22.2, -1.214566,
        23.2, -1.278972,
        24.2, -1.446857,
        25.2, -1.712344,
        26.2, -2.092921,
        27.2, -2.618496,
        28.2, -3.31615,
        29.2, -4.22969,
        30.2, -5.461675,
        31.2, -7.003569,
        32.2, -8.920811,
        33.2, -10.953258,
        34.2, -13.069741,
        35.2, -15.285645,
        36.2, -17.660295,
        37.2, -20.358729,
        37.856668,  -22.529445,
        38.104685,  -23.571949,
        38.142619,  -24.35249,
        38.231162,  -24.182123,
```

```
$END
$PRES COORDS=
      18.935323,   -2.46235,
      18.982967,   -2.640739,
      19.064111,   -2.764043,
      19.2, -2.903071,
      19.7, -3.340221,
      20.2, -3.719307,
      21.2, -4.36244,
      22.2, -5.044373,
      23.2, -5.78243,
      24.2, -6.575745,
      25.2, -7.434206,
      26.2, -8.365664,
      27.2, -9.372774,
      28.2, -10.460153,
      29.2, -11.605158,
      30.2, -12.805836,
      31.2, -14.079113,
      32.2, -15.432649,
      33.2, -16.875296,
      34.2, -18.390959,
      35.2, -19.923458,
      36.2, -21.511086,
      37.2, -23.167506,
      37.623464,   -23.819452,
      37.985979,   -24.359375,
$END
$SUCT COORDS=
      18.892719,   -2.494266,
      18.946959,   -2.228764,
      19.2, -1.875918,
      19.35154,    -1.758648,
      19.7, -1.59875,
      20.2, -1.48005,
      21.2, -1.330729,
      22.2, -1.307691,
      23.2, -1.391895,
      24.2, -1.580021,
      25.2, -1.872701,
      26.2, -2.273993,
```

```
     27.2, -2.787995,
     28.2, -3.483813,
     29.2, -4.423757,
     30.2, -5.686883,
     31.2, -7.244391,
     32.2, -9.147873,
     33.2, -11.171514,
     34.2, -13.265779,
     35.2, -15.436948,
     36.2, -17.743232,
     37.2, -20.315614,
     38.2, -23.742873,
     38.307614,  -24.248561,
     38.345697,  -24.438369,
     38.243623,  -24.607446,
 $END
 $PRES COORDS=
     18.901383,  -2.60892,
     18.993326,  -2.842796,
     19.2, -3.049905,
     19.7, -3.459081,
     20.2, -3.841251,
     21.2, -4.516357,
     22.2, -5.198589,
     23.2, -5.939066,
     24.2, -6.735081,
     25.2, -7.59612,
     26.2, -8.530646,
     27.2, -9.542086,
     28.2, -10.634549,
     29.2, -11.787746,
     30.2, -13.000425,
     31.2, -14.288596,
     32.2, -15.660724,
     33.2, -17.119274,
     34.2, -18.621994,
     35.2, -20.125068,
     36.2, -21.672144,
     37.2, -23.242525,
     38.047959,  -24.573818,
 $END
```

```
$SUCT COORDS=
     18.804269,  -2.672199,
     18.891983,  -2.330677,
     19.047847,  -2.108661,
     19.2, -1.976903,
     19.257977,  -1.937798,
     19.7, -1.737613,
     20.2, -1.609421,
     21.2, -1.465177,
     22.2, -1.472067,
     23.2, -1.583936,
     24.2, -1.798744,
     25.2, -2.123367,
     26.2, -2.566979,
     27.2, -3.096843,
     28.2, -3.789233,
     29.2, -4.793259,
     30.2, -6.085071,
     31.2, -7.662211,
     32.2, -9.539536,
     33.2, -11.524255,
     34.2, -13.569804,
     35.2, -15.638308,
     36.2, -17.814379,
     37.2, -20.207202,
     38.2, -23.337394,
     38.434493,  -24.329523,
     38.553669,  -24.903657,
     38.439846,  -25.063939,
$END
$PRES COORDS=
     18.816453,  -2.821655,
     18.930883,  -3.104008,
     19.066133,  -3.242953,
     19.2, -3.342874,
     19.7, -3.700224,
     20.2, -4.066045,
     21.2, -4.774197,
     22.2, -5.468728,
     23.2, -6.215073,
     24.2, -7.018467,
```

```
      25.2, -7.886376,
      26.2, -8.828226,
      27.2, -9.848942,
      28.2, -10.952345,
      29.2, -12.123478,
      30.2, -13.360329,
      31.2, -14.674231,
      32.2, -16.073385,
      33.2, -17.515838,
      34.2, -18.93455,
      35.2, -20.373654,
      36.2, -21.891938,
      37.2, -23.382517,
      38.2, -24.979504,
$END
$SUCT COORDS=
      18.703974,  -2.989682,
      18.698928,  -2.912479,
      18.720399,  -2.70952,
      18.817709,  -2.467209,
      19.159262,  -2.126815,
      19.2, -2.102355,
      19.7, -1.882623,
      20.2, -1.745148,
      21.2, -1.610377,
      22.2, -1.641635,
      23.2, -1.773387,
      24.2, -2.006906,
      25.2, -2.350202,
      26.2, -2.813543,
      27.2, -3.405545,
      28.2, -4.114263,
      29.2, -5.186654,
      30.2, -6.484686,
      31.2, -8.066143,
      32.2, -9.911269,
      33.2, -11.829244,
      34.2, -13.781202,
      36.2, -17.807269,
      37.2, -20.069705,
      38.2, -23.00095,
```

```
       38.597025,   -24.562993,
       38.773094,   -25.394571,
       38.654353,   -25.542589,
  $END
  $PRES COORDS=
       18.787634,   -3.278026,
       18.967703,   -3.513343,
       19.2, -3.67108,
       19.7, -3.989977,
       20.2, -4.323843,
       21.2, -5.015554,
       22.2, -5.733118,
       23.2, -6.490531,
       24.2, -7.30627,
       25.2, -8.185615,
       26.2, -9.138559,
       27.2, -10.17168,
       28.2, -11.289979,
       29.2, -12.485611,
       30.2, -13.744347,
       31.2, -15.070391,
       32.2, -16.434611,
       33.2, -17.778785,
       34.2, -19.141025,
       35.2, -20.561927,
       36.2, -22.018783,
       37.2, -23.533003,
       38.2  -25.129318,
       38.473892,   -25.534542,
  $END
  $SUCT COORDS=
       18.7, -2.702617,
       18.856243,   -2.430202,
       19.113159,   -2.215091,
       19.2, -2.165041,
       19.7, -1.949872,
       20.2, -1.808274,
       21.2, -1.679386,
       22.2, -1.720015,
       23.2, -1.85841,
       24.2, -2.098457,
```

```
        25.2, -2.447113,
        26.2, -2.915022,
        27.2, -3.521645,
        28.2, -4.268191,
        29.2, -5.360934,
        30.2, -6.667552,
        31.2, -8.235638,
        32.2, -10.059493,
        33.2, -11.943581,
        34.2, -13.85027,
        35.2, -15.787623,
        36.2, -17.782825,
        37.2, -20.000701,
        38.2, -22.862833,
        38.596006,  -24.346829,
        38.875573,  -25.623843,
    $END
    $PRES COORDS=
        18.65034,   -2.925722,
        18.651941,  -3.089667,
        18.7, -3.302372,
        18.879731,  -3.601903,
        19.2, -3.828356,
        19.7, -4.133616,
        20.2, -4.453189,
        21.2, -5.128033,
        22.2, -5.845687,
        23.2, -6.611802,
        24.2, -7.435375,
        25.2, -8.322075,
        26.2, -9.281821,
        27.2, -10.321961,
        28.2, -11.44892,
        29.2, -12.658188,
        30.2, -13.919006,
        31.2, -15.228075,
        32.2, -16.54108,
        33.2, -17.862434,
        34.2, -19.21178,
        35.2, -20.625467,
        36.2, -22.0814,
```

```
      37.2, -23.60381,
      38.2, -25.201591,
$END
$SUCT COORDS=
      18.605303,  -3.179316,
      18.60312,   -3.027844,
      18.7, -2.680348,
      19.07248,   -2.292983,
      19.2, -2.22165,
      19.7, -2.008976,
      20.2, -1.863838,
      21.2, -1.740897,
      22.2, -1.788872,
      23.2, -1.931947,
      24.2, -2.176903,
      25.2, -2.529025,
      26.2, -2.99926,
      27.2, -3.608939,
      28.2, -4.406183,
      29.2, -5.514038,
      30.2, -6.827668,
      31.2, -8.372274,
      32.2, -10.176661,
      33.2, -12.026146,
      34.2, -13.899225,
      35.2, -15.79998,
      36.2, -17.75239,
      37.2, -19.938045,
      38.2, -22.747933,
      38.647633,  -24.386309,
      38.828585,  -25.166522,
      38.965996,  -25.826143,
      38.8249,    -25.970936,
$END
$PRES COORDS=
      18.7, -3.510598,
      19.2, -3.968608,
      19.7, -4.262882,
      20.2, -4.571863,
      21.2, -5.229147,
      22.2, -5.941736,
```

```
23.2,  -6.71392,
24.2,  -7.545702,
25.2,  -8.440269,
26.2,  -9.407124,
27.2,  -10.454275,
28.2,  -11.590126,
29.2,  -12.811368,
30.2,  -14.062101,
31.2,  -15.333793,
32.2,  -16.616382,
33.2,  -17.919452,
34.2,  -19.267498,
35.2,  -20.674295,
36.2,  -22.13807,
37.2,  -23.666526,
38.2,  -25.26527,
38.608297,  -25.930944,
$END
```

STAN5 solved for heat transfer coefficients using a marching scheme starting at the leading edge and working its way to the trailing edge of the blade. Seventeen sections through the blade were considered. Turbulence intensity was one of the inputs for STAN5. It is very difficult to know the exact intensity but a good estimate is a value between 6 and 10%. An average value of 8% was considered. High values of turbulence intensity did not exhibit behaviour of turbulence breakaway, whereas low levels did show turbulent breakaway. This is an unwanted flow pattern and changes were made to the gradients of the velocity until turbulent breakaway ceases. This was done for all 17 sections through the blade.
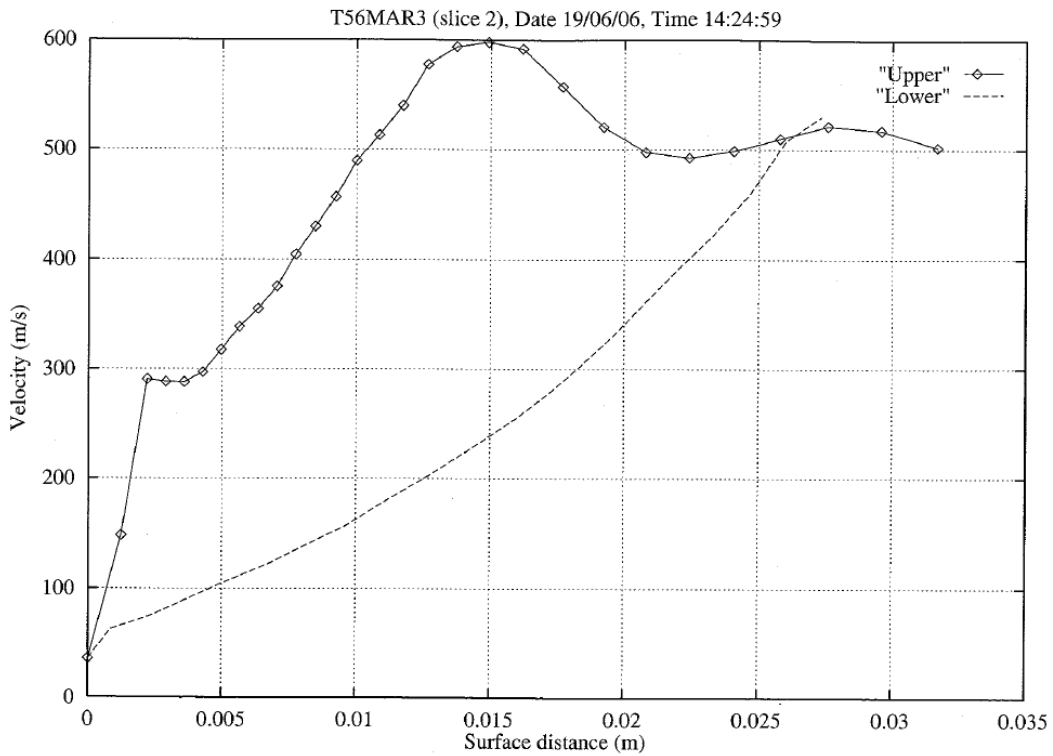
Fig. A22 STAN5 velocity profile for slice 2 – Unchanged velocity gradient
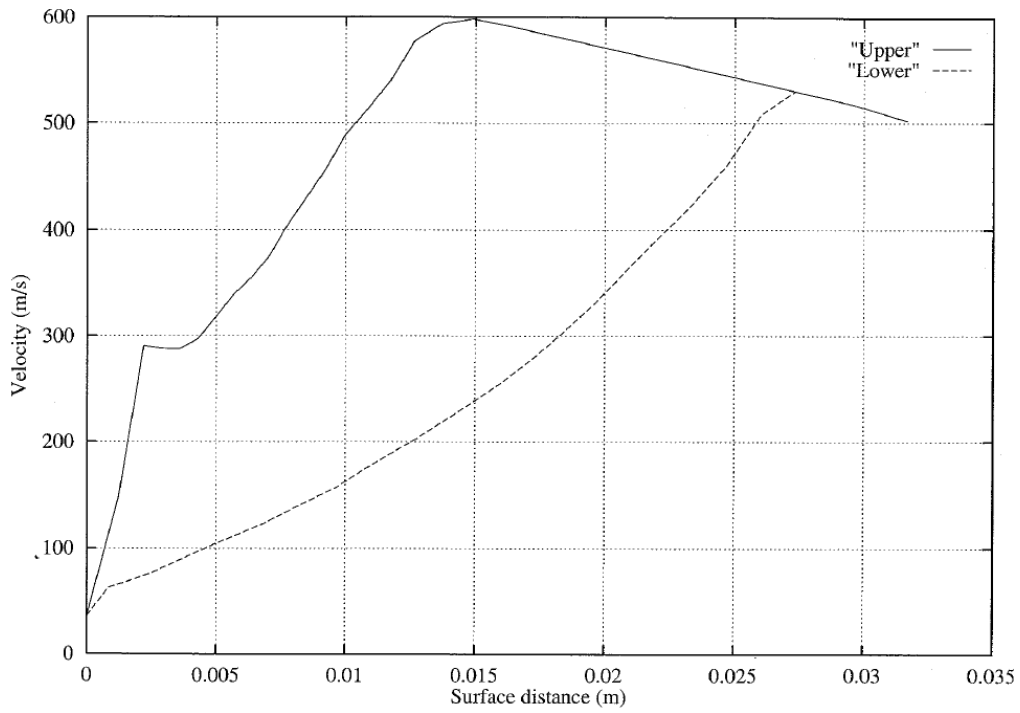
Fig. A23 STAN5 velocity profile for slice 2 – Changed velocity gradient
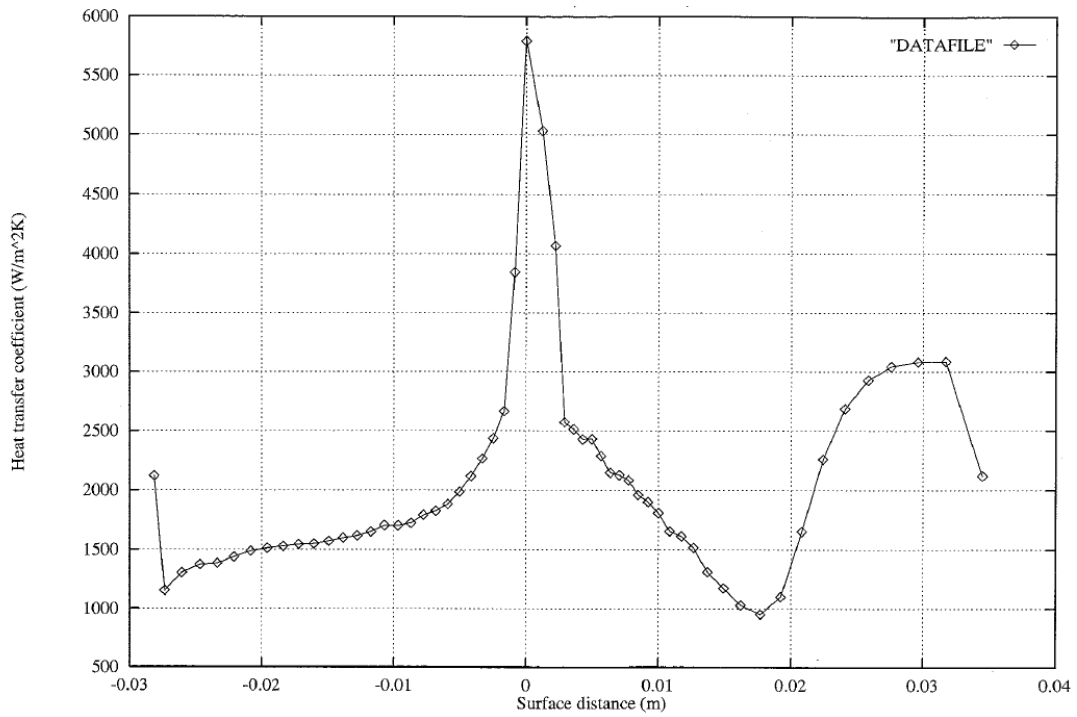

Fig. A24 STAN5 heat transfer coefficients for slice 2

The following table is a summary of the output file that was generated. This file was used by TACT1 when computing for the internal coolant flow.

Suction Surface	X (m)	Y (m)	Z (m)	P (Bar)	T0 (K)	HTTR (W/m^2K)
Table A1 TACT1 Output File
1	9.66E-04	1.36E-03	1.99E-01	9.03E+00	1.20E+03	5.05E+03
2	1.65E-03	2.03E-03	1.99E-01	8.05E+00	1.20E+03	4.07E+03
3	2.33E-03	2.18E-03	1.99E-01	7.88E+00	1.20E+03	2.49E+03
4	3.02E-03	2.29E-03	1.99E-01	8.11E+00	1.20E+03	2.45E+03
5	3.70E-03	2.35E-03	1.99E-01	8.21E+00	1.20E+03	2.39E+03
6	4.39E-03	2.37E-03	1.99E-01	8.09E+00	1.20E+03	2.41E+03
7	5.07E-03	2.34E-03	1.99E-01	7.88E+00	1.20E+03	2.28E+03
8	5.75E-03	2.26E-03	1.99E-01	7.72E+00	1.20E+03	2.14E+03
9	6.44E-03	2.14E-03	1.99E-01	7.61E+00	1.20E+03	2.13E+03
10	7.12E-03	1.98E-03	1.99E-01	7.42E+00	1.20E+03	2.09E+03
11	7.81E-03	1.73E-03	1.99E-01	7.11E+00	1.20E+03	1.96E+03
12	8.49E-03	1.43E-03	1.99E-01	6.85E+00	1.20E+03	1.89E+03
13	9.17E-03	1.06E-03	1.99E-01	6.61E+00	1.20E+03	1.79E+03
14	9.86E-03	5.83E-04	1.99E-01	6.29E+00	1.20E+03	1.65E+03
15	1.05E-02	3.85E-05	1.99E-01	6.07E+00	1.20E+03	1.62E+03
16	1.12E-02	-5.80E-04	1.99E-01	5.80E+00	1.20E+03	1.52E+03
17	1.19E-02	-1.40E-03	1.99E-01	5.38E+00	1.20E+03	1.32E+03
18	1.26E-02	-2.35E-03	1.99E-01	5.30E+00	1.20E+03	1.19E+03
19	1.33E-02	-3.43E-03	1.99E-01	5.45E+00	1.20E+03	1.05E+03
20	1.40E-02	-4.75E-03	1.99E-01	5.62E+00	1.20E+03	9.42E+02
21	1.46E-02	-6.11E-03	1.99E-01	6.11E+00	1.20E+03	1.07E+03
22	1.53E-02	-7.52E-03	1.99E-01	6.47E+00	1.20E+03	1.64E+03
23	1.60E-02	-8.98E-03	1.99E-01	6.53E+00	1.20E+03	2.28E+03
24	1.67E-02	-1.05E-02	1.99E-01	6.41E+00	1.20E+03	2.71E+03
25	1.74E-02	-1.21E-02	1.99E-01	6.25E+00	1.20E+03	2.96E+03
26	1.81E-02	-1.37E-02	1.99E-01	6.11E+00	1.20E+03	3.07E+03
27	1.88E-02	-1.56E-02	1.99E-01	6.02E+00	1.20E+03	3.12E+03
28	1.94E-02	-1.76E-02	1.99E-01	6.24E+00	1.20E+03	3.11E+03
29	2.01E-02	-2.03E-02	1.98E-01	6.34E+00	1.20E+03	2.13E+03

| Pressure Surface	X (m)	Y (m)	Z (m)	P (Bar)	T0 (K)	HTTR (W/m^2K)
1	9.66E-04	1.36E-03	1.99E-01	9.03E+00	1.20E+03	5.05E+03
2	1.65E-03	3.26E-04	1.99E-01	9.77E+00	1.20E+03	5.78E+03
3	2.33E-03	-1.79E-04	1.99E-01	9.30E+00	1.20E+03	3.83E+03
4	3.02E-03	-5.96E-04	1.99E-01	9.27E+00	1.20E+03	2.63E+03
5	3.70E-03	-1.05E-03	1.99E-01	9.41E+00	1.20E+03	2.42E+03
6	4.39E-03	-1.53E-03	1.99E-01	9.40E+00	1.20E+03	2.26E+03
7	5.07E-03	-2.03E-03	1.99E-01	9.33E+00	1.20E+03	2.11E+03
8	5.75E-03	-2.57E-03	1.99E-01	9.31E+00	1.20E+03	1.98E+03
9	6.44E-03	-3.12E-03	1.99E-01	9.30E+00	1.20E+03	1.88E+03
10	7.12E-03	-3.71E-03	1.99E-01	9.28E+00	1.20E+03	1.82E+03
11	7.81E-03	-4.34E-03	1.99E-01	9.25E+00	1.20E+03	1.78E+03
12	8.49E-03	-5.00E-03	1.99E-01	9.21E+00	1.20E+03	1.72E+03
13	9.17E-03	-5.68E-03	1.99E-01	9.17E+00	1.20E+03	1.70E+03
14	9.86E-03	-6.42E-03	1.99E-01	9.13E+00	1.20E+03	1.70E+03
15	1.05E-02	-7.18E-03	1.99E-01	9.06E+00	1.20E+03	1.65E+03
16	1.12E-02	-7.96E-03	1.99E-01	8.98E+00	1.20E+03	1.61E+03
17	1.19E-02	-8.78E-03	1.99E-01	8.91E+00	1.20E+03	1.60E+03
18	1.26E-02	-9.62E-03	1.99E-01	8.82E+00	1.20E+03	1.57E+03
19	1.33E-02	-1.05E-02	1.99E-01	8.70E+00	1.20E+03	1.54E+03
20	1.40E-02	-1.14E-02	1.99E-01	8.58E+00	1.20E+03	1.54E+03
21	1.46E-02	-1.23E-02	1.99E-01	8.42E+00	1.20E+03	1.52E+03
22	1.53E-02	-1.33E-02	1.99E-01	8.22E+00	1.20E+03	1.51E+03
23	1.60E-02	-1.44E-02	1.99E-01	7.99E+00	1.20E+03	1.49E+03
24	1.67E-02	-1.54E-02	1.99E-01	7.71E+00	1.20E+03	1.44E+03
25	1.74E-02	-1.65E-02	1.99E-01	7.40E+00	1.20E+03	1.38E+03
26	1.81E-02	-1.76E-02	1.99E-01	7.08E+00	1.20E+03	1.37E+03
27	1.88E-02	-1.88E-02	1.99E-01	6.77E+00	1.20E+03	1.30E+03
28	1.94E-02	-1.99E-02	1.98E-01	6.41E+00	1.20E+03	1.15E+03
29	2.01E-02	-2.03E-02	1.98E-01	6.34E+00	1.20E+03	2.13E+03

APPENDIX B

STAN5 / TACT1 ILLUSTRATIONS
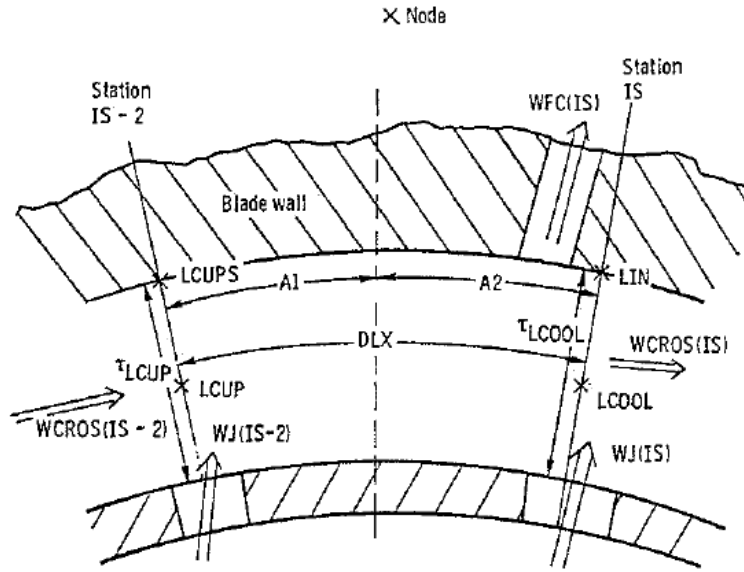
Fig. B1 Coolant – Channel Control Volume and Nomenclature [32]
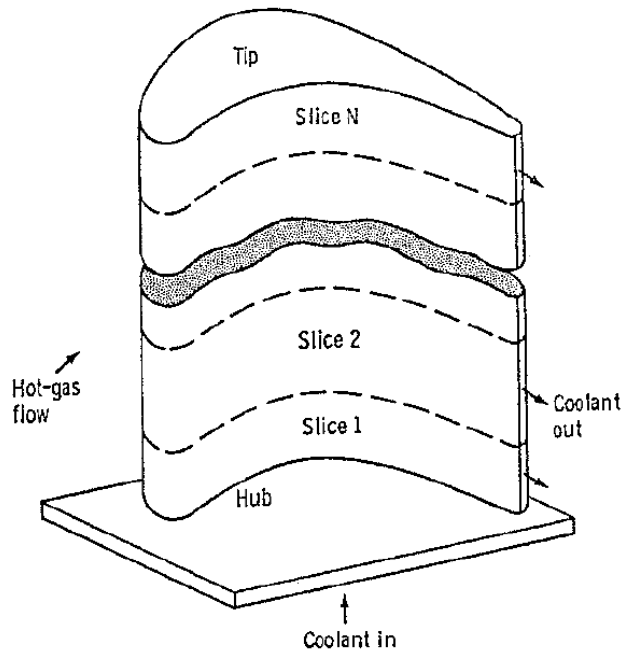

Fig. B2 Overall Division of Blade into Slices [32]
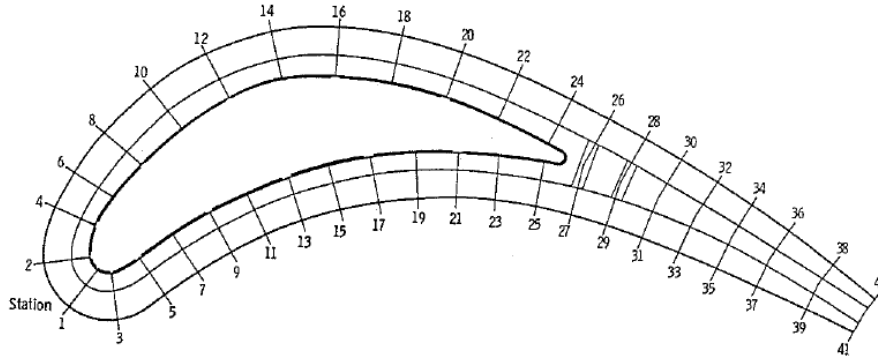
146

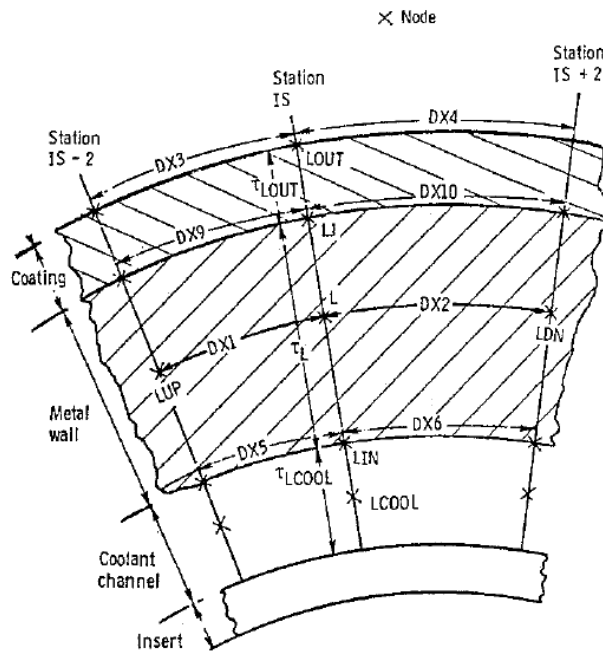*Fig. B3 Cross-Section Depicting 41 Stations [32]*

Fig. B4 Layout and nomenclature of coolant channel, where S_i is the spanwise dimension, normal to the paper [32]

APPENDIX C

ENGINE ANALYSIS FOR 20 000 FEET CRUISING CONDITIONS

Appendix C – Engine analysis for 20 000 feet cruising conditions

$P_0 = 46562.84\,Pa$

$$P_1 = \left(P_0\right)\left(1 + \left(\left(\frac{\gamma-1}{2}\right)\left(\frac{V_{Plane}}{a}\right)^2\right)^{\frac{\gamma}{\gamma-1}}\right)$$

$$P_1 = 101325\left(1 + \left(\left(\frac{1.4-1}{2}\right)\left(\frac{154.21}{316.01}\right)^2\right)^{\frac{1.4}{1.4-1}}\right)$$

$P_1 = 54798.1\,\text{Pa}$

$$T_1 = \left(T_0\right)\left(1 + \left(\left(\frac{\gamma-1}{2}\right)\left(\frac{V_{Plane}}{a}\right)^2\right)\right)$$

$$T_1 = \left(248.55\right)\left(1 + \left(\left(\frac{1.4-1}{2}\right)\left(\frac{154.21}{316.01}\right)^2\right)\right)$$

$T_1 = 260.38\,\text{K}$

$P_2 = \eta_{Duct}P_1$

$P_2 = \left(0.99\right)\left(54798.1\right)$

$P_2 = 54250.11\,\text{Pa}$

$T_2 = T_1 = 260.38\,\text{K}$

$P_4 = P_2\left(PR\right)$

$P_4 = 54250.11\left(9.13\right)$

$P_4 = 495303.5\,\text{Pa}$

$$T_4 = T_2 + \frac{T_2}{\eta_c}\left(PR^{\frac{\gamma-1}{\gamma}} - 1\right)$$

$$T_4 = 260.38 + \frac{260.388}{0.82}\left(9.13^{\frac{2}{7}} - 1\right)$$

$T_4 = 537.86\,\text{K}$

$$P_5 = P_4\left(1 - \rho_{\Delta P}\right)$$
$$P_5 = 495303.5\left(1 - 0.051\right)$$
$$P_5 = 470043.1 \text{ Pa}$$

$$\Delta T_{Cb} = 610 \text{ K} \quad \text{(Calculated)}$$
$$T_5 = T_4 + \Delta T_{Cb}$$
$$T_5 = 537.86 + 610$$
$$T_5 = 1147.86$$

$$P_6 = \left(P_0\right)\left(1.05\right) = 48890.98 \text{ Pa}$$

$$T_6 = T_5 - \eta_t T_5 \left(1 - \frac{1}{\left(\dfrac{P_5}{P_6}\right)^{\frac{1}{4}}}\right)$$

$$T_6 = 1102.63 - \left(0.85\right)\left(1102.63\right)\left(1 - \frac{1}{\left(\dfrac{470043.1}{48890.98}\right)^{\frac{1}{4}}}\right)$$

$$T_6 = 724.84 \text{ K}$$

Air bleeding for NGV cooling

Coolant air bled from compressor is ±2% for NGV cooling

$$w_a = 8.66 \, kg / \sec \quad [1]$$
$$w_{bleed} = 0.02 w_a$$
$$w_{bleed} = \left(0.02\right)\left(8.663\right)$$
$$w_{bleed} = 0.17327 \text{ kg/sec}$$

Table C1 Derived T56 engine pressure and temperature for 20 000 feet

20 000 Feet	Pressure (Pa)	Temperature (K)
0 Ambient	46562.84	248.55
1 Engine Inlet	54798.10	260.38
2 Compressor Inlet	54250.11	260.38
4 Compressor Outlet	495303.5	537.86
5 Combustor Outlet	470043.1	1147.86
6 Turbine Outlet	48890.98	724.84

The turbine inlet temperature was used to formulate the temperature profile for the calculated average turbine inlet temperature for 20 000 feet cruising.
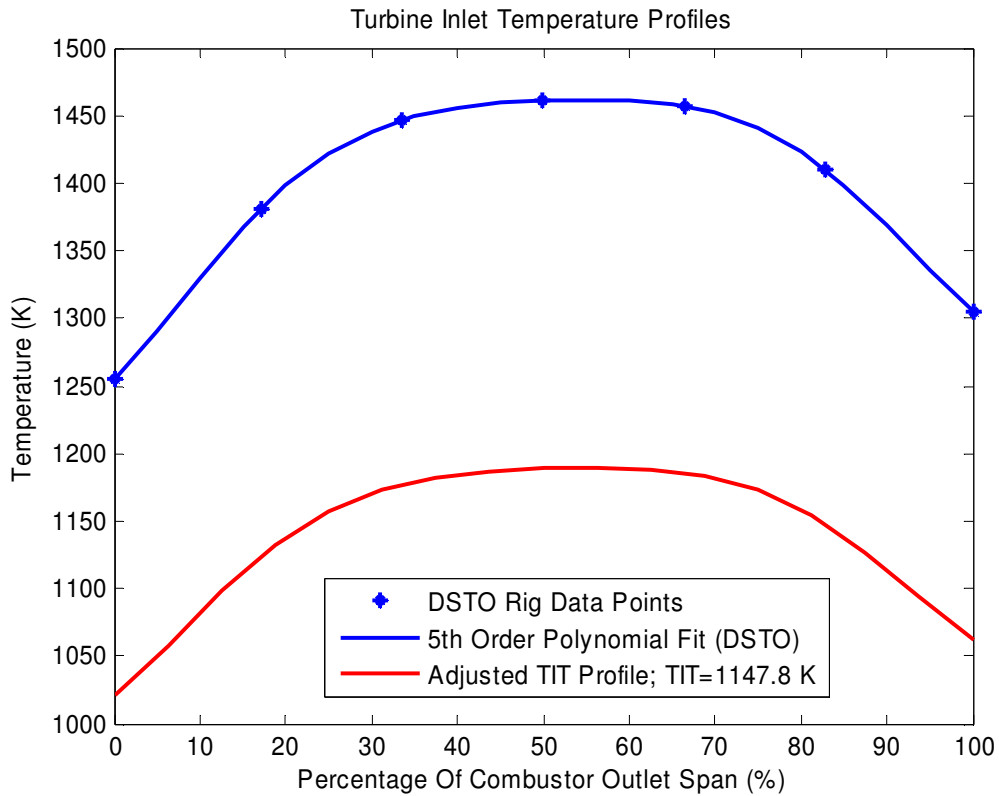
Fig. C1 Turbine inlet temperature vs. percentage of radial distance of the combustors outlet [54]

APPENDIX D

DERIVED T56 ENGINE

CONDITIONS

Derivation

$$\Delta s = C_p \ln\left(\frac{T_2}{T_1}\right) - R \ln\left(\frac{P_2}{P_1}\right)$$

$$Assume \, \Delta s = 0, \left(Isentropic\right)$$

$$0 = C_p \ln\left(\frac{T_2}{T_1}\right) - R \ln\left(\frac{P_2}{P_1}\right)$$

$$\ln\left(\frac{T_2}{T_1}\right) = \frac{R}{C_p} \ln\left(\frac{P_2}{P_1}\right)$$

$$R = C_p - C_v$$

$$\frac{R}{C_p} = \frac{\dfrac{C_p}{C_v} - \dfrac{C_v}{C_v}}{\dfrac{C_p}{C_v}} = \frac{\gamma - 1}{\gamma}$$

$$\ln\left(\frac{T_2}{T_1}\right) = \frac{\gamma - 1}{\gamma} \ln\left(\frac{P_2}{P_1}\right)$$

$$\frac{T_2}{T_1} = \left(\frac{P_2}{P_1}\right)^{\frac{\gamma - 1}{\gamma}}$$

$$\frac{T_2}{T_1} - 1 = \left(\frac{P_2}{P_1}\right)^{\frac{\gamma - 1}{\gamma}} - 1$$

Including Compressor Efficiency

$$\frac{T_2}{T_1} - 1 = \eta_c \left[\left(\frac{P_2}{P_1} \right)^{\frac{\gamma-1}{\gamma}} - 1 \right]$$

$$\frac{\dfrac{T_2}{T_1} - \dfrac{T_1}{T_1}}{\dfrac{T_1}{T_1}} - 1 = \eta_c \left[\left(\frac{P_2}{P_1} \right)^{\frac{\gamma-1}{\gamma}} - 1 \right]$$

$$T_2 - T_1 = T_1 \eta_c \left(\frac{P_2}{P_1} \right)^{\frac{\gamma-1}{\gamma}} - T_1$$

$$T_2 - T_1 = T_1 \eta_c \left[\left(\frac{P_2}{P_1} \right)^{\frac{\gamma-1}{\gamma}} - 1 \right]$$

$$T_2 = T_1 \eta_c \left[\left(\frac{P_2}{P_1} \right)^{\frac{\gamma-1}{\gamma}} - 1 \right] + T_1$$

Efficiency and Pressure drop calculation using marketing chart data

Pressure Ratio

$$\frac{P_2}{P_1} = \frac{958.5}{953.28} = 9.1362$$

Compressor Efficiency

$$\eta_c = \frac{T_2}{T_3 - T_2} \left[\left(\frac{P_2}{P_1} \right)^{\frac{\gamma-1}{\gamma}} - 1 \right]$$

$$\eta_c = \frac{291.79}{602.87 - 291.79} \left[\left(\frac{958.5}{104.91} \right)^{\frac{1.4-1}{1.4}} - 1 \right]$$

$$\eta_c = 0.8268$$

$$\eta_c = 82.68\%$$

Turbine Efficiency

$$\eta_t = \frac{T_5 - T_6}{T_5 \left[1 - \left(\dfrac{1}{\dfrac{P_4}{P_5}} \right)^{\frac{\gamma - 1}{\gamma}} \right]}$$

$$\eta_t = \frac{1350 - 858.94}{1350 \left[1 - \left(\dfrac{1}{\dfrac{932.52}{120.33}} \right)^{\frac{1.333 - 1}{1.333}} \right]}$$

$$\eta_t = 0.8528$$

$$\eta_t = 85.28\%$$

Diffuser Pressure Drop

$$\eta_{diff} = \frac{P_3 - P_4}{P_3} = \frac{958.5069\text{-}953.2826}{958.5069} = 0.00545$$

Combustor Pressure Drop

$$\rho_{\Delta P} = \frac{P_4 - P_5}{P_4} = \frac{953.2826\text{-}932.5161}{953.2826} = 0.0217$$

Diffuser Temperature Gain

$$\tau_{\Delta T} = \frac{T_4 - T_3}{T_4} = \frac{602.8724\text{-}604.6175}{602.8724} = 0.00288$$

Combustor Efficiency

$$\delta_{Cb} = \frac{p_{t2}}{p_0}$$

$$\delta_{Cb} = \frac{(P_{am})(RPR)}{101.325}$$

$$\delta_{Cb} = \frac{(P_{am})\left((RTR)(\eta_{Duct})\left(\dfrac{P_{am}}{p_{n7}}\right)\right)}{101.325}$$

$$\delta_{Cb} = \frac{(P_{am})\left(\left(1+\left(\left(\dfrac{\gamma-1}{2}\right)(M)^2\right)^{\frac{\gamma}{\gamma-1}}\right)(\eta_{Duct})\left(\dfrac{P_{am}}{p_{n7}}\right)\right)}{101.325}$$

but $P_{am} = p_{n7}$

$$\delta_{a} = \frac{(P_{am})\left(\left(1+\left(\left(\dfrac{\gamma-1}{2}\right)\left(\dfrac{V_{Plane}}{V_{Sound}}\right)^2\right)^{\frac{\gamma}{\gamma-1}}\right)(\eta_{Duct})\right)}{101.325}$$

$$\delta_{Cb} = \frac{(101.325)\left(\left(1+\left(\left(\dfrac{1.333-1}{2}\right)\left(\dfrac{167.19}{340.3}\right)^2\right)^{\frac{1.333}{1.333-1}}\right)(0.99)\right)}{101.325}$$

$$\delta_{Cb} = 0.99$$

Fig. $3A-10$ *Air Flow* [29]

$$\frac{w_a}{\delta_{Cb}} = 15.92\,kg/\sec$$

$$w_a = 15.92\delta_{Cb} = (15.92)(0.99)$$

$$w_a = 15.76\,kg/\sec$$

Fig.$3A-13$ *Fuel Flow* [29]

$$\frac{w_f}{\delta_{Cb}} = 0.33238\,kg\,/\sec$$

$$w_f = 0.33238\delta_{Cb} = (0.33238)(0.99)$$

$$w_f = 0.3290\,kg\,/\sec$$

T_5 *Is the TIT of Operating Manual*

$$\Delta T_{Cb} = T_5 - T_4 = 1350 - 604.61 = 745.38\,K$$

$$\frac{w_f}{w_a}_{Operating\,Manual} = \frac{0.3290}{15.7608} = 0.020878$$

$$\frac{w_f}{w_a}_{Marketing\,Chart-Fig.2.17[4]} = 0.021$$

$$\eta_{Cb} = \frac{\dfrac{w_f}{w_a}_{Operating\,Manual}}{\dfrac{w_f}{w_a}_{Marketing\,Chart-Fig.2.17[4]}} = \frac{0.020878}{0.021}$$

$$\eta_{Cb} = 0.994$$

Air Bleeding for NGV Cooling

Coolant Air Bled From Compressor is ±2% for NGV Cooling

$$w_{bleed} = 0.02 w_a$$

$$w_{bleed} = (0.02)(15.76084073)$$

$$w_{bleed} = 0.315216815\,kg/\sec$$

Take-off Conditions

$$P_1 = \left(P_0\right)\left(1 + \left(\left(\frac{\gamma-1}{2}\right)\left(\frac{V_{Plane}}{a}\right)^2\right)^{\frac{\gamma}{\gamma-1}}\right)$$

$P_0 = 101325 \, Pa$

$\gamma = 1.4$ for unburnt air at sea level [4]

$a = \sqrt{\gamma R T}$

$a = \sqrt{(1.4)(287)(288)}$

$a = 340.17 \, m/s$

$V_{Plane} = 78.24 \, m/s$ $(Assumed)$

$$P_1 = 101325\left(1 + \left(\left(\frac{1.4-1}{2}\right)\left(\frac{78.24}{340.17}\right)^2\right)^{\frac{1.4}{1.4-1}}\right)$$

$P_1 = 105126.94 \, Pa$

$$T_1 = \left(T_0\right)\left(1 + \left(\left(\frac{\gamma-1}{2}\right)\left(\frac{V_{Plane}}{a}\right)^2\right)\right)$$

$$T_1 = \left(288\right)\left(1 + \left(\left(\frac{1.4-1}{2}\right)\left(\frac{78.24}{340.17}\right)^2\right)\right)$$

$T_1 = 291.04 \, K$

$P_2 = \eta_{Duct} P_1$

$\eta_{Duct} = 0.99 [1]$

$P_2 = \left(0.99\right)\left(105126.9486\right)$

$P_2 = 104075.6792 \, Pa$

Although derived, no temperature gain is assumed across inlet duct

$T_2 = T_1 = 291.04 \, K$

$$T_4 = T_2 + \frac{T_2}{\eta_c}\left(PR^{\frac{\gamma-1}{\gamma}} - 1\right)$$

$$T_4 = 291.04 + \frac{291.04}{0.82}\left(9.13^{\frac{1.4-1}{1.4}} - 1\right)$$

$$T_4 = 601.19\,\text{K}$$

$$P_4 = (PR)(P_2)$$
$$P_4 = (9.13)(104075.7)$$
$$P_4 = 950211\,\text{Pa}$$

$$P_5 = P_4(1 - \rho_{\Delta P})$$
$$P_5 = 950211(1 - 0.051)$$
$$P_5 = 901750.2\,\text{Pa}$$

$$T_5 = 1350K \quad [29]$$

A 5% pressure gain is assumed over the exit duct

$$P_6 = (P_0)(1 + 0.05)$$
$$P_6 = (P_0)(1.05) = 106391.3\,\text{Pa}$$

$$T_6 = T_5 - \eta_t T_5\left(1 - \frac{1}{\left(\frac{P_5}{P_6}\right)^{\frac{1}{4}}}\right)$$

$$T_6 = 1350 - (0.85)(1350)\left(1 - \frac{1}{\left(\frac{901750.2}{106391.3}\right)^{\frac{1}{4}}}\right)$$

$$T_6 = 873.41\,\text{K}$$

APPENDIX E

FLUENT / TACT1 RESULTS

Metal temperature of sectional slices through blade
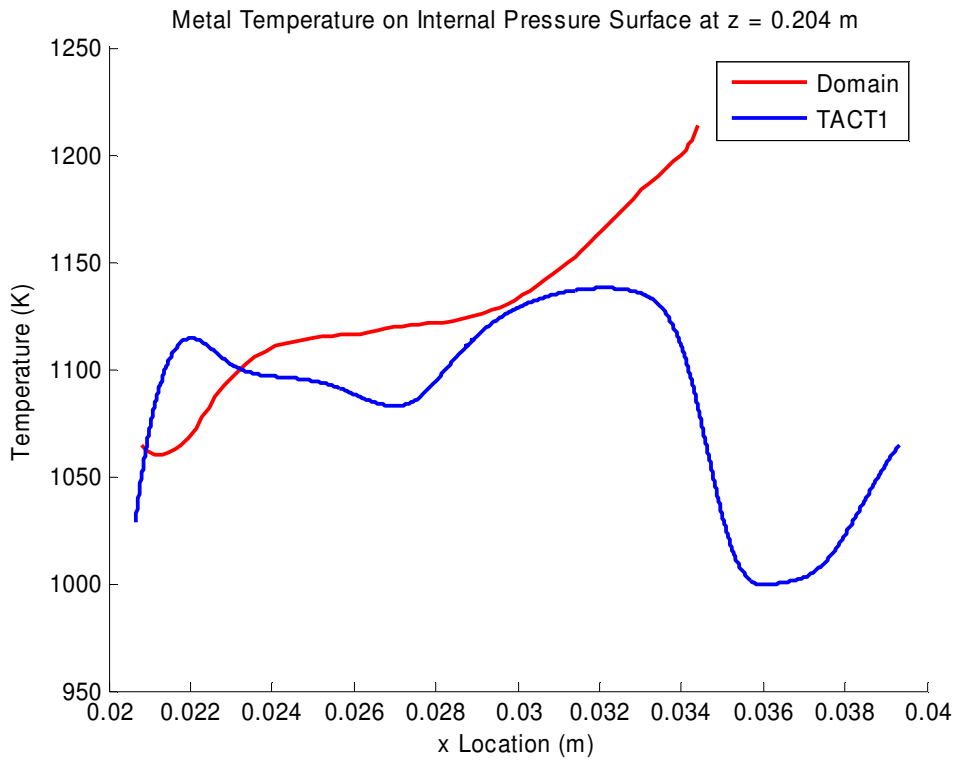
Fig. E1 Metal temperature on internal pressure surface at radial distance of 0.204 m
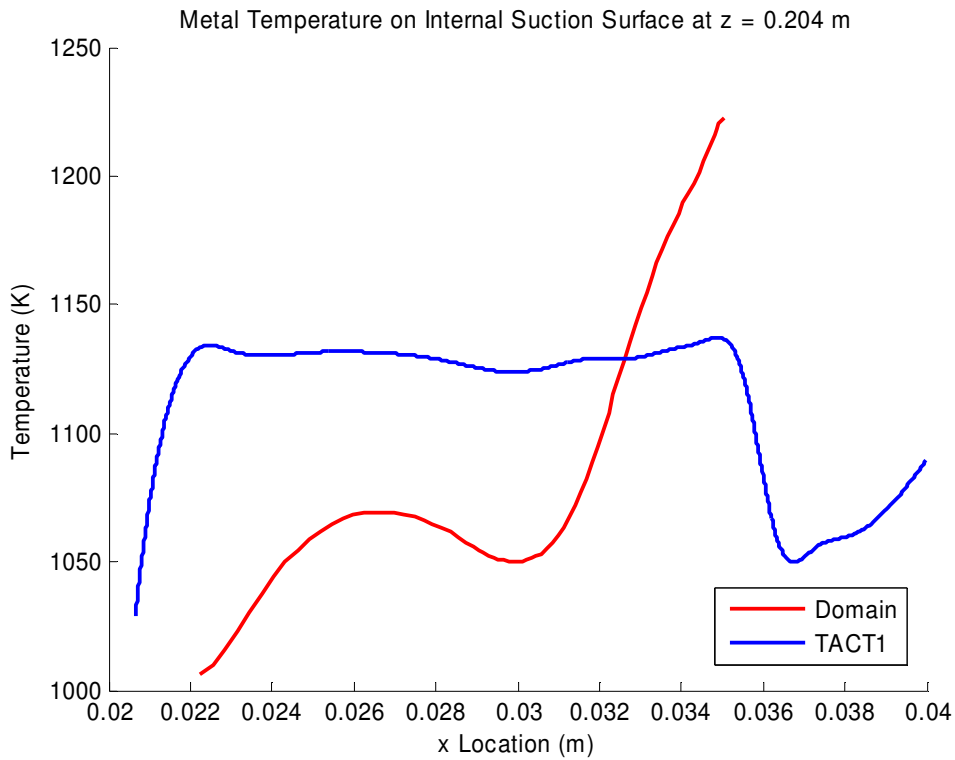
Fig. E2 Metal temperature on internal suction surface at radial distance of 0.204 m
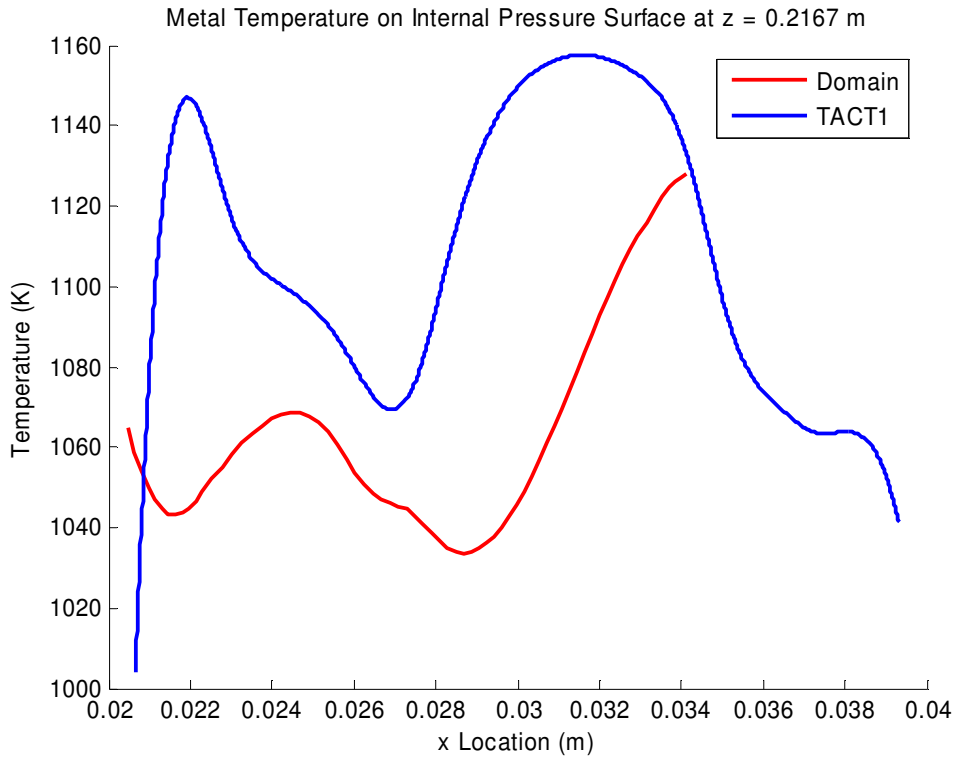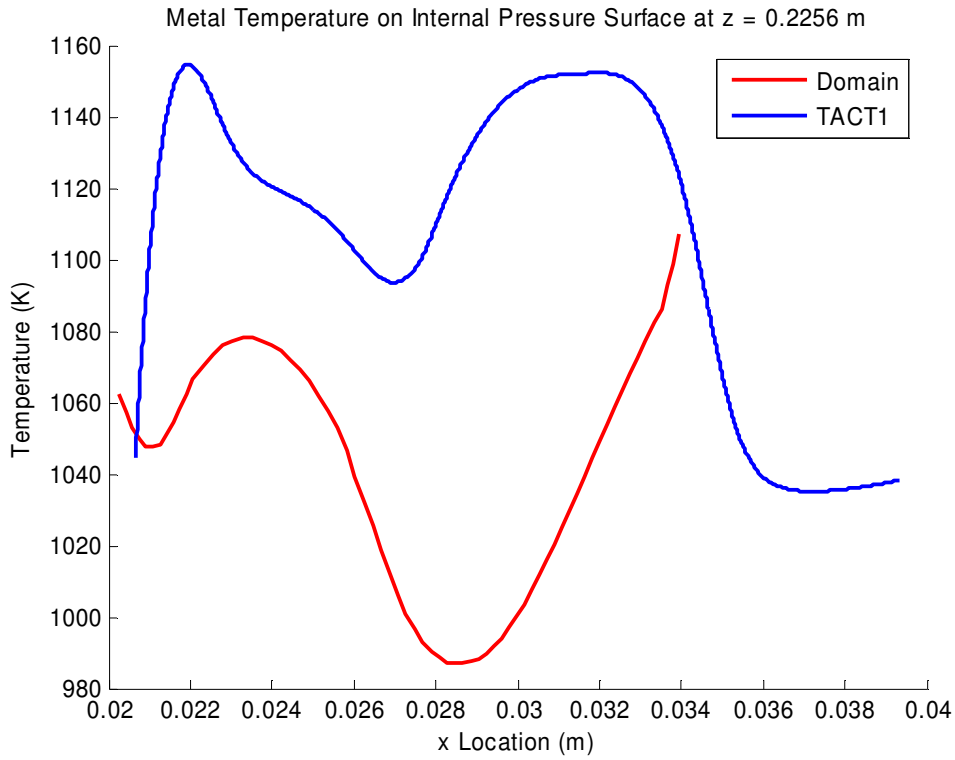
Fig. E3 Metal temperature on internal pressure surface at radial distance of 0.216 m
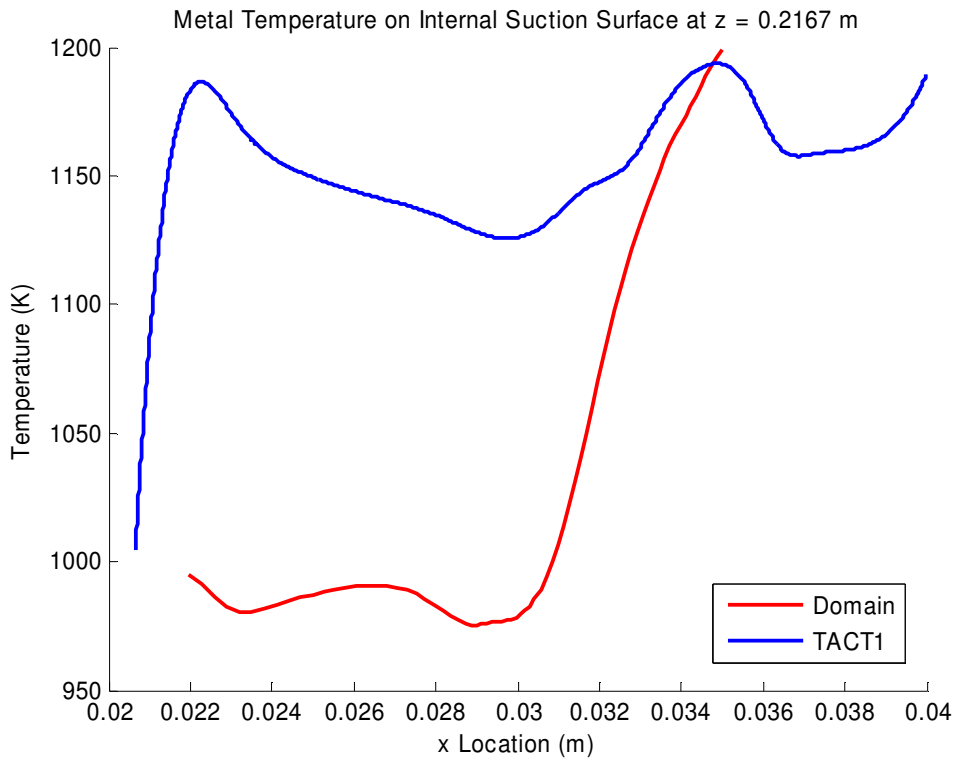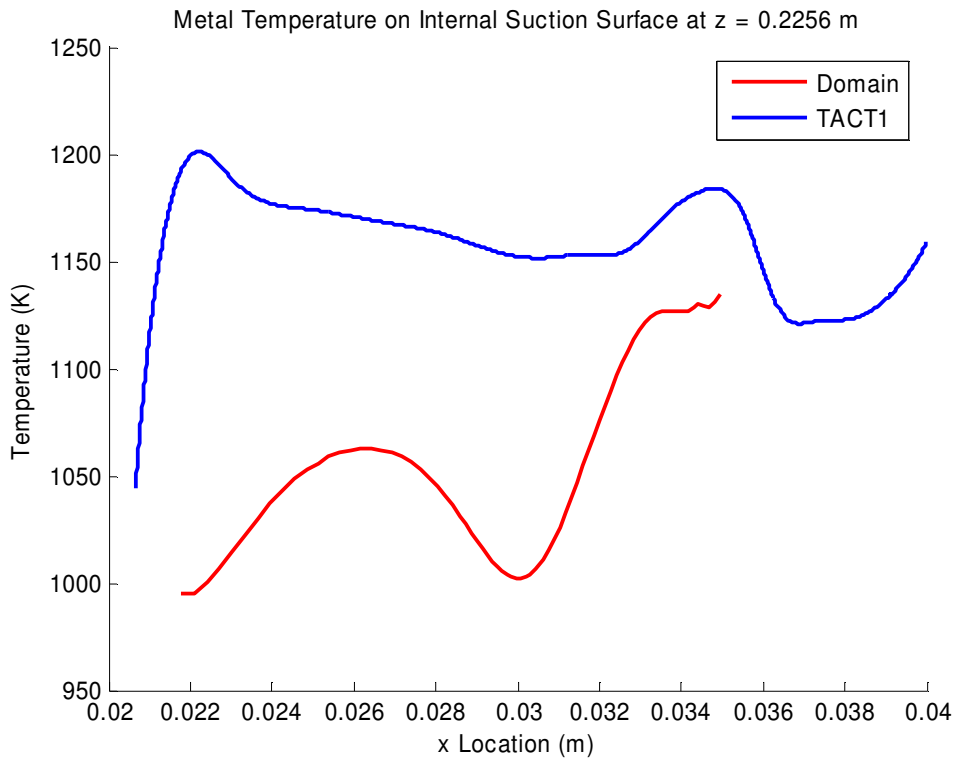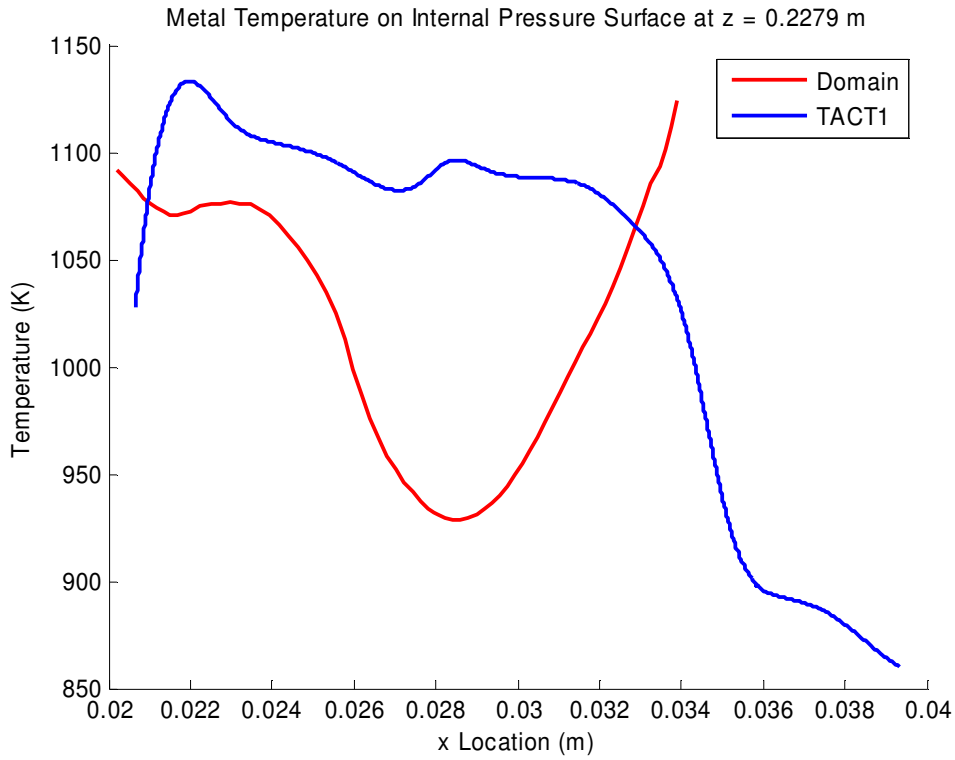

Fig. E4 Metal temperature on internal suction surface at radial distance of 0.2167 m
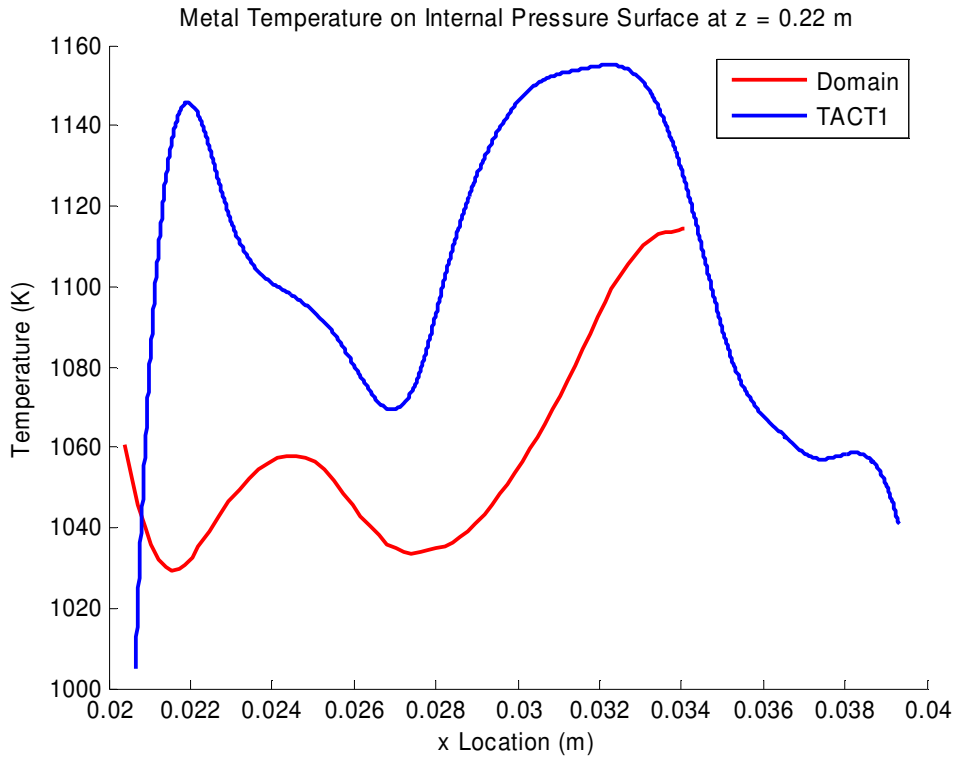
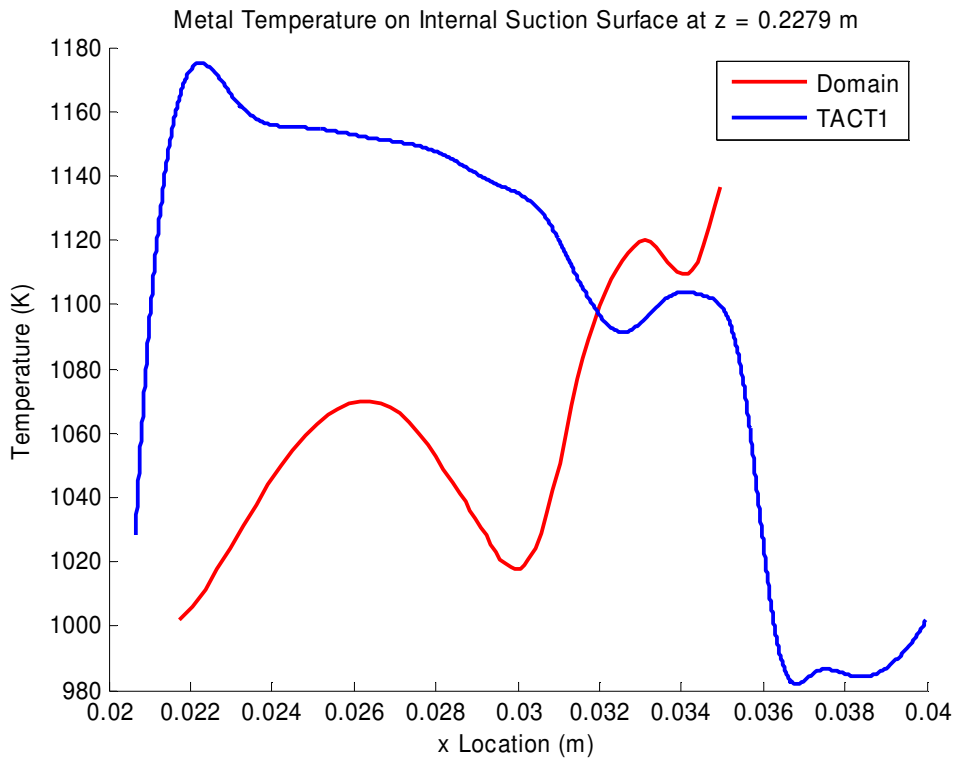*Fig. E5 Metal temperature on internal pressure surface at radial distance of 0.22 m*
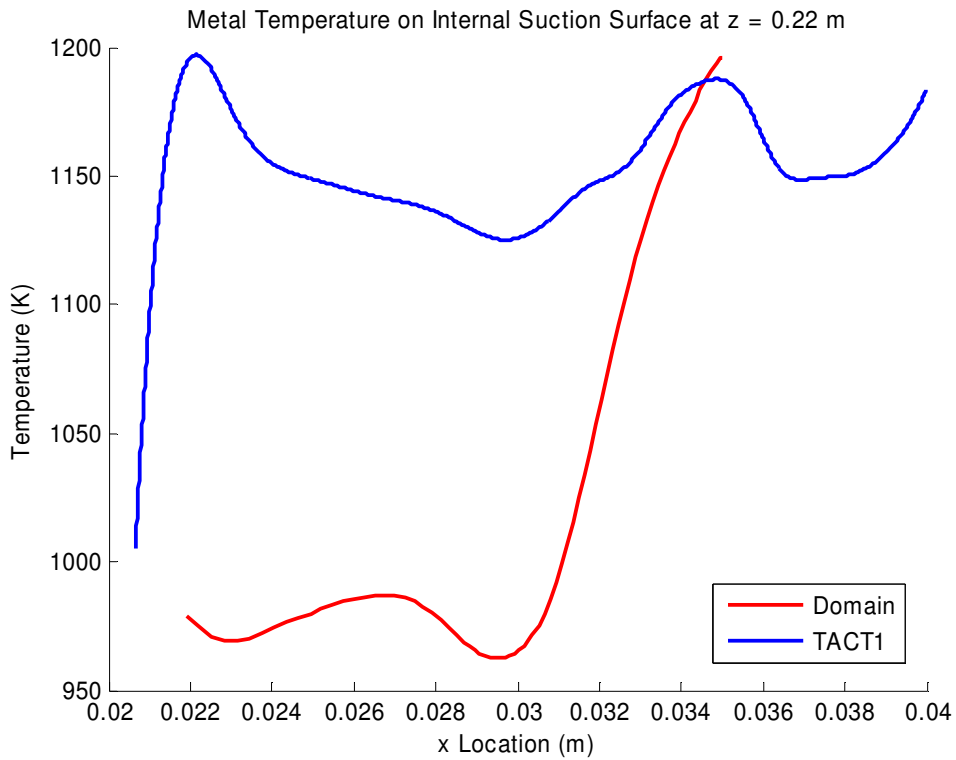
*Fig. E6 Metal temperature on internal suction surface at radial distance of 0.22 m*

Fig. E7 Metal temperature on internal pressure surface at radial distance of 0.2256 m

Fig. E8 Metal temperature on internal suction surface at radial distance of 0.2256 m

Fig. E9 Metal temperature on internal pressure surface at radial distance of 0.2279 m

Fig. E10 Metal temperature on internal suction surface at radial distance of 0.2279 m
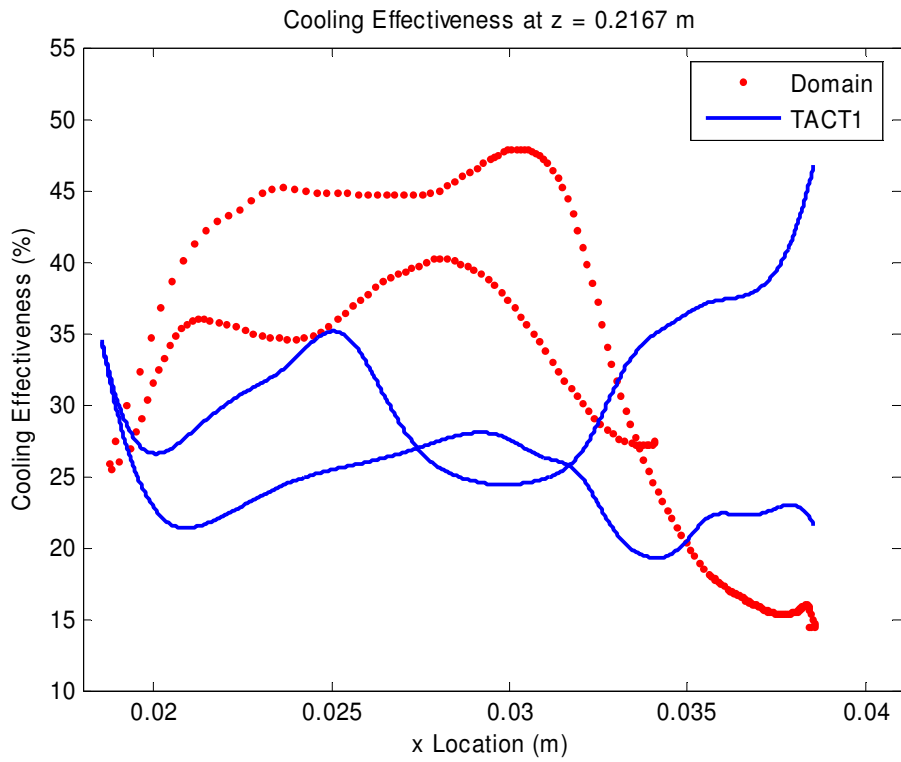
Cooling Effectiveness at z = 0.204 m

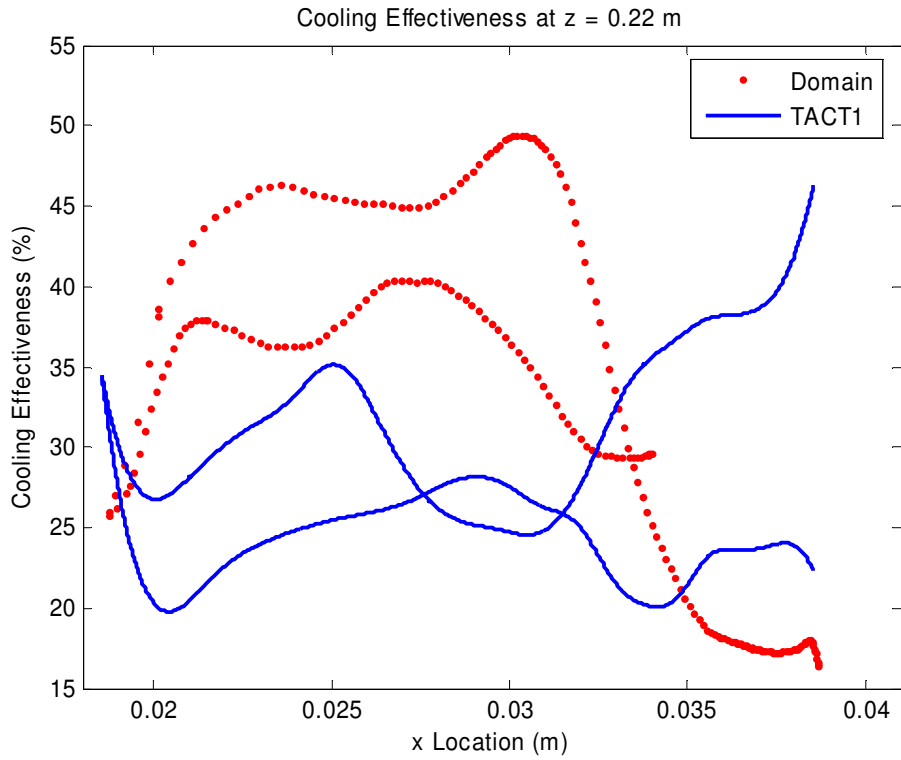*Fig. E11 Cooling effectiveness at radial distance of 0.204 m*
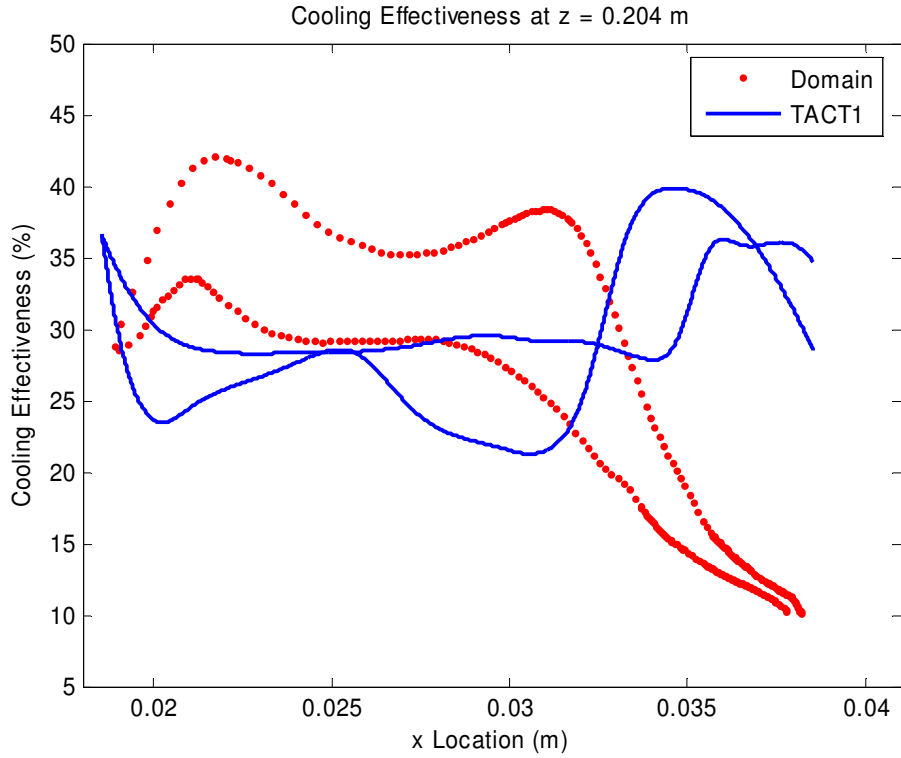
Cooling Effectiveness at z = 0.2167 m

Fig. E12 Cooling effectiveness at radial distance of 0.2167 m

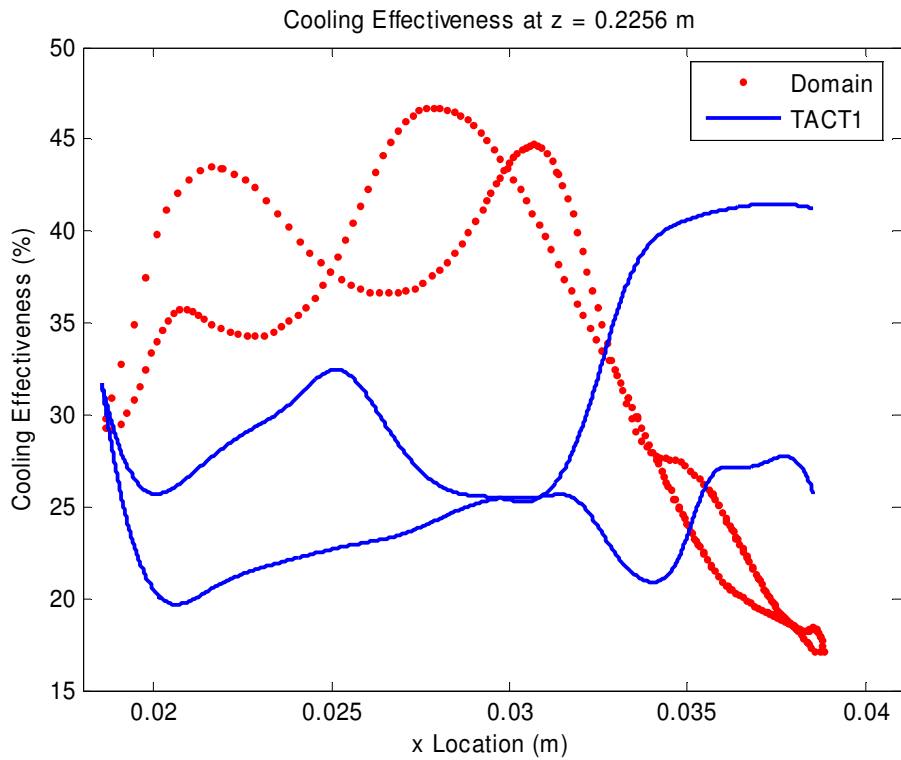*Fig. E13 Cooling effectiveness at radial distance of 0.22 m*

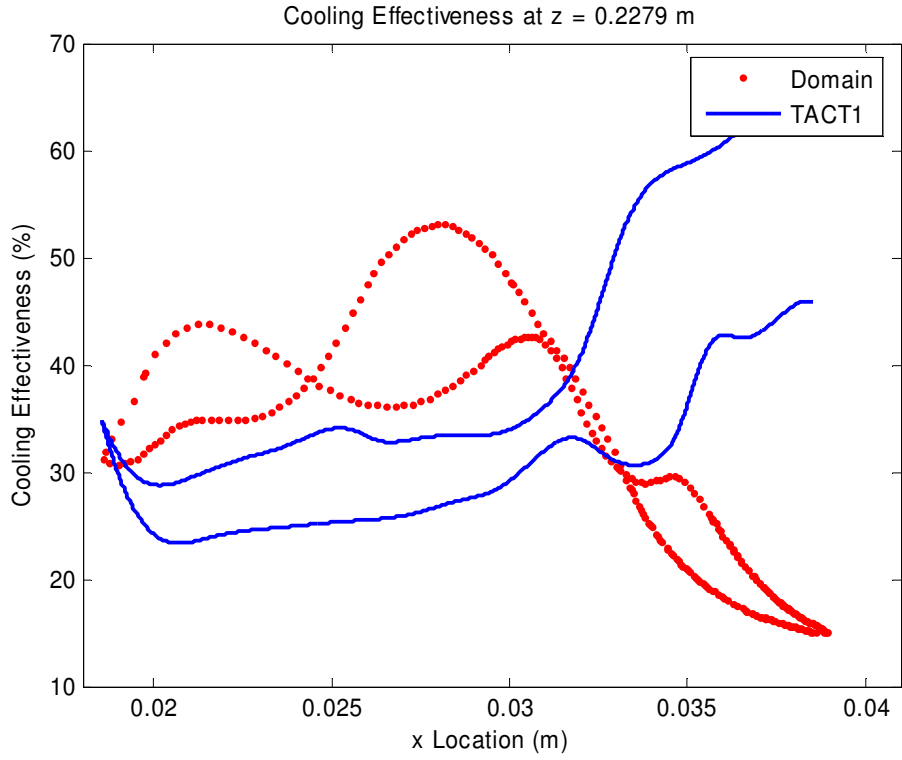*Fig. E14 Cooling effectiveness at radial distance of 0.2256 m*

Fig. E15 Cooling effectiveness at radial distance of 0.2279 m